

**A Geophysical Package for
In-situ Planetary Science**

Thesis submitted for the degree of
Doctor of Philosophy
at the University of Leicester

by

Michelle Sarah Skidmore

Space Projects and Instrumentation Group
Department of Physics and Astronomy
University of Leicester

September 2009

Declaration

I hereby declare that no part of this thesis has been previously submitted to this or any other university as part of the requirement for a higher degree. The work described herein was conducted solely by the undersigned except for those colleagues and other workers acknowledged in the text.

Michelle Sarah Skidmore

15/09/2009

A Geophysical Package for In-situ Planetary Science

Michelle Sarah Skidmore

Abstract

Measuring the effect of geological and chemical processes, weather, biological processes and the interaction of SCR and GCR radiation with a planet is fundamental to understanding the formation, evolution and alteration of a planet. This thesis details the evolution and development of a geophysical package that can be used to better understand the effect of these fundamental physical processes by measuring composition, constraining heat flow and measuring the age of a planetary surface. There are a number of future ESA and NASA planetary science missions that are in the planning or initial study phases, where the scientific objectives include determining the surface composition, measuring planetary surface heat flow and constraining planetary chronology.

The geophysical package is capable of operation on landers and penetrators; both of these are possible in-situ platforms being proposed for these missions. In addition radioisotope power sources are being proposed for both thermal management and electricity generation; the power source might provide the source of neutrons to induce the γ -ray emission from the planetary surface. The development and verification of a Monte Carlo planetary radiation environment model using both experimental data and data acquired in orbit of the Moon and Mars is described in this thesis. It was used to model the geophysical package on the surface and sub-surface of Mars and Europa. The model was also used to investigate the suitability of several neutron sources to induce γ -ray emission on a planetary surface that could also be used for power generation.

Acknowledgements

I would like to thank my supervisor, Richard Ambrosi, Emma Bunce and Dave Vernon for all their help and advice over the past three years. I would also like to thank the Engineering and Physical Sciences Research Council for funding this work.

To Danny and Charly, I wouldn't have got through three years without you dragging me out to coffee, nights out and bringing me cakes- I only hope my new office mates are the same! Thanks to my housemates Lucy, Dee and Hannah for helping me survive my third year through the cinema evenings, pub quiz Tuesdays, red wine Wednesdays and for Sundays watching whole series of the West Wing etc. to keep me sane! Thanks also to the PhD students in the Physics building for the pub trips and a cup of tea and biscuits at 3.45 pm everyday!

To my family, thank you for listening and giving me all those pep-talks, even when they involved telling me to pull myself together!

Finally to Keith, thank you for all the dinners you cooked while I was working at my laptop, for putting up with me being grouchy because I had to work at weekends and for proof-reading work for me when I asked; in short, thanks for being handsome!

Publications

Some of the results presented in this thesis have been incorporated into the following papers. The chapters to which these papers refer are given in brackets.

- I. Ambrosi, R. M., Ball, A. J., Nelms, N., Talboys, D., Bentley, M. S., Spohn, T., Nadalini, R., Hagermann, A., Richter, L., Calcutt, S., Fraser, G. W., Bridges, J., Zarnecki, J. S., Cockell, C. S., Grady, M. M., Simon, H., Siffert, P., Skidmore, M. S., (2006), X-ray and γ -ray Spectrometers for the Heat Flow and Physical Properties Instrument (HP3) on the ExoMars Geophysical and Environmental Package. Presented at the 4th International Planetary Probe Workshop, Pasadena, 27-30th June 2006, Submitted to: Conference Proceedings, 4th International Planetary Probe Workshop 27-30th June 2006, (Chapters 2, 3, 4).
- II. Skidmore, M. S., Ambrosi, R. M., Simon, H., (2009), A Hybrid X-ray and γ -ray Detector for In-situ Planetary Science Missions, Nuclear Instruments and Methods in Physics Research A, 604(3), pp. 592-603 (Chapter 4).
- III. Skidmore, M. S., Ambrosi, R. M., Vernon, D., Calzada, E., Benedix, G., Bücherl, T., Schillinger, B., (2009), Prompt γ -ray Activation Analysis of Martian Analogues at the FRM-II Neutron Reactor and the Verification of a Monte Carlo Planetary Radiation Environment Model, Nuclear Instruments and Methods in Physics Research A, 607, pp. 421-431 (Chapter 5).
- IV. Skidmore, M. S., Ambrosi, R. M., Verification of Monte Carlo Planetary Surface Radiation Environment Model using γ -ray Data from Lunar Prospector and 2001 Mars

Odyssey, (2009), Nuclear Instruments and Methods in Physics Research A, 612, pp. 296-302 (Chapter 6).

- V. Skidmore, M. S., Ambrosi, R. M., (2009), γ -ray Spectroscopy in Mars Orbit During Solar Proton Events, Advances in Space Research, 44, pp. 1019- 1029 (Chapter 7).
- VI. Skidmore, M. S., Ambrosi, R. M., O'Brien, R. C., (2009), Neutron Sources for In-situ Planetary Science Applications, Nuclear Instruments and Methods in Physics Research Section A, 608, pp. 403- 409 (Chapter 8).

Table of Contents

Chapter 1 Introduction.....	1
1.1 Objectives of Future In-situ XRF and GRS Missions	2
1.2 Background and Objectives of this Thesis.....	4
Chapter 2 Background to X-ray Spectroscopy, γ -ray Spectroscopy, γ -ray Densitometry and Radiometric Dating	9
2.1 Introduction.....	9
2.2 Origin of Particles and Radiation that Interact with a Planetary Body	9
2.3 Generation of X-rays	11
2.4 Generation of γ -rays	12
2.5 X-ray and γ -ray Spectroscopy.....	16
2.6 Orbital versus In-situ γ -ray Spectroscopy.....	21
2.7 γ -ray Backscatter Densitometry	23
2.8 K- Ar Radiometric Dating	30
2.9 Summary	33
Chapter 3 X-ray and γ -ray Detectors.....	34
3.1 Introduction.....	34
3.2 The Detector System	35
3.3 Photon Interactions with the Detector	37
3.4 Semiconductor Detectors.....	40
3.5 Scintillator Detectors	50
3.6 Intrinsic Full-Energy Photopeak Efficiency and Resolution	53
3.7 Types of Semiconductor Detectors	56

3.8 Examples of γ -ray Spectrometers on Previous Spacecraft	63
3.9 Summary	64
Chapter 4 Characterisation and Selection of γ -ray Detectors for a Geophysical Package...	65
4.1 Introduction.....	65
4.2 γ -ray Detectors for the Geophysical Package	65
4.3 Experimental Methodology.....	68
4.4 Results.....	71
4.5 Discussion	78
4.6 Conclusion	89
Chapter 5 Development and Verification of a Monte Carlo Model using Experimental Data	
.....	90
5.1 Introduction.....	90
5.2 Prompt γ -ray Activation Analysis	90
5.3 Planetary Radiation Environment Modelling with MCNPX.....	91
5.4 PGAA at FRM-II.....	93
5.5 Modelling the γ -ray Emission from PGAA using MCNPX	107
5.6 Discussion	112
5.7 Conclusion	115
Chapter 6 Development and Verification of a Monte Carlo Planetary Radiation	
Environment Model using γ -ray Data from Lunar Prospector and 2001 Mars Odyssey...	117
6.1 Introduction.....	117
6.2 Verification Methodology.....	118
6.3 Verifying the Model using 2001 Mars Odyssey γ -ray Data	120
6.4 The Martian Monte Carlo Model	126

6.5 Verifying the Model using Lunar Prospector γ -ray Data	134
6.6 Results.....	136
6.7 Discussion	138
6.8 Conclusion	141
Chapter 7 γ -ray Spectroscopy in Mars Orbit During Solar Proton Events.....	142
7.1 Introduction.....	142
7.2 SPEs.....	142
7.3 Detection of SPEs at the Earth and Mars.....	146
7.4 SPE Data	150
7.5 γ -ray Data Analysis	154
7.6 Results.....	155
7.7 Discussion	158
7.8 Conclusion	159
Chapter 8 Neutron Sources for In-situ Planetary Science Missions	161
8.1 Introduction.....	161
8.2 The Geophysical Instrument: Neutron Sources	162
8.3 Neutron Sources for In-situ Applications	164
8.4 The Physical Model.....	166
8.5 Results.....	173
8.6 Discussion	180
8.7 Conclusion	185
Chapter 9 Summary.....	186
Appendix A.....	192
References	199

Table of Figures

Figure 1-1. A schematic of the proposed design of the HP ³ mole, featuring a suite of geophysical instruments. Taken from Ambrosi et al. (2006).....	5
Figure 2-1. A diagram of the processes involved in a spallation reaction. Adapted from URL: www.sckcen.be/myrrha/images/spallation.png	12
Figure 2-2. Diagram showing possible interactions of protons and solar X-rays with a planetary surface to produce γ -rays and X-rays.....	13
Figure 2-3. Two of the possible neutron interactions with an atom, a) inelastic scattering, b) neutron capture. Adapted from Brookshaw (2006).....	14
Figure 2-4. The fractional proton penetration through the Martian atmosphere obtained via the Monte Carlo model described in Chapter 6. Protons of < 100 MeV do not survive to the Martian surface.....	15
Figure 2-5. Fractional proton penetration into the Martian surface obtained via the Monte Carlo model described in Chapter 6. Protons under 100 MeV do not survive to the surface. The higher the proton energy, the greater the penetration into the Martian surface.....	16
Figure 2-6. How the γ -ray count rate in a given energy window for two detectors at different fixed positions relative to the source varies with density. Detector I has a sonde length that is smaller than detector II. Taken from Ambrosi et al. (2007).	27
Figure 2-7. Schematic of the original HP ³ densitometer. Taken from Ambrosi et al. (2006).	28
Figure 2-8. Diagram showing the Compton window in a ¹³⁷ Cs spectrum. Taken from Ball et al. (2007).....	29
Figure 3-1. Block diagram of the elements that comprise a spectrometer. The analog to digital converter (ADC) is usually incorporated into the MCA.....	35
Figure 3-2. A block diagram to show the stages in the signal processing of the photon interaction with the detector. Taken from Ball et al. (2007).....	36
Figure 3-3. The absorption cross-section variation with energy for Si and Ge for photoelectric absorption, Compton scattering and pair production. Data taken from: Hubbell and Seltzer (2004).	38
Figure 3-4. A ¹³⁷ Cs spectrum to show the main photopeak and the Compton scattering region.....	39
Figure 3-5.a) A representation of incident radiation imparting enough energy to an electron involved in bonding in the crystal lattice to cause the electron to break the bond, leaving a positive charge or 'hole'. b) shows the band model representation; the electron is shown leaving the valence band and entering the conduction band.....	42
Figure 3-6. a) An n-type semiconductor with an excess of donor sites, b) A p-n junction before the application of an applied voltage, c) after the application of an applied bias voltage, showing the depleted region of the semiconductor.....	44
Figure 3-7. The majority carrier collection contribution to the charge collection as a function of where the ionising event occurred. Taken from Hage-Ali and Siffert (1995).....	47
Figure 3-8. Methods of recombination in a semiconductor detector.....	48

Figure 3-9. Electron mobility in CdTe with temperature from 190 K to 300 K. Data taken from Sellin et al. (2004).....	50
Figure 3-10. A diagram of the interactions that occur in a scintillator detector.....	51
Figure 3-11. A diagram of the processes that occur in the PMT.....	52
Figure 3-12. A diagram of the co-axial detector, the thick outer contact is lithium diffused and forms a p-n junction. Taken from Gehrels et al. (1988).....	57
Figure 3-13. The hemispherical detector configuration.....	61
Figure 4-1. Experimental set up of the detectors; the standards were placed at the bottom of the lead cave.....	68
Figure 4-2. The vacuum chamber containing the hemispherical CdTe detector.....	70
Figure 4-3. ^{137}Cs spectrum for the five evaluated detectors showing the 0.662 MeV peak.....	73
Figure 4-4. Resolution with varying energy for the evaluated scintillator detectors.....	74
Figure 4-5. Resolution with varying energy for the evaluated semiconductor detectors.....	74
Figure 4-6. Photopeak efficiencies with energy for the five detectors.....	77
Figure 4-7. The background of the $\text{LaBr}_3(\text{Ce})$ detector.....	87
Figure 4-8. The high-energy performance of the HPGe and $\text{LaBr}_3(\text{Ce})$ detectors.....	88
Figure 5-1. A diagram of the experimental set up in the ANTARES chamber.....	98
Figure 5-2. A portion of the spectrum from the sand calibration sample. The Si, Al and H peaks have been labelled. A single escape peak is labelled as SE and a double escape peak is labelled as DE.....	101
Figure 5-3. A portion of the spectrum from the ME analogue with the strongest γ -ray peaks labelled. A single escape peak is labelled as SE and a double escape peak is labelled as DE.....	101
Figure 5-4. The unfiltered and filtered neutron spectrum that was provided by the ANTARES team and input into MCNPX. The spectrum was divided into 125 energy bins and the input was used in the MCNPX program.....	109
Figure 5-5. The ratio of the experimental to the modelled count rates for each γ -ray peak present in the calibration samples and analogues that had less than a 20 % uncertainty in the energy range 0 – 1.45 MeV and is highlighted in Table 5-2.....	111
Figure 5-6. The ratio of the experimental to the modelled count rates for each γ -ray peak present in the calibration samples and analogues that had less than a 20 % uncertainty in the energy range 1.45 – 3.6 MeV and is highlighted in Table 5-2.....	111
Figure 6-1. A map of the Martian surface, the grids are marked on the map (Boynton et al., 2007).....	121
Figure 6-2. A description of the asymmetric Gaussian function.....	123
Figure 6-3. Example of the peak fitting procedure carried out in Origin for Silicon at 1.779 MeV.....	124
Figure 6-4. The geometry of the Monte Carlo model. The detector was modelled at an altitude of 400 km above the surface.....	127
Figure 6-5. The density profile of the modelled Martian atmosphere used in the Monte Carlo model based on an average scale height of 10.8 km.....	128
Figure 6-6. The atmosphere temperature profile of the modelled Martian atmosphere. Data taken from Bergman et al, 2003.....	128
Figure 6-7. The GCR input spectrum into the 2001 Mars Odyssey simulation (Simonsen and Nealy, 1991). The spectrum was divided into 835 energy bins and formed the input into the planetary MCNPX model.....	131

Figure 6-8. The intrinsic efficiency of the HPGe detector on 2001 Mars Odyssey. Data taken from Kerry et al. (2002).....	133
Figure 6-9. The experimental to modelled count rate ratio for the elemental lines given in Table 1 for grids 1 – 3 on the Martian surface. The ratios are generally accurate to within a factor of 20 % when taking into account the associated error.....	137
Figure 7-1. Relative amounts (%) of secondary particles in the MCNPX simulated Martian surface.....	146
Figure 7-2. γ -ray spectra from the 2001 Mars Odyssey γ -ray spectrometer collected over a SPE that occurred in January 2005. Data taken from the NASA PDS Geosciences node (Boynton, 2002).....	149
Figure 7-3. EPS (15 MeV to 80 MeV) and HEPAD (320 MeV to > 700 MeV) data from GOES-11 for 2005 (Corrected proton channel data from GOES-11). Data taken from NGDC (2008).....	152
Figure 7-4. The EPS and HEPAD measured proton fluence from GOES-11 in orbit of the Earth, the HEND particle flux and the γ -ray spectrometer continuum count rate at 1.070 MeV and 7.196 MeV from 2001 Mars Odyssey in the orbit of Mars in January 2005. It shows increases in proton flux across the energy range 15 MeV to 700 MeV during the SPE. Data taken from NDGC (2008); Boynton (2002); Boynton (2004).	153
Figure 7-5. The EPS and HEPAD measured proton fluence from GOES-11 in orbit of the Earth, the HEND particle flux and the γ -ray spectrometer continuum count rate at 1.070 MeV and 7.196 MeV from 2001 Mars Odyssey in the orbit of Mars in September 2005. It shows increases in proton flux across the energy range 15 MeV to 700 MeV during the SPE. Data taken from NDGC (2008); Boynton (2002); Boynton (2004).....	154
Figure 8-1. Neutron spectra from ^{252}Cf , Am-Be, Pu-Be and enriched AmO ₂ sources. Data taken from O'Brien et al. (2009).....	166
Figure 8-2. The geometry of the geophysical package in the MCNPX model.....	167
Figure 8-3. The geometry of the geophysical package used in the model.....	167
Figure 8-4. The peak precision for the major γ -ray peak of each element on the Martian surface, using the different neutron sources when the detectors are 50 cm away from the neutron source.	174
Figure 8-5. The peak precision for the major γ -ray peak of each element on the Martian surface, using the different neutron sources when the detectors are 50 cm away from the neutron source.	175
Figure 8-6. The peak precision for the major γ -ray peak of each element on the Martian surface, using the different neutron sources when the detectors are at 2 m depth with the neutron source on the surface.....	176
Figure 8-7. The peak precision for the major γ -ray peak of each element on the Martian surface, using the different neutron sources when the detectors are at 2 m depth with the neutron source on the surface.....	177

Acronyms

ADC	Analogue to Digital Converter
ASIC	Application Specific Integrated Circuit
ASPERA	Analysers of Space Plasmas and Energetic Atoms
BGO	Bismuth Germanate
CdTe	Cadmium Telluride
CME	Coronal Mass Ejection
CPP	Compact Pulse Processor
CRB	Colombia River Basalt
CsI(Tl)	Caesium Iodide
DE	Double Escape Peak
D-T	Deuterium-tritium
ENDF	Evaluated Nuclear Data File
EPS	Energetic Particle Sensor
E_g	Forbidden Energy Gap
EPSRC	Engineering and Physical Sciences Research Council
ESA	European Space Agency
FRM-2	Forschungs-Neutronenquelle Heinz Maier-Leibnitz
FWHM	Full-width Half Maximum
GCR	Galactic Cosmic Ray
GOES	Geostationary Operational Environmental Satellites
GRS	Gamma ray Spectroscopy
HEND	High-energy Neutron Detector
HEPAD	High-energy Proton and Alpha Detector
HP ³	Heat Flow and Physical Properties Package
HPGe	High-Purity Germanium
HV	High-voltage

IMF	Interplanetary Magnetic Field
K-Ar	Potassium-Argon
LaBr ₃ (Ce)	Lanthanum Bromide
MARIE	Martian Radiation Environment Experiment
MCA	Multi-channel Analyser
MCNPX	Monte-Carlo N-Particle Transport Code
ME	Mount Erebus
MSL	Mars Science Laboratory
NS	Neutron Spectrometer
OU	Open University
PDS	Planetary Data System
PGAA	Prompt Gamma ray Activation Analysis
PMT	Photomultiplier Tube
ppm	Parts per million
ppb	Parts per billion
RTG	Radioisotope Thermal Generator
SCR	Solar Cosmic Ray
SE	Single Escape Peak
SEM	Space Environment Monitor
SPE	Solar Proton Event
TF	Theo's Flow
WF	Weight Fraction
XRF	X-ray Fluorescence Spectroscopy
Z	Atomic number

Chapter 1

Introduction

X-ray fluorescence (XRF) and γ -ray spectroscopy (GRS) have been used to determine the composition of planetary surfaces since the 1960s with the Apollo and Ranger missions to the Moon. The composition of a planet is a direct result of major solar system processes including (Kring et al., 1995):

- Planetary body evolution.
- Planetary differentiation (heating processes).
- Geological processes that build or alter surfaces (volcanic activity, meteorite impacts).
- Alteration and chemical processes (e.g. by liquid flows).
- Interactions between the surface and the atmosphere.
- Interactions with biological activity.

Knowledge of the composition and bulk density of a planetary surface is crucial to enable a complete understanding of the processes outlined above. Although extensive composition mapping has been carried out on the Moon and Mars (Prettyman et al., 2006; Boynton et al., 2007), there remains a great deal of uncertainty in the composition of many other objects and planets in the solar system (including Venus and the moons of Jupiter and Saturn). In addition, unreliable age estimates and heat flow estimates could also benefit from in-situ missions (where the instrumentation is installed on a surface or sub-surface

platform) whose observations will contribute to answering important questions relating to the planetary processes described above. The information that can be obtained using the techniques proposed in this thesis will constrain planetary heat flow estimates and provide invaluable data for planetary evolution models.

1.1 Objectives of Future In-situ XRF and GRS Missions

GRS is a well-established technique to determine the abundance of the major rock-forming and radioactive elements of a planetary body from orbit. Previous orbital missions using GRS instrumentation include 2001 Mars Odyssey (Boynton et al., 2007); Lunar Prospector (Prettyman et al., 2006) and the NEAR-Shoemaker asteroid rendezvous mission (Evans et al., 2001). However, GRS has only been carried out in-situ on the surface of Venus during the Russian Venera programme (Surkov, 1997a), although an in-situ GRS system was incorporated into the failed Mars-96 mission. Conversely, XRF is an in-situ (and orbital) technique that has been used on many planetary bodies including Mars (i.e. the alpha proton X-ray spectrometer on Mars Pathfinder (Reider et al., 1997) and the alpha particle X-ray spectrometer on the Mars Exploration Rovers Spirit and Opportunity (Gellert et al., 2004)). Composition data obtained on the surface can provide a ‘ground truth’ to orbital measurements. There is also interest in understanding the variation in composition with depth, a parameter never examined on any planetary science mission. A γ -ray spectrometer on a penetrator, mole or drill (collectively referred to hereafter as sub-surface probes) could examine the undisturbed sub-surface beneath any material that could have undergone weathering or alteration processes, allowing a more accurate view of the composition of the sub-surface of a planetary body (Kring et al., 1995). A sub-surface probe-based γ -ray

spectrometer would be able to take measurements as a function of depth, rather than relying on the attenuated emissions through the surface.

The bulk density profile (as a function of depth) constrains the geological interpretation of the data obtained from the examination of local deposits. For example; fluvial (liquid flows) and Aeolian (wind) activity, volcanism, glaciation and erosion, the depth distribution of loose deposits and bedrock, petrology and possibly sedimentary layering will all affect the bulk density profile of the near-surface of a planetary body. Bulk density measurements are very important when calculating planetary surface heat flow, a parameter that is poorly known for most planets except the Earth (Ambrosi et al., 2006; Ball et al., 1996; Hagermann, 2005; Spohn et al., 2001). γ -ray backscatter densitometry can create a bulk density profile of a planetary sub-surface and is described in Chapter 2, Section 2.7. A profile of the bulk density will provide an improved measure of the heat capacity of the crust as a function of depth and would be enhanced by knowledge of the composition of the surface (the heat capacity of a planetary body is dependent on its composition (Briggs et al., 2005; Healy et al., 1976)).

The age of the lunar surface is well-known given the large amount of remote sensing data of the cratering rate on the surface and age measurements of samples returned from the Luna and Apollo missions. There are large uncertainties in the boundary ages of the Martian epochs because the Martian cratering rate is poorly known and relative age estimates of the Martian epochs have been inferred from the Lunar cratering rate (Talboys et al., 2009). Swindle (2001) reported that uncertainties in the boundaries of epochs can vary by a factor of 2-4. In-situ dating measurements of a planetary surface will provide a

more precise estimate of planetary chronology. Knowledge of a planetary surface chronology can constrain planetary evolution models and the geological history of the planetary surface (i.e. to determine if and when volcanic activity occurred on the surface) (Hartmann and Neukum, 2001). Radiometric dating with γ -rays using the Potassium-Argon (K-Ar) method is evaluated in detail in this body of work (See Chapter 2, Section 2.8 and Chapter 8).

1.2 Background and Objectives of this Thesis

The Heat Flow and Physical Properties Package (HP³) was originally proposed by a team of European collaborators for a European Space Agency (ESA) Mercury lander technology development study. This package consisted of a mole that would penetrate beneath the Mercurian surface to a depth of ~ 5 metres. Once positioned, instruments on the mole would be used to estimate the planetary surface heat flow. The mole contained a γ -ray backscatter densitometer to calculate the bulk density of the surface of Mercury; the bulk density is required to determine the planetary heat flow accurately (Spohn et al., 2001). Although the Mercury lander was not selected for the BepiColombo mission, the breadboard programme continued with the development of the mole for use on other in-situ planetary missions. Work on the breadboard densitometer finished in 2006; however, the concept evolved into a geophysical package proposed by Ambrosi et al. (2006), that could simultaneously carry out GRS, γ -ray backscatter densitometry, radiometric dating and if required, XRF. The evolution of the sub-surface probe continued via an EPSRC Challenging Engineering award funding a research programme at the University of Leicester aimed at developing sensors for extreme environments. A collaboration with

EURORAD, France, promoted the development of the geophysical package. The analytical techniques described in Section 1.1 can be used to determine surface and sub-surface composition, constrain heat flow through a planetary regolith, determine the age of the planetary surface and hence understand more about the processes that formed planetary bodies. Ambrosi et al. (2006) proposed a possible configuration for the geophysical package housed in the HP³ mole (See Figure 1-1). Future missions whose scientific objectives could be met by the geophysical package include the MoonLITE penetrator mission or missions that form part of the Aurora or Cosmic Vision programmes. Targets for the Cosmic Vision programme include Europa and Titan where landers and penetrators are likely to play a role.

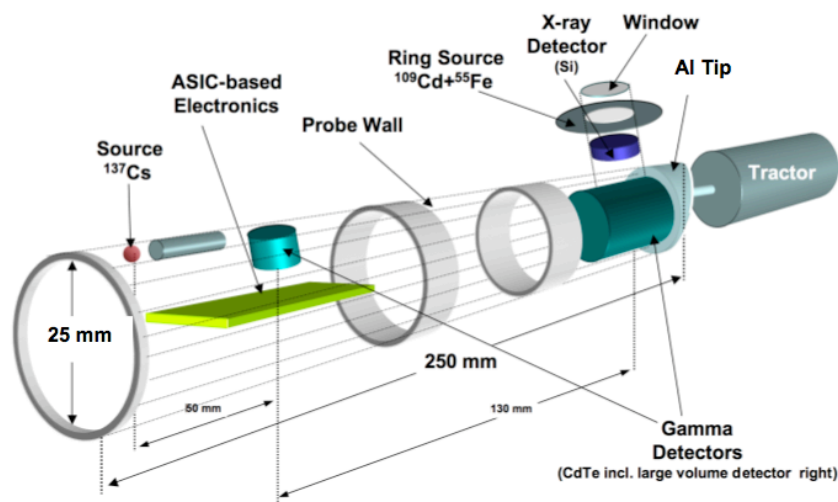


Figure 1-1. A schematic of the proposed design of the HP³ mole, featuring a suite of geophysical instruments. Taken from Ambrosi et al. (2006).

This thesis focuses on the development of the γ -ray detector component of the geophysical package that would measure the composition, bulk density and age of a planetary surface. A great deal of work has already been carried out in the area of XRF for planetary applications (e.g. Talboys, 2006; Rieder et al., 1997; Economou, 2001).

Chapter 2 describes the physics that governs the generation of X-ray and γ -rays on a planetary surface. It then will describe how these emissions can be used to determine the composition of a planet, how XRS and GRS are complementary to one another and how models are used to interpret the information detected by the X-ray and γ -ray instruments. The chapter also introduces the science objectives met by the use of GRS, including the concept of γ -ray backscatter densitometry, the importance of the bulk density in planetary heat flow calculations and how γ -ray techniques can be exploited to carry out radiometric dating of a planetary surface.

Chapter 3 describes the physical principles that are involved in X-ray and γ -ray detection, including the interactions that occur between X-ray photons, γ -ray photons and various detector materials. The properties and theory of operation of semiconductor and scintillator detectors for spectroscopic applications is discussed. Examples of the detectors used in previous interplanetary GRS missions are included.

Evaluating different detector types and configurations in order to achieve the scientific objectives described in Chapters 1 and 2 is a key enabling step for a successful flight instrument development programme. Chapter 4 describes the evaluation and comparison of different γ -ray detector solutions and configurations including: planar and hemispherical cadmium telluride, a caesium iodide scintillator, a lanthanum bromide scintillator and a high-purity germanium detector to determine the suitability of each detector option for an in-situ mission.

Chapter 5 describes a Monte Carlo planetary radiation environment model developed using the Monte Carlo N-Particle Transport Code (MCNPX), designed to investigate the expected performance of an in-situ geophysical package operating to a depth of up to 5 m. In this chapter the experimental verification of the model is also described. The first part of this chapter describes an experimental campaign at the ANTARES facility at the FRM-II neutron reactor, Munich, Germany. The aim of the campaign was to irradiate several Martian analogues and calibration samples with a thermal neutron beam to carry out some activation measurements. The second part of the chapter details the exploitation of the γ -ray data obtained from the experiment to verify the Monte Carlo model.

Chapter 6 describes the verification of the MCNPX planetary radiation environment model detailed in Chapter 5 using the γ -ray data acquired by the γ -ray spectrometers on 2001 Mars Odyssey and Lunar Prospector in orbit around Mars and the Moon.

Chapter 7 investigates whether the increased γ -ray emission from a planetary surface and atmosphere that results naturally from a solar proton event could be useful in future orbital and in-situ GRS missions, using data acquired by the γ -ray spectrometer on 2001 Mars Odyssey.

Chapter 8 details the modelling of the geophysical package on an in-situ mission (sub-surface probe or lander) using the planetary radiation environment model. It compares several types of neutron source including radioisotope and (α, n) sources for the geophysical package. It discusses the results of modelling the geophysical package,

including the limits of detectability of trace elements within a planetary surface using the geophysical package for GRS and the feasibility of radiometric dating.

In the final chapter the findings of this work are summarised and future work that may be undertaken with the aim of further developing the geophysical package is outlined.

Chapter 2

Background to X-ray Spectroscopy, γ -ray Spectroscopy, γ -ray Densitometry and Radiometric Dating

2.1 Introduction

This chapter details the physical processes that occur on a planetary surface to generate X-ray and γ -ray emissions. XRF and GRS are described, evaluated and compared as compositional analysis techniques. The importance of both orbital and in-situ GRS measurements is discussed and the concept of densitometry and radiometric dating using γ -ray techniques is also introduced.

2.2 Origin of Particles and Radiation that Interact with a Planetary Body

Planetary X-ray and γ -ray emission is generated when radiation or particles of solar, magnetospheric and galactic origin interact with a planetary body. The Sun emits a variety of particles and radiation. X-rays are emitted from the solar corona from regions that have temperatures of $\sim 10^6$ K (Okada et al., 2006). The X-ray flux from the Sun in the energy range 0.1 – 20 keV is large during quiet solar conditions; $\sim 10^8$ photons $\text{cm}^{-2} \text{s}^{-1}$ (Grande et

al., 2003). The flux and energy of the X-ray spectrum can increase significantly during solar flares (Okada et al., 2006). Particles (including protons, ions and electrons) are ejected from the Sun and contribute to the solar wind. Their energies are typically in the range of eV to keV (Hundhausen, 1995), and they have speeds of approximately 400 km s^{-1} when they reach the Earth (Barnes, 1992). Higher energy particles (MeV) are emitted from the Sun during a solar proton event (SPE) (See Chapter 7), but these are unpredictable and have varying fluxes and distributions. The particles emitted during a SPE can interact with a planetary body to produce X-rays and γ -rays.

Magnetospheres such as those of Earth and Jupiter feature radiation belts; these are composed of charged particles trapped within the magnetosphere (Wolf, 1995). The magnetic fields of these planets can accelerate the charged particles to high energies (e.g. in the Jovian magnetosphere, electrons can be accelerated to GeV energies, protons to 100s of MeV (Jun and Garrett, 2005)). These high energy particles are able to interact with Jovian moons that lie within Jupiter's magnetosphere such as Europa (Jun and Garrett, 2005) to produce X-rays and γ -rays.

Galactic cosmic radiation (GCR) that is composed primarily of protons (protons $\sim 87\%$, heavier ions $\sim 13\%$) and with energies ranging between 0.1 - 10 GeV/nucleon is also present in the solar system (and can therefore interact with planetary bodies in the solar system) with a flux of $\sim 2 \text{ protons cm}^{-2} \text{ s}^{-1}$ (Reedy and Arnold, 1972). The GCR flux and energy distribution is modulated by solar activity and can vary by up to a factor of 2 over a solar cycle.

2.3 Generation of X-rays

There are a number of mechanisms that generate planetary X-ray emission, including (Potts, 1987; Govil, 2001; Bhardwaj et al., 2007):

1. The interaction of solar X-rays with a planetary body or atmosphere. The X-ray photon is fully absorbed or scatters from an electron in an atom (X-ray fluorescence).
2. The interaction of charged particles with a planetary body, often known as particle-induced X-ray emission (PIXE). The charged particle collides with the inner shell electrons of an atom.
3. The interaction of fast (high energy) electrons i.e. electron-electron scattering with an electron in an atom.
4. Charge exchange of solar wind or magnetospheric ions with atmospheric neutrals.
5. Fast electrons can interact with a planetary body or atmosphere causing the production of continuum bremsstrahlung radiation.

When mechanisms 1-4 occur, the energy from the interaction of the charged particle/photon is imparted to an inner shell electron; it vacates the shell and the atom is left in an unstable state. To stabilise itself, the remaining electrons are rearranged to fill the gap left by the electron (Potts, 1987). The atom loses the excess potential energy created by an outer electron filling an orbital gap via X-ray emission (in the case of mechanism 1, the re-emitted X-ray is known as a secondary or fluorescent X-ray).

2.4 Generation of γ -rays

There are a number of mechanisms that generate planetary γ -ray emission, including (Boynton et al., 2004):

1. Charged particle (protons and electrons) scattering, or capture by the nucleus of an atom. The interaction of the high energy particle with the nucleus leaves it in an excited state and γ -ray emission occurs to return the nucleus to its ground state.
2. The interaction of secondary particles with a planetary surface (such as neutrons created from proton interactions). When solar and GCR particles directly interact with a planetary atmosphere or surface, a complex series of interactions occur (including spallation, ionisation, scatter and absorption; these and other reactions are detailed in Krane (1988)). Spallation can occur if a proton of sufficient energy interacts with the nucleus of an atom (See Figure 2-1). The interaction causes the expulsion of large numbers of nucleons. Many of these ‘secondary’ particles are neutrons.

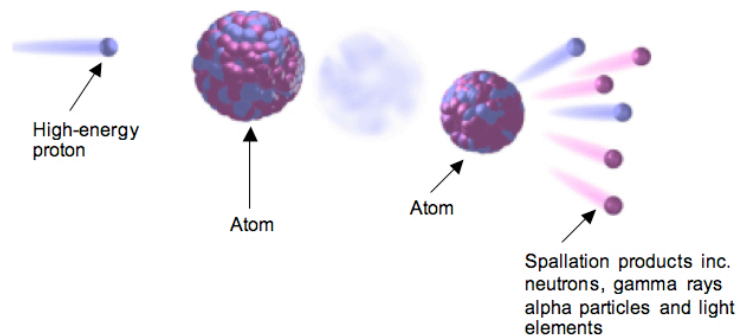


Figure 2-1. A diagram of the processes involved in a spallation reaction. Adapted from URL: www.sckcen.be/myrrha/images/spallation.png.

A high energy proton hits an atom and causes the expulsion of large numbers of nucleons from the nucleus. The greatest number of spallation products occurs for the heavier elements such as Fe and Ti. Spallation reactions occur when solar and GCR protons have energies higher than several 10s of MeV (Boynton et al., 2004).

Boynton et al. (2004) estimated that ~ 10 neutrons are produced per primary GCR particle. The neutrons undergo further interactions with matter (See Figure 2-2) including inelastic scattering or capture (See Figure 2-3). High energy neutrons undergo scattering reactions with the matter in the surface, losing energy until they reach thermal energies (< 1 eV) and undergo neutron capture. The interaction of the neutron with a nucleus (via capture, inelastic scatter or non-elastic scatter) can leave the nucleus in an excited state; the de-excitation process often results in the emission of a particle or γ -ray and in the case of inelastic scattering the re-release of a neutron at a lower energy (Kaplan, 1963). This is the primary mechanism for the creation of γ -rays on a planetary surface.

3. γ -rays are released when atoms undergo natural radioactive decay processes such as spontaneous fission and α decay (e.g. ^{40}K , ^{232}Th and ^{238}U) (Boynton et al., 2004).

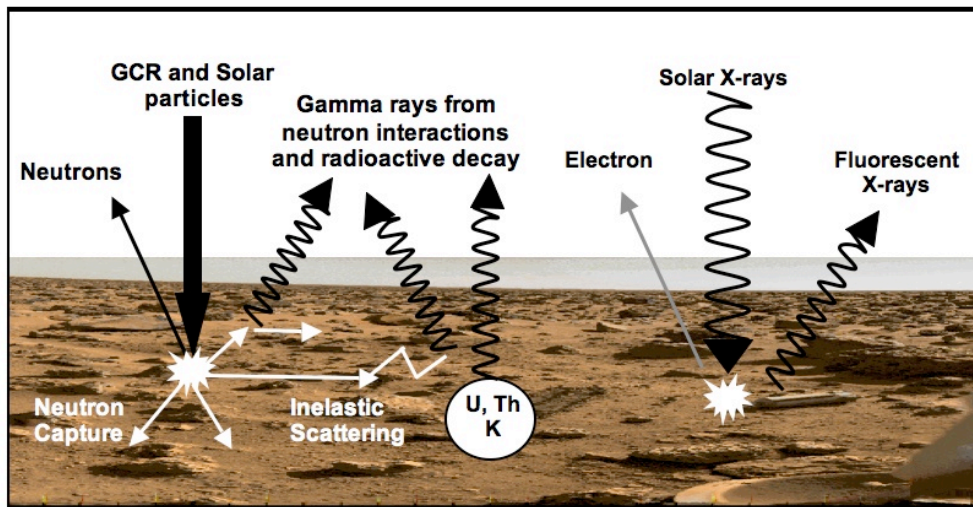


Figure 2-2. Diagram showing possible interactions of protons and solar X-rays with a planetary surface to produce γ -rays and X-rays.

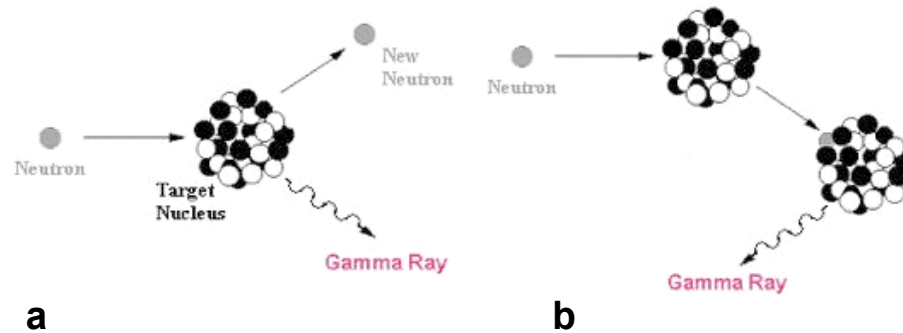


Figure 2-3. Two of the possible neutron interactions with an atom, a) inelastic scattering, b) neutron capture. Adapted from Brookshaw (2006).

Inelastic scatter is where a high energy or ‘fast’ neutron (MeV) scatters from an atom. Some of the neutron’s energy is passed to the atom, leaving it in an excited state, and the atom emits a γ -ray to return to its ground state. In neutron capture a thermal neutron (< 1 eV) is captured by the atom to create a new isotope. This isotope is in an excited state and emits a γ -ray to return to the new isotope’s ground state.

The interaction length (the mean free path of a particle to reduce its energy by a factor of $1/e$) of a proton depends on the proton’s energy. Low energy protons have small interaction lengths, but those of GeV energies can penetrate several metres into matter e.g. in silica of density 2.33 g cm^{-3} , protons of keV energies (solar wind protons) have ranges (or mass thicknesses) of $\sim 10^{-5} \text{ g cm}^{-2}$ and protons of GeV energies (GCR protons) have ranges of 10^2 - 10^3 g cm^{-2} (Berger et al., 2005). The Moon has a negligible atmosphere and a negligible magnetic field, therefore all of the solar wind and GCR protons are able to interact with the Lunar surface directly. The Martian atmosphere, although thin, significantly attenuates the proton flux below 100 MeV, so only GCR protons and high energy protons released during a SPE (hereafter called solar cosmic ray (SCR) protons) are able to interact with the surface. A Monte Carlo model that simulates the Martian

atmosphere and surface is discussed in detail in Chapter 6. It indicates that protons of < 100 MeV are attenuated in the atmosphere (See Figures 2-4 and 2-5). As a result, normal solar protons that constitute the solar wind do not create a significant amount of γ -ray emission from the surface of Mars. In contrast, the SCR and GCR protons are able to directly interact with the sub-surface because their typical energies are higher. The Earth's atmosphere is thicker (1033 g cm^{-2} (Masarik and Reedy, 1995)) than the Martian atmosphere ($\sim 20 \text{ g cm}^{-2}$ (Masarik and Reedy, 1996)), as a result only high energy GCR protons, and SCR protons accelerated by large SPEs (GeV) can reach the surface of the Earth.

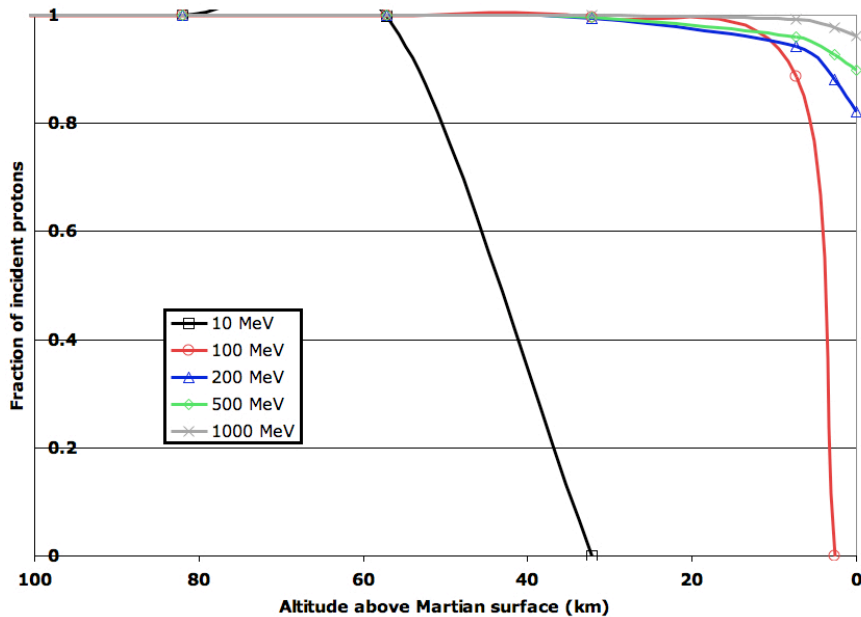


Figure 2-4. The fractional proton penetration through the Martian atmosphere obtained via the Monte Carlo model described in Chapter 6. Protons of < 100 MeV do not survive to the Martian surface.

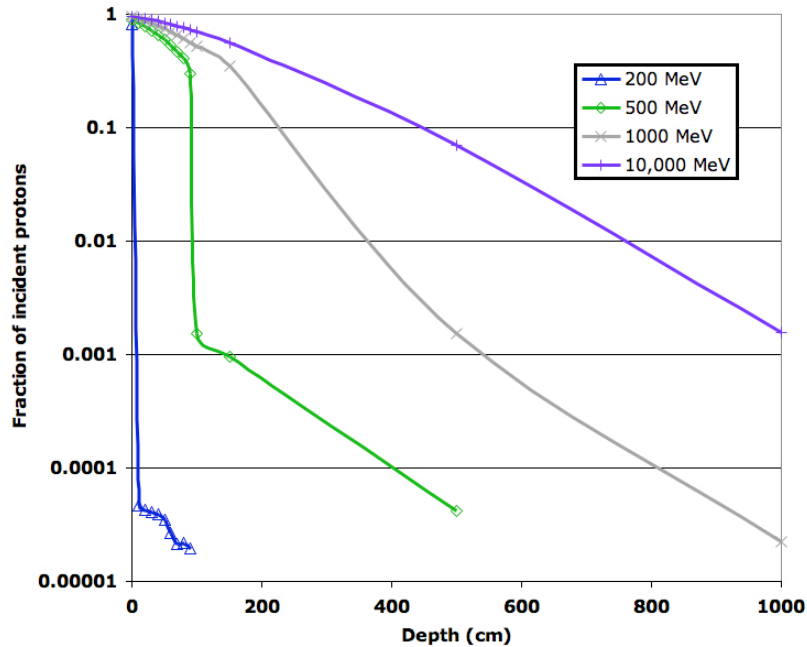


Figure 2-5. Fractional proton penetration into the Martian surface obtained via the Monte Carlo model described in Chapter 6. Protons under 100 MeV do not survive to the surface. The higher the proton energy, the greater the penetration into the Martian surface.

2.5 X-ray and γ -ray Spectroscopy

2.5.1 X-ray Fluorescence Spectroscopy

The X-ray spectrum emitted from a planetary surface ranges between 1 keV and 100 keV (Yin et al., 1993). The strength of these emissions is strongly dependent on the chemical composition of the surface as well as on the incident high energy particles/ radiation. The X-ray fluorescence counts are not directly proportional to the concentration of the element in the planetary surface, but must be corrected for absorption enhancement effects, i.e. the other elements in the sample can absorb these X-rays. An X-ray fluorescence spectrometer in orbit or in-situ may be used to detect these emissions and the count rate in the detector of each X-ray peak may be used to determine the composition of the surface. The type of

X-ray spectrum obtained from a particular element is dependent on its atomic number and is elementally specific (Potts, 1987).

If the X-ray spectrometer is placed in-situ, then the fluorescence may be increased using a radioactive source that emits X-rays or an X-ray tube (Potts, 1987). The first XRF measurements taken of another planet from orbit were of the Moon by the command modules of Apollo 15 and 16. However, little scientific information was gathered about the Moon. The problem with XRF using naturally created emissions is that the solar X-rays emitted from the Sun can be six times more intense than the emission of fluorescent X-rays from the surface (Yin et al., 1993), therefore it can be difficult to isolate these emissions above the background. In addition, the intensity and energy distribution of the emission from the Sun is highly variable, requiring the use of X-ray detectors monitoring the solar X-ray emissions to accurately interpret any XRF spectra. The only elements that can be analysed in orbit about a planet with a thin or no atmosphere are Mg, Si, and Al (Yin et al., 1993). If there is high solar activity it is possible to detect Ti and Fe using XRF (Okada et al., 2006).

XRF can be used to calculate the concentration of many rock-forming elements, and a large number of trace elements, down to parts per million (ppm) or parts per billion (ppb) (Potts, 1987). The most prominent elemental fluorescent lines are the $K\alpha$ lines (when the incident X-ray interacts with an electron in the K-orbital shell); Table 2-1 shows a few examples of fluorescent lines for the major rock-forming elements.

Element	Energy of K α line (keV)
Mg	1.254
Al	1.487
Si	1.740
Ca	3.691
Ti	4.508
Fe	6.403
O	0.530

Table 2-1. K α lines of interest from major rock-forming elements (Starr et al., 2001).

2.5.2 γ -ray Spectroscopy

The γ -ray spectrum emitted from a planetary surface ranges between 200 keV and 10 MeV (Boynton et al., 2004). The composition of the surface and sub-surface of a planet can be extracted from the measured γ -ray spectra, given that the energy of the γ -rays emitted by these mechanisms are element specific. In addition, the intensity of a γ -ray line is proportional to the concentration of the associated element in the surface, sub-surface or atmosphere of a planet. The energy of the major neutron capture and inelastic scattering γ -rays for the major rock-forming elements is shown in Table 2-2. A neutron source may be used to augment the natural γ -ray emission from the planet if the mission is in-situ. Although neutron sources were previously bulky, developments in technology have allowed neutron sources to become more compact (Ambrosi et al., 2005). This will be discussed further in Chapter 8.

Element	Energy of γ -ray (MeV)	
	Inelastic Scatter	Neutron Capture
Mg	1.368	0.585
Al	2.210	7.724
Si	1.779	3.539
Ca	3.737	1.943
Ti	0.984	1.381
Fe	0.847	7.631
O	6.129	0.870

Table 2-2. γ -ray emission lines from neutron capture and inelastic scatter reactions with major rock-forming elements (Masarik and Reedy, 1996).

2.5.3 X-ray versus γ -ray Spectroscopy

In-situ XRF has been used on many planetary science missions, such as the Venera missions on Venus (Surkov, 1997b), the Mars Pathfinder (Reider et al., 1997) and Viking missions to Mars (Surkov, 1997b). It requires the presence of an X-ray source, such as ^{55}Fe , ^{109}Cd , ^{241}Am or a combination of these in order to produce the X-rays that will interact with the surface. The presence of an X-ray source rather than relying on natural planetary emissions means that the spectral acquisition times (to obtain peaks with a given level of precision) are seconds to hours depending on the strength of the X-ray source. Recent GRS missions have focused on orbital measurements such as 2001 Mars Odyssey and Lunar Prospector; however, in-situ GRS has been carried out on the surface of Venus as part of the Venera programme and was planned on the surface of Mars as part of the failed Mars-96 mission (Surkov, 1997a). A neutron source such as ^{252}Cf or Am-Be may be used to increase the γ -ray emission from the surface of a planet if the instrumentation was in-situ.

XRF can only determine the composition of a planetary surface to a depth of a few millimetres. In silica of density 2.33 g cm^{-3} , 20 keV X-rays have an interaction length of the order of millimetres; 6 keV X-rays have an interaction length of the order of microns (Hubbell and Seltzer, 2004). The composition derived from XRF is not always an accurate determinant for the composition of the whole surface as the surface is usually more oxidised and weathered than the material below. γ -ray emissions can be used to determine the bulk composition of a planet because the interaction length of γ -rays are longer (in silica of density 2.33 g cm^{-3} , 20 cm at 200 keV and 1 m at 10 MeV (Hubbell and Seltzer, 2004)). To examine the unaltered regions of a planetary regolith, it is necessary to probe at depths greater than 2 m; or in the case of a rover to find a suitable outcrop, which is not always possible. X-ray techniques would rely on some form of sample retrieval system.

The small interaction length ($\mu\text{m} - \text{mm}$) of X-rays also has implications for the configuration of the sub-surface probe. XRF techniques are often limited by the presence of protective windows that limit the performance of the instruments by introducing a low energy cut-off which is usually around 1 keV for typical Be windows (Ambrosi et al., 2005; Jenkins, 1999a). The exclusion of windows from detectors for XRF can enhance their performance and could enable the detection of elements such as C (280 eV) depending on the signal to background and noise associated with the detector system. However, X-ray detectors without windows have to be custom made (Ketek, 2008). The exclusion of a window increases the risk of damage to a detector; in addition the detector becomes sensitive to light. There are significant engineering challenges associated with the inclusion of a windowless detector in a surface or sub-surface probe, which could be avoided if using γ -rays. The interaction length of γ -rays do cause a disadvantage to the technique; the

detectors required for GRS need larger volumes than those used in XRF. This increases the mass of the instrument; which is undesirable in remote sensing missions where mass is restricted.

The amount of compositional information that can be gathered using XRF tends to be limited to the major rock-forming elements (Si, Ti, Mg etc.) (Surkov, 1997b). GRS can detect all major rock-forming elements and can also detect light elements such as H, C, N, P and B. Both techniques can detect elements that are present in trace amounts (ppm, ppb) (Jenkins, 1999b). Since the two techniques probe different areas of the surface composition (XRF probes the composition of the outermost layers of the surface that have undergone weathering effects and GRS the composition of the unaltered surface to a depth of several metres), XRF and GRS are complementary and can be used simultaneously to maximise the data that could be obtained from a sub-surface probe or lander. Although it is desirable to have a geophysical package capable of carrying out both techniques there are mass and power constraints to consider, therefore in this thesis the XRF capability is considered to be optional in the package and is not discussed any further in this work.

2.6 Orbital versus In-situ γ -ray Spectroscopy

The limitations of orbital XRF compared with in-situ XRF were discussed in Section 2.5.1. To get a complete view of the surface composition and planetary formation processes, both orbital and surface measurements are required. In particular in-situ GRS is complementary to orbital GRS because:

- In some cases orbital measurements have to be corrected for atmospheric absorption effects where an atmosphere is present, such as Mars; this is not the case for in-situ measurements.
- While the orbital measurements give an average composition over a large area, in-situ measurements can give detailed compositional information over an area of a few square metres (in several locations if the γ -ray spectrometer is installed on a lander).
- To date orbital measurements have provided compositional maps of the Moon and Mars with a spatial resolution of hundreds of kilometres. In-situ observations can localise heterogeneities (such as water deposits or precipitates) on a much finer scale from centimetres to metres (Kring et al., 1995).
- An in-situ γ -ray spectrometer could identify diurnal or seasonal variations in the composition. For example, CO₂ ice covers larger areas of the poles during a Martian winter.
- A sub-surface probe could examine the undisturbed surface, beneath any material that has undergone weathering processes. This gives a more accurate view of the composition of the sub-surface of a planet (Kring et al., 1995). The γ -rays emitted by the deeper surface material are attenuated as they travel to the surface so less compositional information can be gathered at depth on a lander or orbital-based spectrometer. A sub-surface probe would not have this problem because it would be making measurements at a depth where those γ -rays are created.
- If the sub-surface probe is a drill rather than a penetrator, it may be possible to collect spectra at varying depths thus gaining a depth profile of the composition.

- A sub-surface probe-based γ -ray detector would have a larger surface area exposed to the γ -ray emitting surface material because it would be completely surrounded by it as opposed to a lander or orbital spectrometer that would have only one side of a detector crystal exposed to the surface. This would increase the overall counts in the detector, thus improving the counting statistics.
- If the geophysical package being developed at the University of Leicester were installed on a sub-surface probe, the addition of a small ^{137}Cs source could extend the γ -ray spectrometer's capabilities to include γ -ray backscatter densitometry to allow calculation of the bulk density of the sub-surface of a planetary body. This is discussed further in Section 2.7.

2.7 γ -ray Backscatter Densitometry

The technique of using γ -ray or Compton backscatter densitometry to get an estimate of the density of a medium has been used in several terrestrial applications, including well logging by the oil and gas industry (Ambrosi et al., 2006). It has also been used in the 1960s and 1970s in the Soviet Union to measure the surface density of Mars, the Moon and Venus (Surkov, 1997a).

A planetary sub-surface preserves information of the geological and climatic evolution of the planet. The sub-surface of Mars is known to contain water ice (Ambrosi et al., 2006), and it may therefore provide a habitable environment. The geophysical package deployed on a sub-surface probe would enable the geophysical and geochemical profiling to depths of up to 3 m at the target site. Previous ground penetrators have only been able to profile up

to 30 cm depth (e.g. the Viking missions on the surface of Venus) (Ambrosi et al., 2006). The oxygen extinction depth is an important parameter in determining the required sampling depths on Mars to find putative organic material. Chemical weathering occurs on Mars in the form of oxidation, and many oxides are created, such as ferric oxides and sulphates. In order to sample the un-oxidised surface, it is necessary to penetrate the surface by several metres because oxygen can diffuse into the soil, and meteorite impacts allow already oxidised soil to be buried and brings un-oxidised material to the surface. The oxidant extinction depth is defined as the depth where the oxidising agent concentration reaches zero, which on Mars is between 2 m and 5 m (Lammer et al., 2003).

2.7.1 Heat Flow Measurements: The Importance of Accurate Bulk Density Calculations

The thermal conductivity of the regolith is dependent on its bulk density (Healy et al., 1976; Briggs et al., 2005). Combining the mechanical and bulk density information with thermal measurements allows the heat flow of the surface and sub-surface of a planet to be estimated. Surface heat flow information constrains thermal evolution models and planetary composition models because it provides an upper limit to the abundance of radioactive elements, which generate heat in a planetary surface. The variation in heat flow of a planetary surface can also reflect the tectonic activity on the planet, since the heat flow will increase towards young planetary crustal regions where volcanic activity is more likely.

Surface heat flow is poorly known for the other planetary bodies in the solar system, including the Moon. Apollo 15 and 17 made the first heat flow measurements on the Moon

using a penetrator. The surface heat flow was estimated to be 21 mW m^{-2} and 16 mW m^{-2} respectively at the two different landing sites. However, both locations of measurement were located near the highland-mare boundary and were not representative of the entire planet. Warren and Rasmussen corrected these values in 1987 to give a global mean of 12 mW m^{-2} in 1987 (Warren and Rasmussen, 1987).

The ESA Rosetta mission includes the Multi-Purpose Sensors for Surface and Subsurface Science (MUPUS) instrument (Spohn et al., 2007), which will measure heat flow on the comet Churyumov- Gerasimenko using a penetrating device and the future ExoMars mission to Mars may contain a heat flow measurement instrument on the Humboldt payload. However, neither of these missions contain accurate systems of measuring the surface density as a function of depth. A bulk density profile with depth of a planetary sub-surface is essential to get an accurate estimate of planetary surface heat flow (Briggs et al., 2005; Healy et al., 1976), and estimates have to be obtained from several locations on the planetary surface to get a complete picture of the global surface heat flow.

A γ -ray backscatter densitometer measures the intensity of backscattered or Compton scattered γ -rays from a source of known activity that have travelled into the medium surrounding the detector. When γ -rays Compton scatter in a material, they impart a fraction of their energy to the electron they are scattering from. The probability of Compton scattering occurring in a material is proportional to the number density of electrons in the material. Therefore, since the electron number density is proportional to the mass density of the material we can relate the intensity of backscattered γ -rays into a detector to the density

of the medium surrounding it. The intensity of the γ -rays measured by the detector is dependent on (Ball et al., 1996):

- a) The density of the medium surrounding the detector.
- b) The distance between the source and the detector- the sonde length.
- c) The characteristics of the detector, such as the efficiency (See Chapter 3, Section 3.6).
- d) The source activity.

Figure 2-6 demonstrates how the Compton backscattering count rate of a detector varies with density for detectors with two different sonde lengths. When the density is low, there is a low scattering probability; therefore the count rate is low. As the bulk density increases the scattering probability increases up to a critical density. Above the critical bulk density attenuation by the surrounding medium starts to dominate over the scattering, causing the count rate to decrease. A calibration curve of the Compton backscattering count rate against materials of known density can be used to interpret the remote data obtained by the densitometer on the surface of another planet, converting it into an estimate of the bulk density of the surface (Hearst and Carlson, 1969). As can be seen in Figure 2-6 there can be two possible densities for a given backscattered count rate which introduces uncertainty. The solution to this is to use a two-detector system. The critical density for the longer sonde is smaller than the shorter sonde because the γ -ray intensity has a $1/e$ dependence on the thickness of the medium. By taking the ratio of the count rates of the two detectors a single density is obtained for a given backscattered count rate.

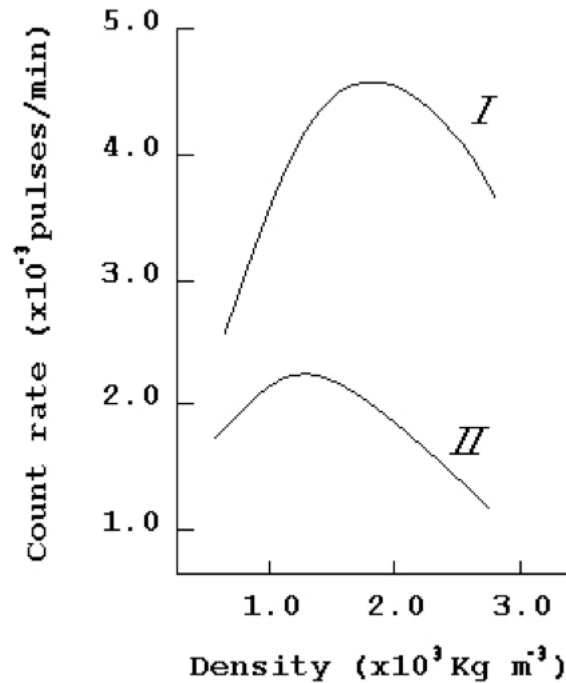


Figure 2-6. How the γ -ray count rate in a given energy window for two detectors at different fixed positions relative to the source varies with density. Detector I has a sonde length that is smaller than detector II. Taken from Ambrosi et al. (2007).

Venera 10, a Soviet probe that landed on Venus in 1975, made use of this technique to estimate the density of the Venusian surface (Surkov, 1997a). γ -rays emitted from a ^{137}Cs source were scattered by the Venusian rock and were recorded by three different detectors at different distances to the source, and the count rates were used to derive the surface density, $\rho = 2.8 \pm 0.1 \times 10^3 \text{ kg m}^{-3}$ (Surkov, 1997a).

2.7.2 γ -ray Backscatter Densitometer

A schematic of the original configuration of the HP³ mole is shown in Figure 2-7.

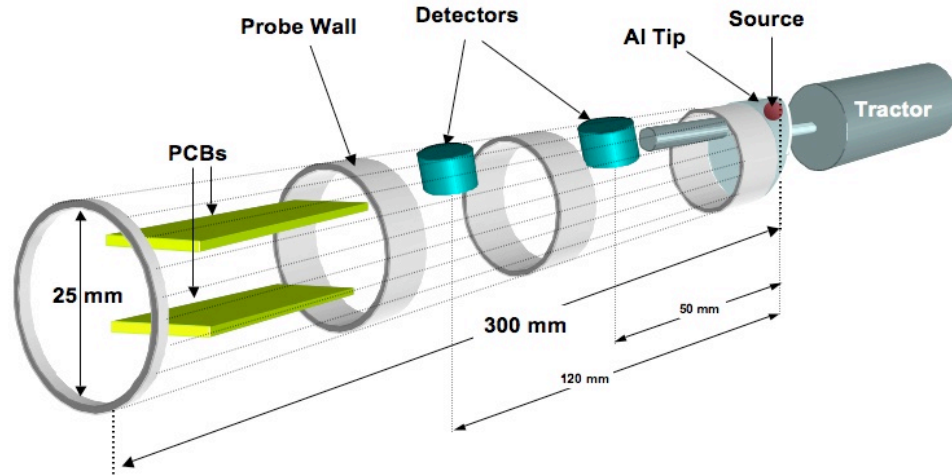


Figure 2-7. Schematic of the original HP³ densitometer. Taken from Ambrosi et al. (2006).

A ^{137}Cs source was included in the mole, which emitted 662 keV γ -rays into the material surrounding the mole. The backscattered spectrum from the medium surrounding the mole that is collected by the densitometer is shown in Figure 2-8. The integrated counts in a selected region of this spectrum were used as a measure of the density of a surrounding material. This ‘Compton window’ extended from 250 keV – 450 keV. This energy range was chosen because it limited the γ -rays counted to those that had undergone minimal scattering interactions (the single scatter plateau region indicated in Figure 2-8).

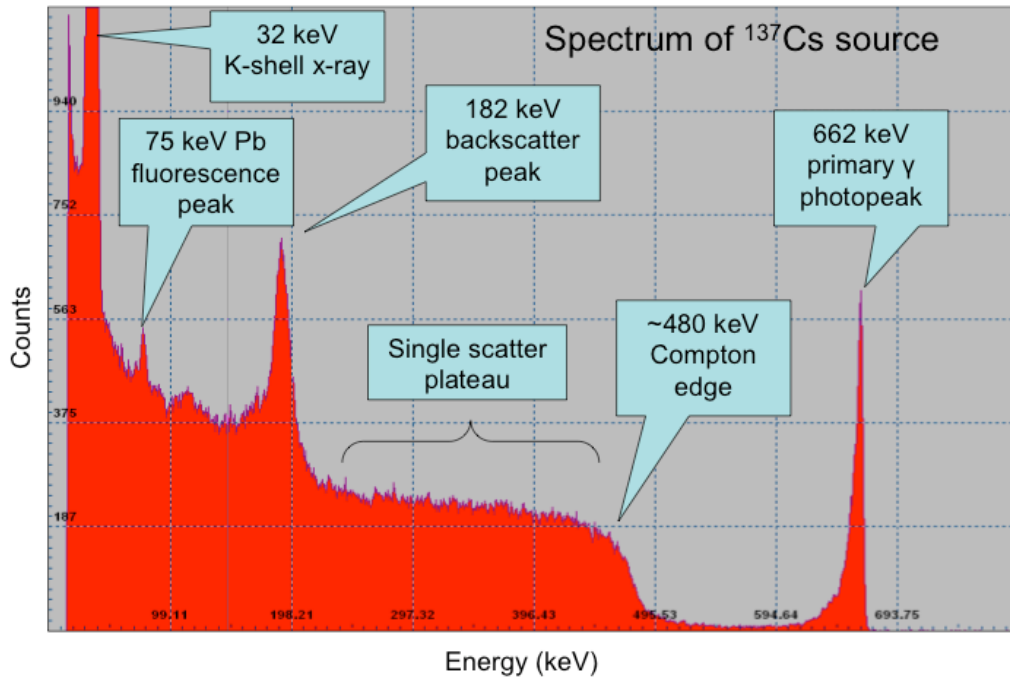


Figure 2-8. Diagram showing the Compton window in a ^{137}Cs spectrum. Taken from Ball et al. (2007).

The spectrum contains several features; the 32 keV X-ray produced by the decay of ^{137}Cs , the 65 keV X-ray fluorescence peak created by the excitation of the surrounding material (lead), the backscatter peak (the energy that most Compton scatter γ -rays have after scattering), the single scatter plateau region, the Compton edge (the maximum energy a γ -ray may have after scattering from the surrounding medium) and the main ^{137}Cs γ -ray decay peak (which may be used for energy calibration).

Two 75 mm³ CdTe γ -ray detectors were used to obtain two independent measurements on the density. The mole contained 13 Tungsten shielding disks of \varnothing 5 mm x 5 mm that were placed directly above the source to prevent the scattering signal from being shadowed by the main photopeak from the source.

In 2006, an extension of the capability of the densitometer was proposed by Ambrosi et al. (2006). The small volume CdTe detectors were replaced by two large volume detectors so

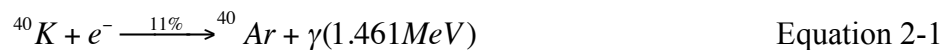
that the feasibility of the densitometer (renamed the geophysical package) to carry out GRS and radiometric dating could be investigated (See Figure 1-1). A full description of the densitometer experimental work and the modelling results is given in Ambrosi et al. (2006, 2007) and Ball et al. (2007), therefore the densitometer aspect of the geophysical package is not discussed any further in this work.

2.8 K- Ar Radiometric Dating

The lunar surface is well characterised in terms of its age and the cratering rate from remote observations of the surface, and samples returned from the Luna and Apollo missions. However, the Martian cratering rate is poorly known and there are large uncertainties in the boundary ages of the Martian epochs (Talboys et al., 2009) because the estimates have been inferred from the Moon. K-Ar dating can be carried out remotely to estimate the age of a planetary surface.

2.8.1 The K-Ar Radiometric Dating Technique

Radioactive K (^{40}K) comprises 0.012 % of natural K. About 11 % of ^{40}K decays involve electron capture to create ^{40}Ar and the atom also emits γ -ray of 1.461 MeV (Dickin, 2005), according to the following reaction:



The decay constant for this reaction is $0.581 \times 10^{-10} \text{ yr}^{-1}$ (Dickin, 2005). ^{40}K can also decay into ^{40}Ca via β emission (the probability of this mode of decay is 89 %). The decay constant is $4.962 \times 10^{-10} \text{ yr}^{-1}$ (Dickin, 2005).



Therefore the total amount of ^{40}Ar present in a sample is governed by the equation:

$$^{40}\text{Ar}_{\text{total}} = ^{40}\text{Ar}_i + \frac{\lambda_{\text{ec}}}{\lambda_{\text{total}}} K (e^{\lambda_{\text{total}} t} - 1), \quad \text{Equation 2-3}$$

where $^{40}\text{Ar}_i$ is the ^{40}Ar present in a sample that originated from the formation of the rock or surface sample, λ_{ec} is the decay constant for electron capture, λ_{total} is the sum of the decay constant from the two decay modes that occur (Equations 2-1 and 2-2), ^{40}K is the amount of ^{40}K present in the sample of interest at time t . Since ^{40}Ar outgases when the surface is heated, it is assumed that all of the ^{40}Ar out gassed when the sample was formed, therefore $^{40}\text{Ar}_i$ is negligible.

^{40}Ar is not a natural constituent of rocks and planetary surface material, however non-radiogenic ^{40}Ar content (as opposed to radiogenic ^{40}Ar created by radioactive decay) can be present in the rocks that originated from the Martian atmosphere and ^{40}Ar loss is possible through weathering. Careful background subtraction is required for this method to be accurate. If the interior of the sample can be examined, then non-radiogenic ^{40}Ar from weathering should be negligible. When K-Ar dating on the Earth, non-radiogenic ^{40}Ar is accounted for in a sample by examining the concentration of ^{36}Ar ; the ratio of ^{40}Ar to ^{36}Ar is 296 on the Earth, therefore this knowledge can be used to subtract non-radiogenic ^{40}Ar

from the concentration estimates of radiogenic ^{40}Ar . On Mars the ratio of ^{40}Ar to ^{36}Ar is not as well established but has been estimated to be between 1700 and 1900 (Dicken, 2005; Talboys et al., 2009).

2.8.2 Previous Methods of Remote K-Ar Radiometric Dating

Radiometric dating of Mars using the K-Ar method was planned on the ill-fated Beagle-2 mission, and it will not be attempted again until the NASA Mars Science Laboratory (MSL) lands on the Martian surface in 2012. The Beagle-2 mission (and the future MSL mission) relied on two remote techniques to carry out K-Ar dating; XRF to determine the concentration of ^{40}K and mass spectroscopy (specifically a Gas Chromatograph Mass Spectrometer) to determine the concentration of ^{40}Ar and ^{36}Ar in a given Martian surface sample (Talboys et al., 2009). Talboys et al. (2009) carried out dating on analogues using flight similar hardware and found that they could only determine the ages of the analogues to a precision of 30 %.

GRS can determine the concentration of ^{40}K via the detection of the γ -rays emitted via radioactive decay (Equation 2-1). If the signal to background ratio is large in the γ -ray spectrum acquired on a planetary surface, then the concentrations of ^{40}Ar and ^{36}Ar may be determined via the γ -rays emitted from neutron capture by ^{40}Ar and ^{36}Ar . The feasibility of using GRS to determine the concentrations of ^{40}K and ^{40}Ar , and therefore whether GRS can carry out K-Ar radiometric dating of the Martian and other surfaces to a better level of precision that already exists is addressed in Chapter 8.

2.9 Summary

In this chapter the importance of making detailed compositional, bulk density and dating estimates of a planetary regolith in-situ has been explained. These measurements constrain planetary heat flow estimates, provide a 'ground truth' to orbital measurements and to determine the ages of planetary surfaces. A comparison of the techniques of XRF and GRS has been made, including a discussion on the complementary aspects of the two techniques. The technique of exploiting the γ -ray backscatter of a source from the material surrounding it has been described as an accurate method to measure the bulk density of a planetary regolith. The concept of radiometric dating using the K-Ar method has also been introduced.

Chapter 3

X-ray and γ -ray Detectors

3.1 Introduction

The first γ -ray spectrometers were used in the Ranger missions to the Moon in the 1960s. Ranger 3 was designed to make measurements of Lunar γ -ray emissions using a scintillator-based γ -ray spectrometer. Ranger 3 missed the Moon due to a series of malfunctions; however, the γ -ray detector did observe the γ -ray emissions from the Lunar surface for approximately 40 hours (Surkov, 1997a). In 1966, Luna 10 carried out the first investigation of X-ray radiation originating from the Moon (Surkov, 1997b). Since then many planetary science missions have utilised XRF and GRS to determine the compositions of a planetary surfaces, using scintillator or semiconductor detectors. In this chapter the elements that comprise an X-ray or γ -ray spectrometer are introduced. The theory of the operation of semiconductors and scintillators is discussed, and how their properties make them suitable for spectroscopic applications. The advantages and disadvantages of using different types of scintillator and semiconductors are explained and a section is included that details several examples of γ -ray detectors that have been used on interplanetary remote sensing missions.

3.2 The Detector System

A block diagram of a traditional detector system is shown in Figure 3-1 (hereafter referred to as the spectrometer). A detector system includes the detector element or crystal (hereafter referred to as the detector), the preamplifier, main amplifier, the multi-channel analyser (MCA) and the power/bias supply.

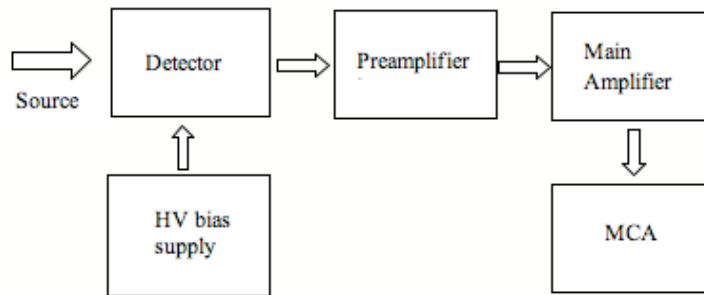


Figure 3-1. Block diagram of the elements that comprise a spectrometer. The analog to digital converter (ADC) is usually incorporated into the MCA.

The energy of the γ -ray or X-ray photon is absorbed by the detector and physical processes occur (to be detailed in Sections 3.4 and 3.5) that result in the output of a current pulse, which is proportional to the energy of the photon. The preamplifier converts the current pulse into a voltage pulse, and carries out some basic shaping. The pulse is then passed to the main amplifier where it is amplified and shaped according to the user-designated shaping time. The shaping time is related to the properties of the detector (Knoll, 1999a) and can be used to discriminate between detected events and noise. Noise is introduced by the electronic components of the system and the detector itself (Section 3.4.3). Pile up occurs when the count rate of the detector is greater than the preamplifier response time for

each event. The detector ‘dead time’ is the time in which events are not processed due to this pile up.

The MCA converts the amplitude of the signal into a digital signal that is proportional to the pulse height. The signal is then assigned to the appropriate channel number according to the size of the digital signal (the size of the digital signal is proportional to the original γ -ray energy). The output is a histogram/spectrum of the number of photons per energy interval absorbed into the detector. Figure 3-2 shows a block diagram of the stages of the pulse processing. The preamplifier, amplifier and MCA will be referred to collectively as the detector electronics in this work.

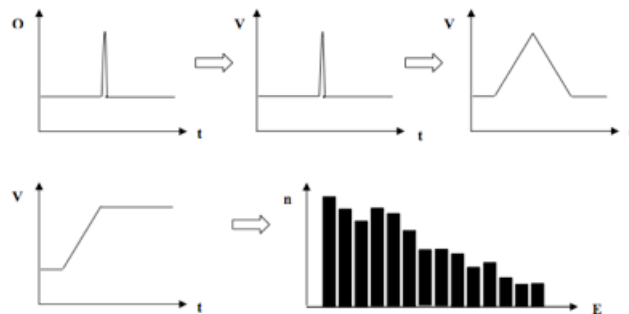


Figure 3-2. A block diagram to show the stages in the signal processing of the photon interaction with the detector. Taken from Ball et al. (2007).

The charge pulse is converted to a voltage pulse in the preamplifier and shaped in the main amplifier. It is then converted into a digital signal in the MCA and allocated to the relevant channel according to the size of the pulse (the energy of the incident γ -ray). The output is a histogram/spectrum of the number of photons detected per channel or energy interval.

3.3 Photon Interactions with the Detector

The photon absorption through matter is governed by Equation 3-1 (Siffert and Coche, 1968a):

$$N = N_o \left[1 - \exp\left(-\frac{\rho\sigma_{tot}}{uA} x\right) \right], \quad \text{Equation 3-1}$$

where N is the number of photons absorbed, N_o is the initial number of photons entering the detector, x is the thickness of the detector crystal, ρ is the density of the matter, σ_{tot} is the total cross section per atom (which is a sum of three contributions, the photoelectric absorption cross section, the Compton scattering cross section and the pair production cross section), u is the atomic mass unit, 1.66×10^{-24} g and A is the atomic mass.

In photoelectric absorption, a photon incident on the detector is absorbed by an electron, causing the ejection (ionisation) of the electron from the atom. The electron's kinetic energy is equal to the energy of the photon minus the binding energy (or ionisation potential) of the electron. The electron can then excite other electrons via collisions. The photoelectric absorption cross section (σ_{PE}) is given by:

$$\sigma_{PE} = Z^5 (E_\gamma)^{-7/2}, \quad \text{Equation 3-2}$$

where E_γ is the energy of the photon and Z is the atomic number of the material (Siffert and Coche, 1968a).

The variation of the cross section with energy for this interaction and the other two contributions to the absorption coefficient are shown in Figure 3-3 for Ge and Si. The

Figure shows that as the photon energy increases, the absorption cross section decreases. The Figure shows that photoelectric absorption is the most probable interaction (the interaction that has the largest cross section) for photon energies up to a few hundred keV, at higher energies scattering becomes more probable (Hubbell and Seltzer, 2004). The electrons created by photoelectric absorption contribute to the main photopeak in the X-ray or γ -ray spectrum (See Figure 3-4).

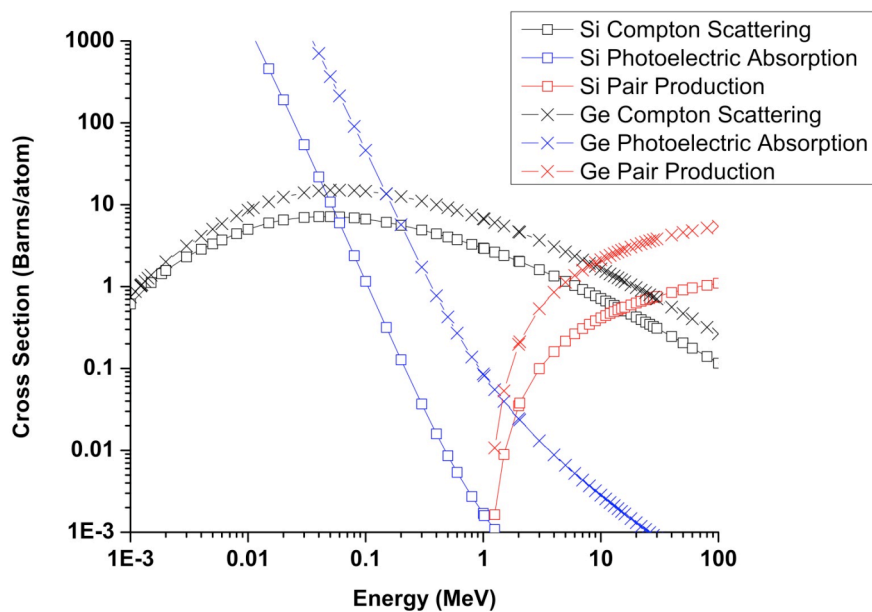


Figure 3-3. The absorption cross-section variation with energy for Si and Ge for photoelectric absorption, Compton scattering and pair production. Data taken from: Hubbell and Seltzer (2004).

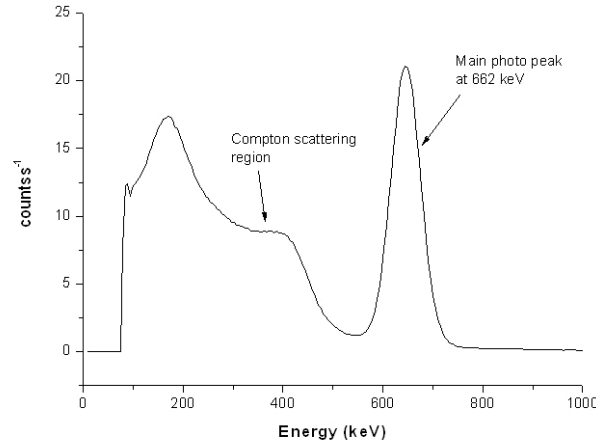


Figure 3-4. A ^{137}Cs spectrum to show the main photopeak and the Compton scattering region.

Compton scattering involves an inelastic collision between a photon and an electron. A photon is re-emitted with a lower energy that may interact with a material again via photoelectric absorption or Compton scatter, or it may escape entirely. This type of scattering can occur at all energies. The photons in this process form the Compton scattering region of the X-ray or γ -ray spectra (See Figure 3-4). Compton scattering is detailed fully in Knoll (1999b) and EG&G Ortec (1984). The cross section for Si and Ge is shown in Figure 3-3; the probability of Compton scattering increases with photon energy up to a critical point (when the photon energy is comparable to the electron rest mass, 0.511 MeV), after which it decreases (Knoll, 1999b).

If the photon has sufficient energy ($E_\gamma > 1.022$ MeV), then it can create an electron-positron pair in the detector (Pair Production). The electron and positron then undergo scattering reactions with the detector material, creating electron-hole pairs until they reach thermal energies (< 1 eV (Révay and Belgya, 2004)). The thermal electron can carry charge as any other electron, but when the positron slows to thermal energies, it annihilates with an

electron to create two 0.511 MeV γ -ray photons. In a detector, these γ -rays have three possible effects (EG&G Ortec, 1984):

- 1 If both γ -rays escape the detector, the total energy absorbed in the detector is 1.022 MeV lower in energy than the initial γ -ray energy, and this forms double escape peak (DE) in the γ -ray spectrum.
- 2 If one γ -ray escapes, the total energy absorbed in the detector is 0.511 MeV lower than the initial γ -ray energy, and this forms a single escape peak (SE).
- 3 If both γ -rays are absorbed, all of the energy associated with the γ -ray has been absorbed, and therefore the detected event contributes to the full photopeak.

Pair production becomes particularly important for γ -rays of energy > 3 MeV, but is possible for γ -rays above 1.022 MeV, as shown in Figure 3-3.

3.4 Semiconductor Detectors

The band level model of a semiconductor is shown in Figure 3-5. Electrons in incomplete outer shells of an atom that can take part in the bonding in the semiconductor crystal lattice (e.g. covalent bonds) are located within the valence band. If sufficient energy is transferred to a valence band electron (e.g. via photon scatter, absorption or thermal excitation), the electron breaks the bond and it 'crosses' the forbidden energy gap, E_g , the minimum energy required for an electron to break the bond holding it within the crystal lattice. The electron is now in the conduction band where it can give rise to a current (See Figure 3-5). Although it is not involved in bonding in the semiconductor, the conduction electron is subject to internal forces in the crystal due to positively charged ions and other electrons. As the

electron breaks from the bond, it leaves a positive charge in the valence band where the bond was broken. The movement of another valence electron into this bond is equivalent to the movement of the positive charge, therefore this broken bond can be thought of as a positive charge carrier, called a hole that can also give rise to a current. A more detailed description can be found in Neaman (2003a).

In an intrinsic semiconductor with no impurities, electrons and holes are created in pairs, i.e. the number of electrons in the conduction band equals the number of holes in the valence band (See Figure 3-5). The width of the E_g is related to the nature of the chemical bonds in the solid, and is temperature and pressure dependent. For example, the compound semiconductor CdTe has an energy gap of 1.45 eV at room temperature and Ge has a gap of 0.665 eV (Restelli, 1968), therefore it is easier to create conduction electrons in Ge than in CdTe.

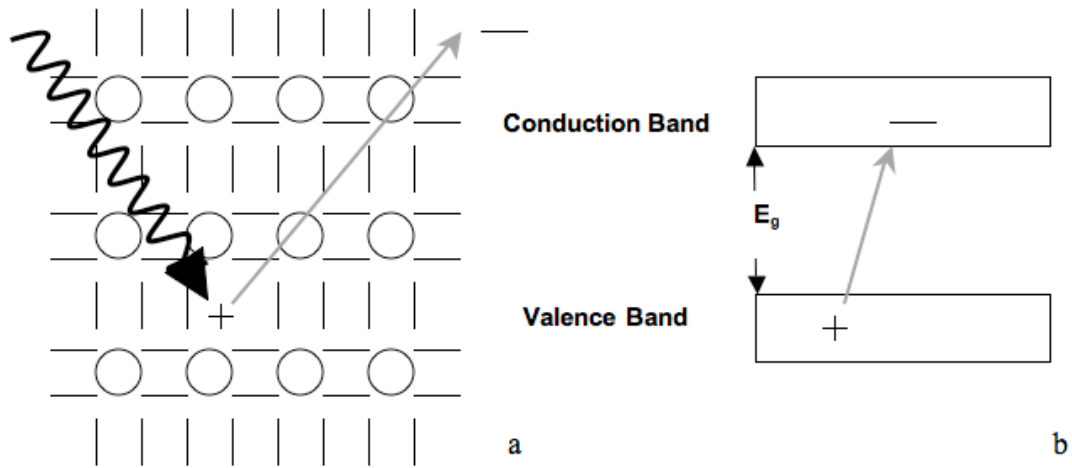


Figure 3-5.a) A representation of incident radiation imparting enough energy to an electron involved in bonding in the crystal lattice to cause the electron to break the bond, leaving a positive charge or 'hole'. b) shows the band model representation; the electron is shown leaving the valence band and entering the conduction band.

3.4.1 Impurities and Defects

Semiconductor materials are prone to chemical impurities and structural defects. Impurities include substitutional or interstitial sites that introduce localised levels into the E_g (See Figure 3-6a). These levels can be ionised, either by giving an electron to the conduction band (known as donor sites or in the case of an impurity, a donor material) or generating a hole in the valence band (known as acceptor sites or an acceptor material). The activation energy of this localised level is substantially smaller than the E_g and can be used to aid the transfer of electrons to and from the conduction band. In some cases semiconductor materials are intentionally doped with an impurity to improve their electrical characteristics. 'Extrinsic' semiconductors are doped to create donor/acceptor levels in the E_g , so that charge generation occurs preferentially from these levels. This means that the

electrons and holes are no longer present in equal concentrations. A semiconductor with an excess of electrons (possibly due to the insertion of a donor material) is known as an n-type semiconductor (Figure 3-6a). A semiconductor with an excess of holes is known as a p-type material (Neaman, 2003b).

If an n-type semiconductor is coupled to a p-type semiconductor, it forms what is known as a p-n junction (See Figure 3-6b). When a reverse bias is applied to the semiconductor, all the conduction electrons flow to the p-side and the holes to the n-side. This leaves a depleted region in the semiconductor where there are only donor and acceptor sites present, the acceptor sites near the p-side and the donor sites at the n-side (See Figure 3-6c). A negative space charge forms near the p-side of the junction and a positive space charge forms near the n-side. This creates an electric field in the depletion region. There is no further conduction until new electron-hole pairs have been formed e.g. by thermal excitation or the interaction of radiation with the detector to create an electron-hole pair (Neaman, 2003c).

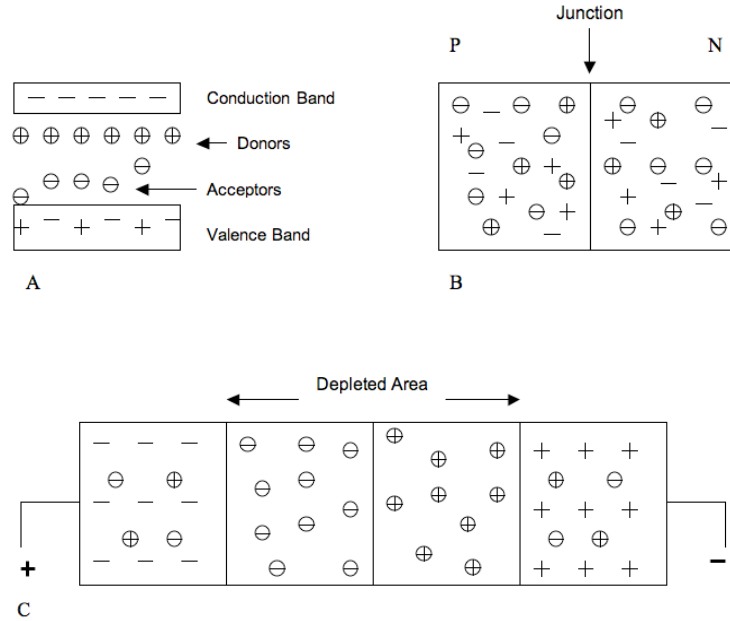


Figure 3-6. a) An n-type semiconductor with an excess of donor sites, b) A p-n junction before the application of an applied voltage, c) after the application of an applied bias voltage, showing the depleted region of the semiconductor.

Structural defects are caused by manufacturing errors or due to damage caused by the interaction of particle radiation with the semiconductor (e.g. proton or neutron radiation). These defects affect the mobility of the charge carriers and the recombination and the trapping in the semiconductor. In the case of Si and Ge, the defects tend to be vacancies in the atomic structure that leave unsaturated bonds on neighbouring atoms that behave as acceptor impurities. The acceptors capture the electrons and give rise to localised levels in the E_g . Interstitial sites act as donors and the electrons on the resulting levels can be excited to the conduction band; this increases the likelihood of thermal excitation which can contribute to the noise in the detector (Neaman, 2003b).

3.4.2 Charge Generation and Transport in Semiconductor Detectors

The number of charge carriers and therefore the total charge generated in a semiconductor detector is proportional to the energy deposited by the photon. The number of charge carriers (N_o) created by an X-ray or γ -ray is given by (Richter and Siffert, 1992):

$$N_o = \frac{E_o}{W}, \quad \text{Equation 3-3}$$

where E_o is the energy of the photon and W is the energy required to create an electron-hole pair.

The energy to create an electron-hole pair is usually 3-4 times the E_g of the semiconductor. The E_g is independent of the photon energy and varies with the temperature of the semiconductor.

The net drift of electrons and holes is random and therefore the net velocity is zero, unless an external force is applied to the semiconductor material (e.g. an electric field). The drift velocity of carriers in a semiconductor material, v , in a planar detector subjected to an electric field is proportional to the electric field strength, κ . The constant of proportionality is the mobility of the carrier μ (Quaranta, 1968). The mobility of a carrier is dependent on the interaction between the lattice atoms and the charge carriers and the impurity concentration of the material, i.e. the amount of trapping that occurs (See Section 3.4.1 and 3.7.2) (Neaman, 2003d). Electrons have a higher mobility than holes, hence a faster drift velocity.

$$v = \mu\kappa, \quad \text{Equation 3-4}$$

The motion of the charge carriers generates a transient current in the detector. The transient current generated by each charge is given by:

$$I = nvq, \quad \text{Equation 3-5}$$

where n is the number of charge carriers and q is the charge of each individual carrier.

The current generated is integrated at the contacts over time to give the induced charge. The charge generated by each carrier of charge q_o moving from the point of generation r to an electrode at $r + dr$ is (Darken and Cox, 1995):

$$dq = q_o \frac{\mathcal{E}(r) dr}{V}, \quad \text{Equation 3-6}$$

where V is the voltage across the contacts (the bias voltage) and $\mathcal{E}(r)$ is the electric field at radius r .

In a planar detector, the induced charge is independent of depth of the interaction in the detector because the electric field is uniform. For a cylindrical detector the electric field (\mathcal{E}_c) at r can be expressed by (Hage-Ali and Siffert, 1995):

$$\mathcal{E}_c(r) = \frac{V}{r \ln(r_2/r_1)}, \quad \text{Equation 3-7}$$

where r_1 is the inner contact radius and r_2 is the outer contact radius.

For a hemispherical configuration the electric field (\mathcal{E}_{hs}) at r is (Hage-Ali and Siffert, 1995):

$$\mathcal{E}_{hs}(r) = \frac{V}{r^2 \left(\frac{1}{r_1} - \frac{1}{r_2} \right)}, \quad \text{Equation 3-8}$$

For both the cylindrical and hemispherical configurations, the electric field is highest near the inner contact, according to Equations 3-7 and 3-8. Figure 3-7 shows the majority carrier

contribution to the charge collection as a function of where the ionising event occurred. It clearly shows that more interactions that take place nearer the outer contact of the cylindrical and hemispherical detectors where the volume is larger. These charge carriers travel through the high field region of the detector, therefore the induced charge is larger.

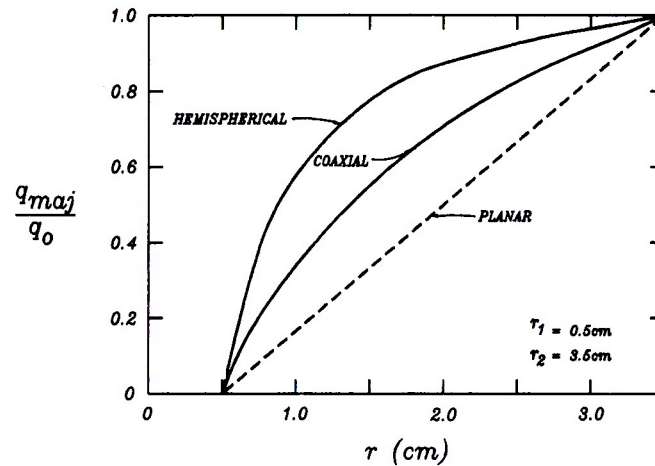


Figure 3-7. The majority carrier collection contribution to the charge collection as a function of where the ionising event occurred. Taken from Hage-Ali and Siffert (1995).

The lifetime of electrons and holes in a semiconductor depends on the rate of recombination in the semiconductor. Direct recombination occurs when an electron leaves the conduction band to rejoin the valence band, as depicted in Figure 3-8. Trapping sites are localised levels in a semiconductor band gap that capture a carrier (See Figure 3-8), but after a time it is released back to its original band rather than causing further recombination (the carriers are usually thermally excited out of the trapping site). The carrier cannot conduct while it is trapped therefore the induced current due to that photon interaction is reduced.

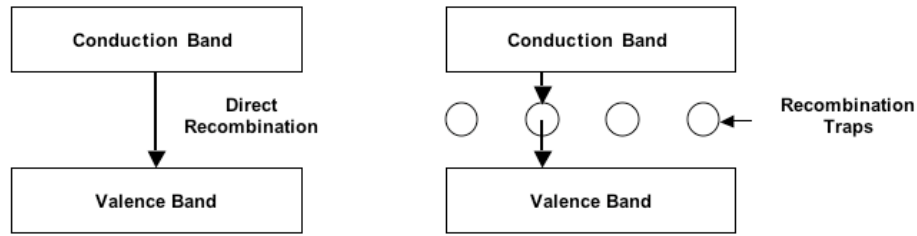


Figure 3-8. Methods of recombination in a semiconductor detector.

The trapping time (or carrier lifetime- the average time a carrier is free before trapping occurs) of the charge carriers is given by τ (Ortec, 2007):

$$\tau = \frac{1}{N_t \sigma_e v_{th}}, \quad \text{Equation 3-9}$$

where N_t is the density of trapping centres, σ_e is the capture cross section of the trap, and v_{th} is the thermal drift velocity of the carrier.

3.4.3 Effect of Temperature on Semiconductor Detectors

The noise in a detector is dependent on the temperature of the detector material and the E_g of the semiconductor. At sufficient temperatures, thermal excitation can produce electron-hole pairs that are swept to the electrodes of the semiconductor in the same way as those created by photon interactions, producing a ‘dark current’ that is processed and contributes to the low energy region of a spectrum. This puts a practical limit on the bias of the system, because an increased bias will increase the charge collection efficiency of both the photon interaction generated carriers and the thermally excited ones. A solution is to cool the detector (e.g. materials with a small E_g such as Ge require cooling to 77K to avoid

high levels of dark current), or to choose a material with a larger E_g (e.g. CdTe has a large band gap (~ 1.45 eV at room temperature (Restelli, 1968)).

The temperature can also affect the mobility of the charge carriers. The density of trapping centres of a material, their trapping, and de-trapping lifetimes contribute to the mobility of a carrier. The de-trapping lifetime is the duration the traps hold the charge before releasing them. The de-trapping lifetime is dependent on the temperature of the material. The de-trapping lifetime (τ_d) can be expressed by the equation (Ortec[®], 2007; Bao et al., 1995):

$$\tau_d = \frac{1}{N_c \sigma_e v_{th} \exp(-E_t/kT)}, \quad \text{Equation 3-10}$$

where N_c is the density of states, E_t is the activation energy of the trap, and T is the absolute temperature of the material, σ_e is the capture cross section of the trap and v_{th} is the thermal drift velocity of the carrier.

Equation 3-10 shows that as the temperature is increased, the trapping time decreases. However, this also implies that there are now more free traps and therefore the trapping rate increases, and the overall carrier mobility decreases and the collection efficiency decreases. Figure 3-9 shows the variation of electron mobility with temperature for CdTe, as the temperature is increased, the electron mobility decreases.

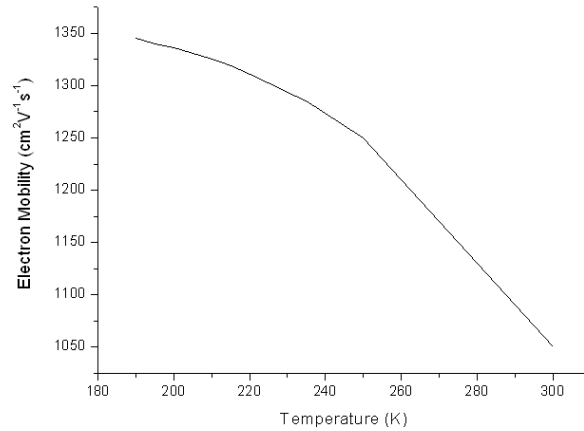


Figure 3-9. Electron mobility in CdTe with temperature from 190 K to 300 K. Data taken from Sellin et al. (2004).

The effects of charge trapping on the performance of a semiconductor detector are detailed in Section 3.7.2.

3.5 Scintillator Detectors

Scintillators are materials that have the property of emitting light when they absorb the energy of interacting radiation. A scintillator-based detector consists of a scintillator crystal or a phosphor, coupled to a photomultiplier tube (PMT) or photodiode. The system produces a current pulse whose height is proportional to the intensity of the light flash generated in the crystal due to the photon interaction.

A photon can give all or part of its energy to a charged particle in a scintillator crystal.

Figure 3-10 demonstrates the processes that result in scintillation photon emission.

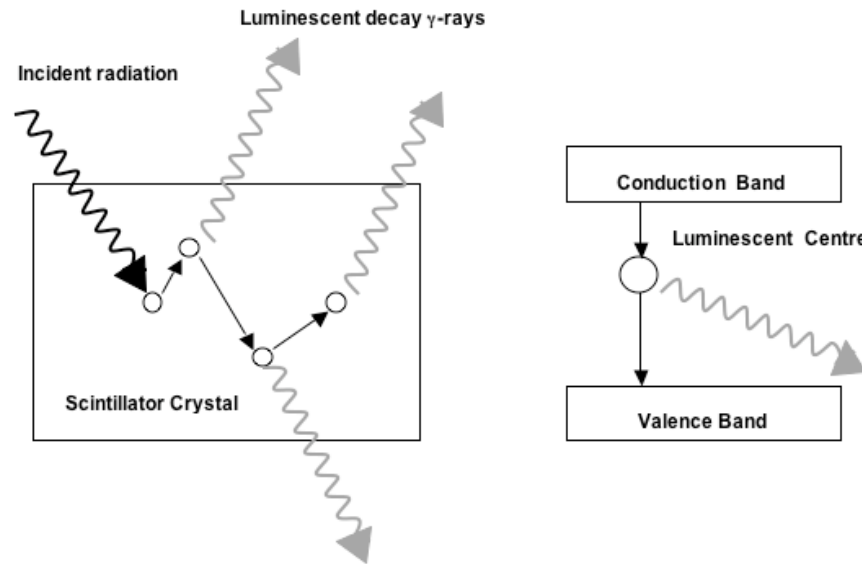


Figure 3-10. A diagram of the interactions that occur in a scintillator detector.

The incident radiation is absorbed/ scattered by an electron in the detector. The electron then dissipates its excess energy via radiative decay and inelastic electron-electron scatter. This creates many electron-hole pairs in the scintillator. When the original electron's energy is less than the ionisation energy threshold, the hot electrons and holes thermalise via intra-band transitions. Luminescent centres in the crystal are excited by the impact of the hot electrons, and they sometimes capture them. The luminescent centres then decay by photon emission to their ground states, which is the characteristic 'flash' a scintillator makes (Knoll, 1999c).

Some scintillation photons are absorbed because the scintillator crystal has an imperfect transparency to the crystal's own fluorescence radiation. The photons that do reach the photocathode in the PMT are converted into photoelectrons (See Figure 3-11). The scintillation photons are converted to photoelectrons via photoelectric absorption at the photocathode (Section 3.3). The PMT accelerates the photoelectrons and are directed to strike a series of electrodes (dynodes) held at potential, which results in secondary electron emission (Knoll, 1999d). The PMT multiplies the few hundred photoelectrons created by each photon into a usable current pulse ($> 10^7$ electrons).

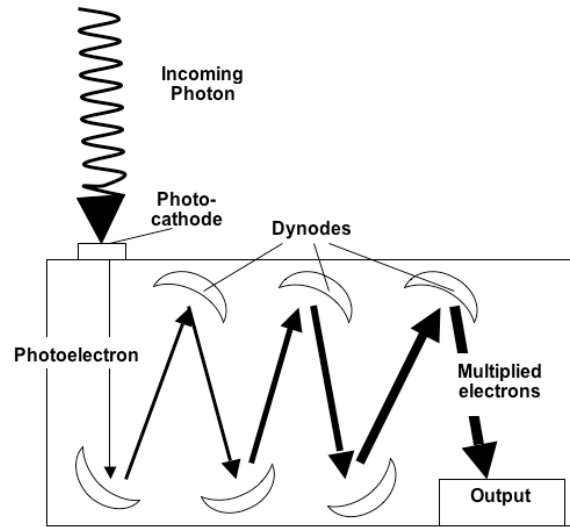


Figure 3-11. A diagram of the processes that occur in the PMT.

The luminescence can be intrinsic to the scintillator e.g. involve electron-hole recombination or be an extrinsic property, e.g. the luminescence ions are doped into the material. Activator ions that cause extrinsic luminescence include Tl^+ , Ce^{3+} and Eu^{2+} (Derenzo, 2003). Scintillators with activator ions can have very high luminosities, e.g. caesium iodide ($CsI(Tl)$) has a very high luminosity. Currently Ce doped scintillators show the best combination of stopping power, speed and luminosity (Derenzo, 2003).

Recent developments have allowed the use of photo detectors or photodiodes instead of PMTs coupled with ultra low noise electronics to eliminate the need for high bias voltages (required by a PMT) and to overcome the poor efficiency associated with PMTs. Instead of converting the emitted light from the scintillator into electrons like the PMT, the photo detector converts the light directly into an electrical signal whose amplitude is directly proportional to the energy of the incoming γ -ray. This has meant that the efficiency of the

detectors and resolution of detectors has increased, to the point where they are now beginning to be competitive with traditional semiconductor detectors. Photo detectors also require lower bias voltages than PMTs (Knoll, 1999d).

3.6 Intrinsic Full-Energy Photopeak Efficiency and Resolution

The intrinsic efficiency of a spectrometer is the ratio of the number of photons detected to the number of photons incident on the detector. The intrinsic full-energy photopeak efficiency is the number of photon counts in the main photopeak compared with the number of full-energy photons incident on the detector. The efficiency of a spectrometer at a particular energy can be calculated if the peak area and calibration source activity are known. Several factors have to be taken into account to get the intrinsic full-energy photopeak detector efficiency so that the detector materials can be compared directly.

Factors including:

- The source to detector distance.
- The self-attenuation of the source.
- Dead time of the detector.
- The thickness of any materials that the γ -rays travel through before they reach the detector (the γ -ray attenuation).
- The detector area and thickness.

These factors can attenuate or alter the energy spectrum of the γ -rays reaching the detector, and can therefore affect the efficiency measurement. Equation 3-11 is the efficiency of the detector modified by these correction factors to give the intrinsic full energy photopeak efficiency of the detector (Molnár et al., 2002; Saint-Gobain Crystals, 2007):

$$\varepsilon_T = \frac{C}{A \times P_\gamma \times f_g \times f_a \times f_d \times f_{sa} \times (T_L / T_R)}, \quad \text{Equation 3-11}$$

where, C is the number of counts in the peak.

A is the activity of the source (Bq).

P_γ is the probability of γ -ray emission at the energy of the peak.

f_g is the geometry correction factor, i.e. the solid angle created by the detector of radius r a distance d away from the source (Saint-Gobain Crystals, 2007).

f_a is the γ -ray attenuation of the source as the γ -rays travel to the detector (Lindstrom and Yonezawa, 2004).

f_d is the fraction of γ -rays that are absorbed in the detector; this is expressed in terms of the linear attenuation coefficient of the detector material, μ (cm^{-1}) and thickness of the detector, x (cm) (Saint-Gobain Crystals, 2007):

$$f_d = \exp(-\mu x), \quad \text{Equation 3-12}$$

f_{sa} is the γ -ray self attenuation factor (Lindstrom and Yonezawa, 2004).

T_L is the detector system live time (s), and T_R is the detector system real-time (s), the ratio of these values corrects for the dead time.

An ideal detector would detect every photon incident on it and would produce a voltage pulse of exactly the same amplitude for every photon i.e. in a spectrum of the number of photons per energy interval all the pulses created due to photons of a given energy interacting with a detector would be in one energy interval (the photopeak). However, in reality some photons do not interact with the detector at all. These photons are scattered out of the detector or induce secondary emission, meaning that they only deposit a portion of their energy in the detector. Even when full energy deposition occurs, the peak can still

have a finite width (which defines the energy resolution of the detector) due to the following effects:

- a) Statistical fluctuations in charge carrier generation and collection in the detector and detector electronics. Equation 3-3 demonstrates that the number of charge carriers created is discrete; therefore there is a random fluctuation in the number of charge carriers that is governed by Poisson statistics (Knoll, 1999e). Under Poisson statistics, the fluctuation of the number of charge carriers N , for a given photon energy is $N^{0.5}$; this has implications on the resolution of the detector. If this were the only source of the peak broadening, the photopeak should have a Gaussian shape (Knoll, 1999e).
- b) Electronic and thermal noise from the detector electronics.
- c) Carrier trapping in the detector which leads to fluctuations in the transient current, causing low energy tailing. Low energy tailing is a result of incomplete charge collection (often due to trapping). The charge is assigned to a lower energy bin than would occur with no trapping, causing tailing of the main photopeak (See Section 3.7.2).
- d) There is also a spread in rise times due to geometric effects of the detector. Charge carriers are generated at varying points of the detector, therefore they can take longer to reach the electrodes than charge carriers created at the surface of the detector due to carrier mobility or trapping effects. This leads to peak broadening and low energy tailing. This puts a practical limit on the size of some detector materials.
- e) Drift in the spectrometer's response function due to changes in temperature etc.

These effects are detailed fully in Knoll (1999f) and Cappellani and Reselli (1968).

The full width half maximum (FWHM) of a photopeak is used as a measure of resolution of a detector at a given energy. The FWHM is a measure of the peak broadening due to the effects listed above. In a spectrum the resolution is given by (Belgys and Révay, 2004):

$$\text{Resolution}(\%) = \frac{FWHM}{\text{Peakenergy}} \times 100, \quad \text{Equation 3-13}$$

3.7 Types of Semiconductor Detectors

3.7.1 Ge and Si Detectors

Ge has a high Z , a large photon absorption cross section, a small E_g , and can be produced with very low impurity and defect concentrations (10^{-5} ppb (Knoll, 1999g) - so the mobilities are high (Table 3-1)), which makes it very suitable for GRS (photons of energy 200 keV- 10 MeV). Si can detect photons of energy as low as 1 keV, and they generate less background than is attributable to high-energy photon scatter and escape peaks, therefore it is more suited to XRF applications (EG&G Ortec, 1995). The properties relevant to spectrometers are shown below for Si and Ge in Table 3-1.

Properties	Si	Ge
Z	14	32
Density (g cm^{-3} at 300K)	2.33	5.33
Carrier density (cm^{-3} at 300K)	1.5×10^{10}	2.4×10^{13}
Electron mobility ($\text{cm}^2 \text{V}^{-1} \text{s}^{-1}$) at 77 K	1350	42000
Hole mobility ($\text{cm}^2 \text{V}^{-1} \text{s}^{-1}$) at 77 K	480	45000
Energy to create an electron-hole pair at 77K (eV)	3.76	2.96

Table 3-1. The properties of Si and Ge. (Restelli, 1968, Darken and Cox, 1995).

Large volume high-purity Germanium (HPGe) detectors are used in fundamental physics research, and in nuclear power facilities because of their excellent spectral resolution. A co-axial configuration of detector is often used with its axis pointed towards the γ -ray source. The GEM-15200-P Poptop HPGe detector detailed in Chapter 4 is a p-type semiconductor material in a closed-end co-axial geometry (See Figure 3-12) that is positively biased at 3.5 kV (EG& G Ortec, 1995). The outer contact (500-1000 μm) is Li diffused (EG& G Ortec, 1995) to form a p-n junction (See Section 3.4) on the outer surface; the inner contact (0.3 μm) is ion implanted. The excess n-type region (n^+) at the outer surface and the excess p-type region (p^+) on the inner surface prevent the injection of large numbers of holes and electrons from their respective regions (EG& G Ortec, 1995). A bias is applied to the detector (See Figure 3-12) that depletes the p-region so no current flows except for leakage currents and the current generated by photon interactions (Gehrels et al., 1988). Most γ -ray interactions occur near the outer contact.

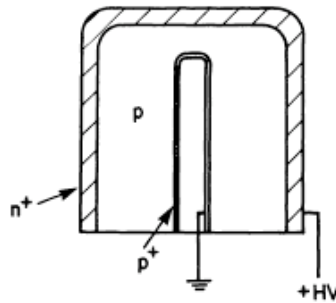


Figure 3-12. A diagram of the co-axial detector, the thick outer contact is lithium diffused and forms a p-n junction. Taken from Gehrels et al. (1988).

3.7.2 CdTe Detectors

CdTe is one of many compound semiconductors used in spectroscopy applications. The advantages of using a CdTe detector over an HPGe or Si detector are that:

- It has low noise at low energies, giving it good resolution at low energy.
- It has a large band gap (~ 1.45 eV at room temperature (Restelli, 1968)).
- It can operate at room temperature (unlike Ge detectors that have to be cooled to 77 K). Operation at room temperature allows them to be portable.

However, CdTe cannot yet be manufactured with the same purity levels as HPGe or Si; which affects the performance of the detector material. The resolution and efficiency of CdTe detectors is limited due to charge trapping created by impurities and defects in the detector crystal. The defects and impurities create trapping sites with specific trap and release times (Equations 3-9 and 3-10) (Redus, 2003). The charge trapping causes a redistribution of the energy associated with a specific detected event which results in low energy tailing of the photopeak of the spectrum (i.e. the resolution degrades). For interactions occurring deeper in the semiconductor material, the charge carriers (particularly the holes because they have lower mobilities) are subject to greater trapping and recombination losses. This puts a practical limit on the size of CdTe detectors that is limited by the purity of the CdTe crystals.

The density of trapping centres of a material and their trapping lifetimes determine the mobility of a carrier. High purity Si or HPGe crystals have large carrier lifetimes, τ_e , (for HPGe $\tau_e = 10^{-3}$ seconds), i.e. the trapping density is small so negligible trapping occurs.

Compound semiconductors have smaller carrier lifetimes (for CdTe $\tau_e=10^{-6}$ seconds) (Redus, 2003) because:

- They are not yet made to the purity levels of Si and HPGe (CdTe impurity concentration was reported to be \sim ppm (Oda, 2007) and the HPGe impurity concentration is $\sim 10^{-5}$ ppb (Knoll, 1999g)).
- Any deviation from stoichiometry in compound semiconductors will generate defects.
- In CdTe, precipitates of Te exceeding 1 μm generate noticeable scattering in the charge collection (Simon, 2009).

The corresponding lower mobility of the holes leads to a longer collection time; this increases the probability of trapping losses.

Until the purity of CdTe can match that of HPGe and Si, there have been several proposed solutions to the problem of charge trapping in semiconductors. Higher bias voltages are not always possible because the velocity of the charge carriers can saturate due to the mobility of the carriers (Section 3.4.2). Several other methods have been developed to compensate for low hole mobility in CdTe detectors that are detailed below.

3.7.2.1 Pulse Shape or Rise Time Discrimination

This method is carried out electronically by examining the pulse shape from the detector preamplifier. The pulse shape from the detector can distinguish its origin (radiation, charged particles, background or noise). Any pulses with a rise time differing to that desired are removed e.g. pulses that could contribute to a low energy tail. This improves the

resolution but reduces the sensitivity since it effectively rejects counts. Rise time discrimination is covered in detail in Knoll (1999a).

3.7.2.2 Stacked Detectors

A thin CdTe detector has the advantage that it reduces the amount of trapping that occurs in the material and overcomes the charge loss that would occur in a thicker detector of the same hole mobility and hole lifetime. However, the disadvantage is that the detection efficiency is not sufficient for γ -rays above several hundred keV that have longer interaction lengths. The solution for the detection of high-energy γ -rays is to stack several thin CdTe detectors together so that they act as a single, thicker detector. Stacking thin detectors with smaller trapping lengths will maintain the large sensitive volume while reducing the low energy tailing. Watanabe et al. (2002) describe a stacked CdTe detector.

3.7.2.3 Compact Pulse Processor

A compact pulse processor (CPP) is a charge loss compensation unit designed to improve the energy resolution and photopeak efficiency of planar CdTe detectors by combining a normal spectroscopy amplifier with an electronic pulse-processing unit. In planar CdTe, the hole mobility limits the charge collection. Richter and Siffert (1992) reported that the fractional energy loss due to trapping correlates with the charge collection time. The correlation is a constant property of the detector and is independent of the photon's energy. It was possible to electronically correct each pulse by the charge lost based on the pulse rise time, thus moving the detected event into the main photopeak; this is the function of the CPP (EURORAD, 1998a).

3.7.2.4 Single Carrier Collection

The geometry or the electrical field shape of the detector can be altered so that only one type of charge carrier is collected. Electrons are usually chosen because in CdTe they have a mobility 10 times that of the holes. Malm et al. (1975) carried out a study to investigate the effect of changing the detector configuration from planar to hemispherical on the pulse height spectra. They came to the conclusion that a hemispherical single charge carrier collection detector with a positive central electrode (See Figure 3-13) would provide the best performance out of the three configurations, planar, hemispherical with a positive central contact and hemispherical with a negative central contact. This configuration uses electrons as the charge carrier. Development on large volume detectors in this configuration is continuing (Simon, 2008). Hemispherical and planar CdTe detectors were characterised as part of this work (See Chapter 4).

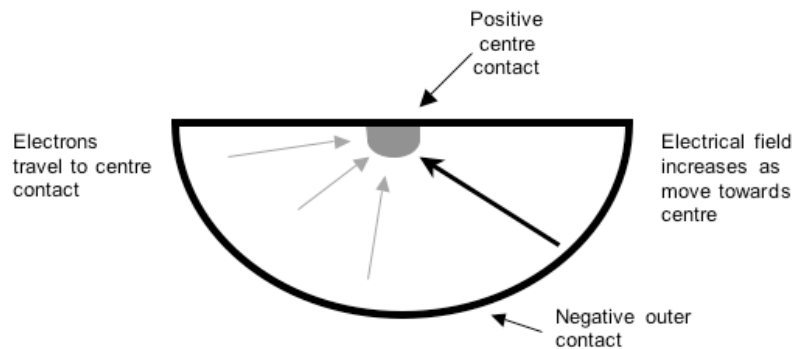


Figure 3-13. The hemispherical detector configuration.

3.7.3 Types of Scintillator Detectors

Several scintillators are detailed in Table 3-2. Lanthanum bromide crystals doped with Ce ($\text{LaBr}_3(\text{Ce})$) are a new generation of inorganic rare earth doped halide scintillators that have high light output ($\sim 60,000$ photons/MeV), high stopping efficiencies, fast response times, are of low cost and have good linearity. They have energy resolutions as low as 4 % at 662 keV at room temperature. This resolution makes this scintillator comparable in performance to compound semiconductors. This detector and a CsI(Tl) detector were characterised by the University of Leicester together with several semiconductor detectors (See Chapter 4).

Detector	Sodium Iodide NaI(Tl)	Cs Iodide CsI(Tl)	Lanthanum Bromide $\text{LaBr}_3(\text{Ce})$	Lutetium Iodide $\text{LuI}_3(\text{Ce})$
Density (g cm^{-3})	3.67	4.51	5.29	5.60
Atomic numbers	Na= 11 I =53	Cs= 55 I = 53	La = 57 Br = 35	Lu = 71 I = 53
Photon efficiency (/MeV)	38,000	40,000	63,000	50,000
Maximum emission wavelength (nm)	415	550	380	474
Energy resolution at 662 keV (%)	12.5	~ 8	< 4	~ 11
Decay time (ns)	230	900	16	23

Table 3-2. A comparison of some properties of several scintillator materials (Shah et al. 2002a, Shah et al., 2002b, Adams, 1970, EURORAD, 2008, EURORAD 1998b, Lecoq et al., 2006).

3.8 Examples of γ -ray Spectrometers on Previous Spacecraft

Since the Ranger missions to the Moon in the 1960s, many planetary science missions have utilised GRS to determine the composition of a planetary surface, a number of these are detailed below for missions to the Moon, Mars and Venus.

Mission	Year of first operation	Type of detector	Energy range (MeV)	Resolution (%)
Luna 10 and 12	1966, 1967	Scintillator	0.3 - 7 MeV	~ 8%
Apollo 15 and 16	1971, 1972	NaI(Tl)	0.55 - 8.6 MeV	8% at 662 keV
Venera 8, 9 and 10	1972, 1975, 1975	NaI(Tl)	0.3 – 3MeV	11% at 662 keV
Vega 1 and 2	1985	CsI(Tl)	0.3 – 3 MeV	10% at 662 keV
Lunar Prospector	1998	BGO	0.3 - 9	10.5% at 662 keV
NEAR	2000	NaI(Tl)	0.1 -10	8.7% at 662 keV
2001 Mars Odyssey	2001	HPGe	0.1 -10	~0.3 at 662 keV

Table 3-3. The details of the γ -ray spectrometers used on a number of interplanetary missions (Surkov, 1997b; Boynton et al., 2004; Goldsten, 1998; Adler et al., 1973; Bruckner and Masarik, 1997; Feldman et al., 2004). BGO= Bismuth Germanate; NaI(Tl)= Sodium Iodide.

The Lunar Prospector mission to the Moon was operational from 1998 to 1999, and was designed to study the lunar surface and its composition from orbit. The γ -ray spectrometer on Lunar Prospector was composed of a \varnothing 7.1 cm x 7.6 cm long cylinder of BGO that was capable of detecting γ -rays ranging in energy between 0.5 MeV and 9 MeV (Feldman et al., 2004). Surrounding the detector was a borated plastic scintillator anticoincidence shield that rejected the cosmic ray background and charged particle interactions within the detector. A full description can be found in Feldman et al. (2004).

2001 Mars Odyssey entered Mars orbit in October 2001 and has been operational from February 2002 to date. The γ -ray spectrometer suite was designed to determine the composition of the near-surface of Mars from orbit by measuring the γ -ray and neutron emissions from the Martian surface. The instrument suite included the γ -ray spectrometer, which was designed to measure the γ -rays emitted from Mars; the neutron spectrometer (NS), which was designed to monitor epithermal and thermal neutron emissions; the high-energy neutron detector (HEND), which was designed to monitor fast and epithermal neutrons detectable from orbit and the central electronics box (Boynton et al., 2004). The γ -ray spectrometer consists of a \varnothing 6.7 cm x 6.7 cm, n-type, HPGe crystal enclosed in a titanium structure. It is separated from the spacecraft by a 6 m boom to minimise the contribution of the background from the spacecraft (Boynton et al., 2004).

3.9 Summary

The materials that commonly comprise XRF and GRS detectors have been discussed, and how their properties are exploited to carry out the two techniques. Examples of detectors used on previous interplanetary remote sensing missions were described, including a scintillator detector based mission (Lunar Prospector) and a semiconductor detector based mission (2001 Mars Odyssey). Chapter 4 details an experimental campaign to characterise and compare several types of detector to determine which variety will meet the requirements of an in-situ probe or lander mission.

Chapter 4

Characterisation and Selection of γ -ray Detectors for a Geophysical Package

4.1 Introduction

This chapter describes the evaluation and comparison of different γ -ray detector solutions and configurations including: planar and hemispherical cadmium telluride, a caesium iodide scintillator, a lanthanum bromide scintillator and a high-purity germanium detector. A discussion then follows on the trade-offs that are made between detector performance and suitability for a mission, including factors such as radiation tolerance, power requirements and mass restrictions. A recommendation is then made on the most suitable detector for the geophysical package.

4.2 γ -ray Detectors for the Geophysical Package

HPGe has a superior resolution compared with other semiconductor and scintillator detectors. Although work is continuing to miniaturise the equipment required to cool HPGe detectors, the mass, volume and power consumption of the current cooling systems still make HPGe impractical for an in-situ mission where the mass per instrument is limited (A study carried out by Ambrosi et al. (2005) found that HPGe detector systems including the cooling system can have masses as low as 2.5 kg; however, a CdTe detector system could

have a mass as low as 1 kg). Detectors that do not have such stringent cooling requirements such as CdTe and scintillators are more desirable for in-situ missions.

Chapter 1 described the evolution of the concept of the geophysical package from a two-detector system designed to carry out bulk density measurements to an instrument that could also carry out GRS and radiometric dating. The geophysical package could operate as part of an in-situ lander or a sub-surface probe. The possible configuration of an instrumented mole designed to measure planetary heat flow was discussed by Ambrosi et al. (2006) and was shown schematically in Figure 1-1. Recent developments in scintillator materials have produced detectors with resolutions comparable to CdTe with the added advantage that they do not require cooling and have increased radiation tolerance (Owens et al., 2007a). Several detector materials and configurations were tested and compared by M. Skidmore in order to determine which detector material is best suited for a sub-surface probe or for space applications in general. The detectors included:

- a) A 5 mm x 5 mm x 3 mm EURORAD planar CdTe detector coupled to a CPP (EURORAD, 1998a).
- b) A 500 mm³ EURORAD hemispherical CdTe detector (EURORAD, 2006).
- c) A 15 mm x 15 mm x 15 mm EURORAD SC1515 CsI(Tl) scintillator (EURORAD, 1998b).
- d) A \varnothing 25.4 mm x 25.4 mm Saint-Gobain LaBr₃(Ce) scintillator, coupled to a Photonis XP2060 PMT (EURORAD, 2008).

The detectors were compared with a large volume Ortec[®] GEM-15200-P HPGe detector. Detectors a-d were chosen for their suitability to fit within the HP³ mole (see Figure 1-1). Stacked planar CdTe detectors or multiple hemispherical CdTe detectors could be used to

provide a larger interaction volume while still fitting into the available volume within the mole. The $\text{LaBr}_3(\text{Ce})$ and $\text{CsI}(\text{Tl})$ detectors are the largest commercially available scintillators that fit within the available volume in the mole.

An ideal γ -ray spectrometer that could be used for a remote sensing mission would have:

- A high efficiency (maximising the number of detected γ -ray photons contributing to the full energy peak). A high intrinsic efficiency can be achieved using a detector material that has a high atomic number and density. For example, a BGO scintillator (used in the Lunar Prospector and NEAR missions) has a higher Z and density (ρ) (Z of Bi= 83 ρ = 7.13 g cm⁻³ (Knoll, 1999c)) than an HPGe detector (Z = 32, ρ = 5.3 g cm⁻³) (Knoll, 1999g). A larger detector will increase the overall efficiency of the detector at higher energies.
- High-energy resolution, so that peaks that are close together in energy can be separated and identified above the background. For example, HPGe detectors (used in the 2001 Mars Odyssey mission) have a high resolution; $\sim 0.3\%$ at 0.662 MeV, whereas BGO scintillators have resolutions larger than 8% at 0.662 MeV (Boynton et al., 2004), therefore elemental peaks can be more easily distinguished or identified using HPGe.

GRS missions often have a trade-off, sacrificing resolution for efficiency. The detectors listed above were characterised in terms of their resolutions and efficiencies (See Chapter 3, Section 3.6).

4.3 Experimental Methodology

The detectors that were characterised, their sizes, volumes, densities and any operating temperature requirements are shown in Table 4-1. In this investigation the detectors were connected to an Ortec[®] 570 spectroscopy amplifier, coupled to an Ortec[®] Maestro-32 MCA emulator (Version 6.06) installed on a PC. The bias was supplied by an Ortec[®] 459 high-voltage (HV) supply. A CPP was required for the EURORAD planar CdTe detector to correct for the charge losses in the detector due to trapping effects (Section 3.7.2). The same detector electronics would ensure that the contribution of the electronics to the efficiency and resolution of the spectrometer was the same for all the detector materials; only the detector material/ configuration was evaluated. The detectors were connected to the power/ bias supply and the amplifier, then placed in a lead cave (to minimise the background) above the relevant source (See Figure 4-1). The shaping time and gain of the amplifier were varied to find the optimum settings. These settings are shown in Table 4-1.

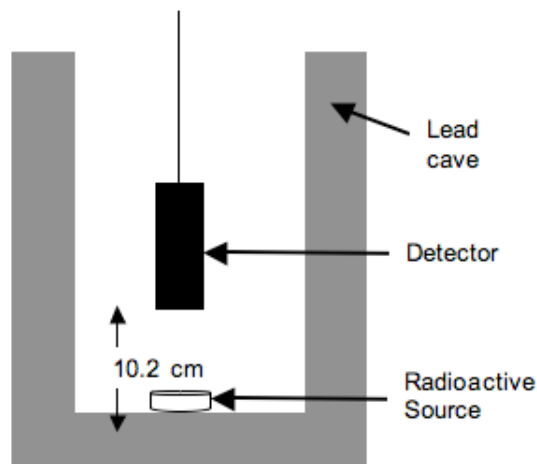


Figure 4-1. Experimental set up of the detectors; the standards were placed at the bottom of the lead cave.

Property	HPGe	CsI(Tl)	LaBr ₃ (Ce)	Planar CdTe	Hemispherical CdTe
Dimensions (mm)	\varnothing 47.9 x 50.4	15 x 15 x 15	\varnothing 25.4 x 25.4	5 x 5 x 3	\varnothing 8.6
Volume (mm ³)	90822	3375	12870	75	500
Density (g cm ⁻³)	5.3	4.41	5.29	6.2	6.2
Operating Temperature (K)	77	293	293	293	223 – 300
Bias (kV)	+ 3.5	N/A	+ 0.488	N/A CPP	+ 1
Optimal Shaping time (μ s)	6	2	1	N/A CPP	1
Optimal gain (x)	10	35.5	35	250	10

Table 4-1. The properties of each detector characterised at the University of Leicester, their operating temperatures and optimised amplifier settings (EURORAD, 1998a, 1998b, 2006, 2008; EG&G Ortec, 1995). The planar CdTe detector was controlled by the CPP unit; therefore the bias and optimal shaping time is not applicable in this case.

In the case of the hemispherical CdTe detector that underwent cooling in a vacuum chamber (See Figure 4-2), the same geometry between source and detector could not be obtained. A thin (0.7 mm) Al window in the chamber wall, 46.5 mm away from the detector allowed the γ -rays to penetrate through to the detector. The detector performance was initially optimised at room temperature; the detector was subsequently cooled and tested at a variety of temperatures down to -50 °C. The resolution and efficiency reached optimum values at a temperature of -30°C.

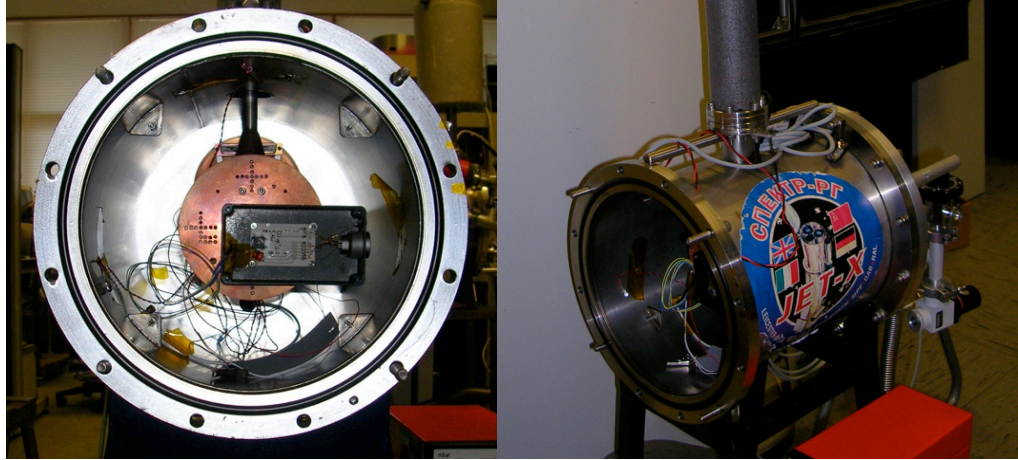


Figure 4-2. The vacuum chamber containing the hemispherical CdTe detector.

The left-hand picture shows the hemispherical detector in the vacuum chamber and the right hand picture shows the outside of the chamber. The source had to be positioned outside of the chamber. The walls of the chamber prevented the same source to detector distance as the other detectors.

4.3.1 Calibration Standards

The detector shaping time, threshold and gain were optimised using a ^{137}Cs source (See Table 4-1). Four additional radioactive standards, (^{232}Th , ^{238}U , ^{40}K and ^{60}Co) were used to collect calibration spectra. The main peaks of each standard are listed in Table 4-2. In addition to these standards, additional data from a number of other standards (^{88}Y , ^{22}Na , ^{54}Mn , ^{57}Co) was obtained for the HPGe detector in a slightly different geometry in a shielded room as opposed to a lead cave (See Chapter 5).

The spectra were collected (at 20°C or below in the case of the hemispherical CdTe detector) over enough time to obtain reasonable counting statistics i.e. a clear photopeak, at the energies given in Table 4-2, which contained at least 100 counts for the weaker sources. Background spectra were also collected at these settings, and these were subtracted from

each of the source spectra, leaving only the γ -rays collected from the source. The spectra were imported into Origin™ and the FWHM and peak areas of the peaks were calculated for each spectrum. The resolutions and efficiencies of each detector were then calculated using this data. In some cases the peaks of interest could not be resolved from other peaks in the spectrum; therefore they could not be used to calculate the resolution and efficiencies of the detectors.

Source	Peak energy of interest (MeV)
^{232}Th	0.238
^{232}Th	0.510
^{232}Th	0.583
^{137}Cs	0.662
^{232}Th	0.911
^{60}Co	1.173
^{60}Co	1.332
^{40}K	1.460
^{238}U	1.760
^{232}Th	2.614

Table 4-2. Table to show the energy of the main peaks of each calibration standard. ^{232}Th has many daughter products, therefore the number of γ -rays emitted from that standard is high, however the ones listed are the only ones that don't appear to overlap with other γ -rays in the ^{232}Th spectra.

4.4 Results

4.4.1 Resolution

Figure 4-3 displays the ^{137}Cs spectra recorded with each of the detectors. The resolution of each detector is what would be expected; planar CdTe detectors typically have resolutions of $\sim 3\%$, hemispherical CdTe detectors $\sim 4-5\%$, HPGe detectors

$\sim 0.3\%$, $\text{LaBr}_3(\text{Ce}) \sim 3.3\%$ and $\text{CsI}(\text{Tl}) \sim 8\text{-}10\%$ (Boynton et al., 2004; Eurorad, 2008, 2006, 1998a, 1998b). The Figure indicates that the $\text{CsI}(\text{Tl})$ detector has the highest counting efficiency (due to the high count rate in the spectra). The Figure also demonstrates that the resolution of the CsI detector is poorer than that of the other detectors ($\sim 10\%$ at 0.662 MeV) and the best resolution is achieved with the HPGe detector ($\sim 0.3\%$ at 0.662 MeV). There are a number of reasons why scintillator-based detectors tend to have poor resolution compared with semiconductors:

- a) The PMT contributes to the fluctuation in the number of electrons detected adding to the statistics associated with the creation of electron-hole pairs in the scintillator crystal. This contribution is the result of photoelectron generation at the photocathode and the electron multiplication process in the PMT. These statistical fluctuations are the dominant factors in determining the resolution.
- b) In general a higher energy is needed to create an electron-hole pair in a scintillator than a semiconductor because they have larger band gaps (e.g. the E_g of $\text{LaBr}_3(\text{Ce})$ is $\sim 6\text{ eV}$ (Dorenbos, 2002) and the E_g of HPGe is $\sim 0.665\text{ eV}$ (See Chapter 3)).
- c) The luminescent centre decay rate can also vary, leading to a fluctuation in the arrival times of the photons at the photocathode, degrading the resolution in the same way traps would in a semiconductor (this fluctuation is not significant compared to the PMT statistical fluctuation (Knoll, 1999h)).
- d) The scintillator crystal may not be 100% transparent to its own light; so fewer photons reach the photocathode of the PMT.
- e) Light is able to escape from the crystal, reducing the number of electrons created at the photocathode. Coating the crystal in a reflective material can reduce this effect.

The $\text{LaBr}_3(\text{Ce})$ and $\text{CsI}(\text{Tl})$ detectors were coated with a reflective material, therefore this effect was reduced (Stynfeld et al., 2006).

The resolution of the $\text{LaBr}_3(\text{Ce})$ detector is better than the $\text{CsI}(\text{Tl})$ based one because the scintillator material has a shorter decay time (~ 16 ns) than $\text{CsI}(\text{Tl})$ (~ 900 ns) and it has a higher photon yield (60,000 photons MeV^{-1} compared with the $\text{CsI}(\text{Tl})$ 40,000 photons MeV^{-1} (EURORAD, 1998; EURORAD, 2008)). These factors improve the counting statistics and the resolution.

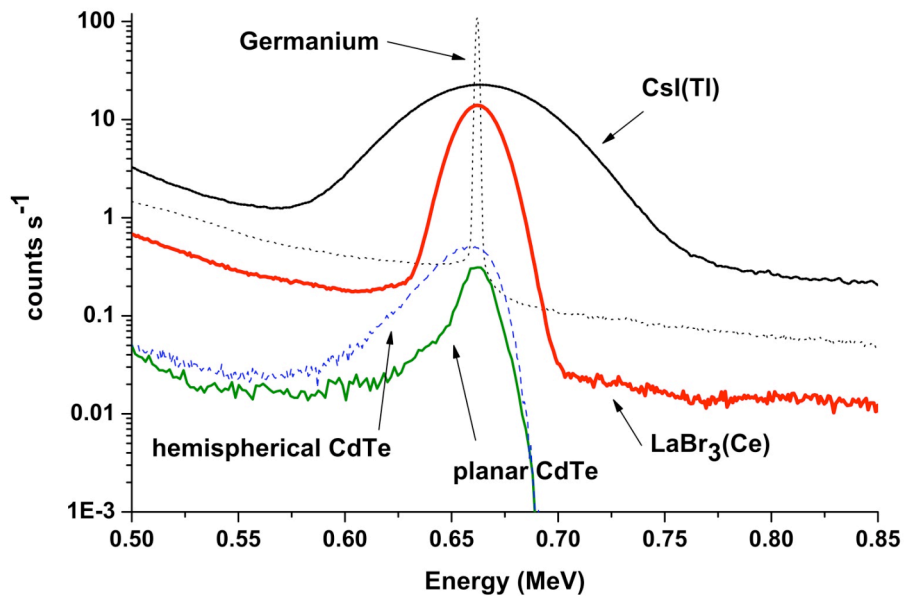


Figure 4-3. ^{137}Cs spectrum for the five evaluated detectors showing the 0.662 MeV peak.

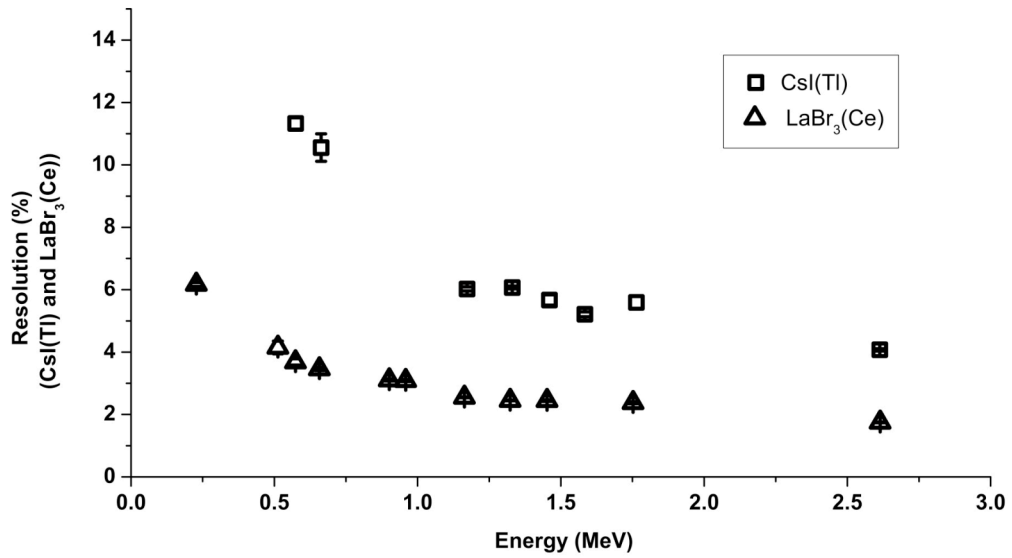


Figure 4-4. Resolution with varying energy for the evaluated scintillator detectors.

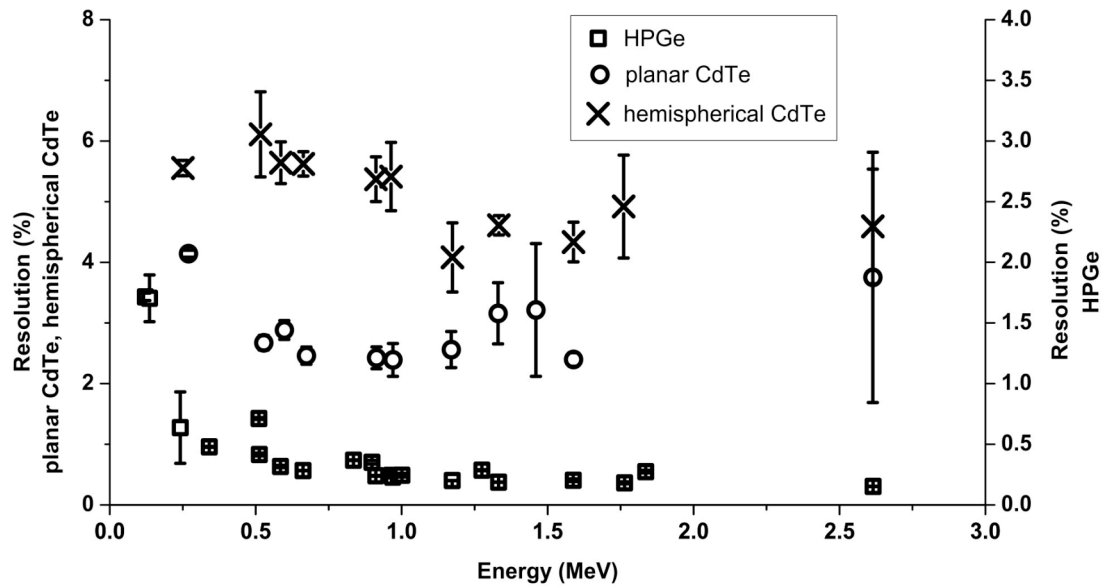


Figure 4-5. Resolution with varying energy for the evaluated semiconductor detectors.

The additional data points for the HPGe detector are from ^{22}Na (0.511 MeV and 1.275 MeV), ^{88}Y (1.836 MeV), ^{54}Mn (0.835 MeV) and ^{57}Co (0.122 MeV and 0.136 MeV).

Figure 4-4 and Figure 4-5 show the resolution of each of the detectors as a function of energy. Although the planar CdTe detector has a resolution of $\sim 2.4\%$ at 0.662 MeV, its performance at higher energies ($\sim 3.8\%$ at 2.614 MeV) is poor compared with LaBr₃(Ce) and HPGe ($\sim 1.7\%$ and $\sim 0.15\%$ at 2.614 MeV respectively). The depth of interactions is important in determining the resolution of the detector. The planar CdTe detector is only 3 mm thick, which makes charge collection more efficient especially if the interaction point is close to an electrode (Hitomi, 2008). In addition, the CPP also reduces the low-energy tailing by compensating for any charge loss effects due to trapping. The thickness of this detector also means that detection efficiency at high energies is particularly low. Many γ -rays interacting with the detector escape, depositing only fractional amounts of energy in the case of incoherent scattering events; high energy γ -rays may not interact with the detector at all. Statistically speaking low efficiencies result in reduced resolution as the number of detected events decrease (See Chapter 3, Section 3.4). Although the efficiency of the planar detector could be increased by increasing the total thickness there is the trade-off between increased efficiency and degradation of resolution as a result of increased trapping by defects in the larger crystal. A solution to this problem is to use a different geometry (such as a hemispherical geometry) for the detector in order to maximise collection efficiency in a thicker detector without significantly affecting the resolution or to stack the planar detectors to create a larger detector volume.

Figure 4-4 and Figure 4-5 show the resolution is poor for all of the detectors at low energies. At low energies the resolution is dominated by the statistical fluctuation in the number of charge carriers (See Chapter 3, Section 3.4). At high energies this effect is less

significant because more charge carriers are generated. The fraction of electrons that are trapped in a semiconductor material due to defects is constant with γ -ray energy. Although this effect is negligible compared to the statistical fluctuation for low energy γ -ray interactions, at higher energies electron trapping becomes the dominant effect on the resolution (this can be seen in Figure 4-4 where the resolution levels off at higher energies). As the γ -ray energy continues to increase, fewer interactions occur in the detector (this is dependent on the volume of the detector), the resolution now becomes dependent on the number of detected events (the efficiency of the detector- longer accumulation times can compensate for this). In sources that emit γ -rays of varying energies such as the ^{232}Th source (See Table 4-2), higher energy γ -rays such as the 2.614 MeV γ -ray are more likely to undergo Compton scattering and pair production in the detector. Fractional amounts of energy deposited via incoherent scattering and pair production can generate additional peaks which can interfere with peaks of interest and reduce the overall signal to background ratio. Escape peaks can also interfere with primary peaks of interest.

Sections 3.4 and 3.7.2 detailed the problems of trapping in semiconductor detectors. In large volume detectors the charge carriers have further to travel to reach the electrodes, increasing the probability of charge trapping, and creating a broader peak. In HPGe the resolution does not change significantly with energy at higher energies because the trapping centre density is small. The hemispherical detector had a poorer resolution than its planar counterpart at lower energies, suggesting that the CPP may be a superior method to improve the resolution compared with single carrier collection to reduce charge trapping at low energies.

4.4.2 Intrinsic Full-Energy Photopeak Efficiency

A plot of the full-energy photopeak efficiency versus energy for each detector material, demonstrates that the $\text{LaBr}_3(\text{Ce})$ detector performs better than the other detectors (Figure 4-6). The planar CdTe detector produced the worst results, even though CdTe has the highest density (See Table 4-1), primarily because of the high trapping probability of the material. The CPP reduced the charge loss effects to improve the resolution, but it was at the expense of the efficiency. Stacking the detectors could improve efficiency and get a large interaction volume while reducing the effects of trapping.

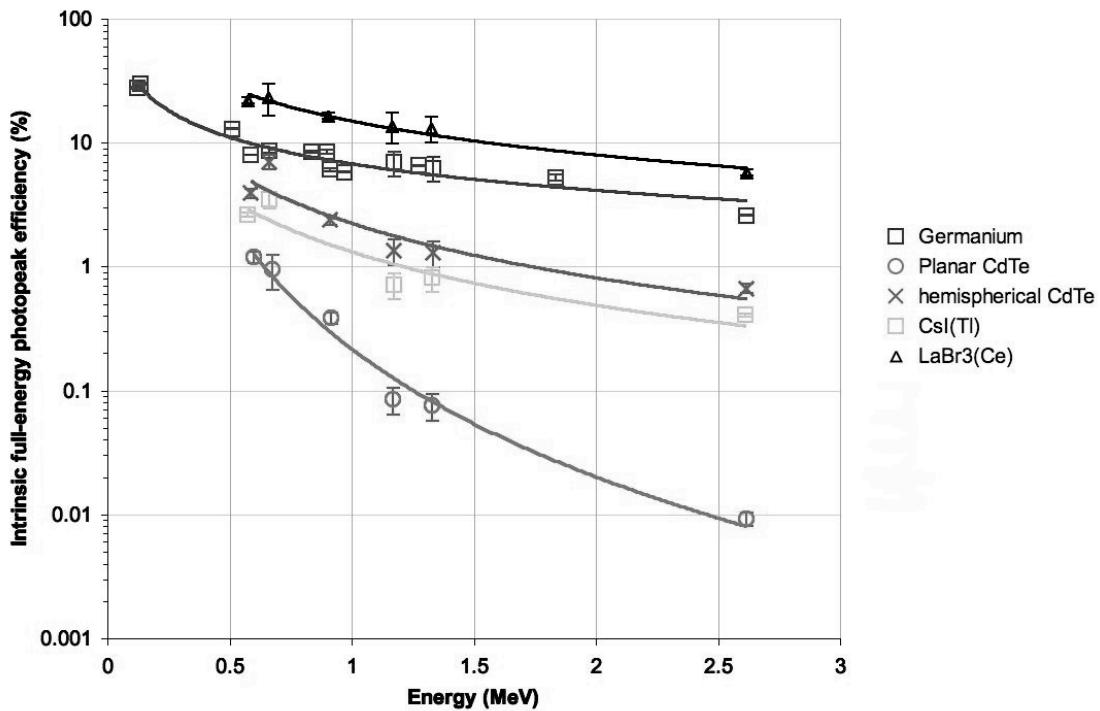


Figure 4-6. Photopeak efficiencies with energy for the five detectors.

Given that the γ -ray interaction probability increases with density and atomic number, high-density detectors that contain high Z materials are preferred. Table 4-1 gives the densities and atomic numbers of each of the detectors. The CsI(Tl) detector efficiency is

lower than that of the other detectors because as seen in Table 4-1 its density is lower than the others. $\text{LaBr}_3(\text{Ce})$ has a higher atomic number than HPGe, therefore the probability of an interaction is higher, and the efficiency is greater.

4.5 Discussion

When selecting the ideal detector for a planetary science mission there are a number of trade-offs that one needs to make and these are often driven primarily by scientific objectives and practical engineering solutions imposed by the mission profile. There are a number of in-situ missions being planned for the near future, including the UK MoonLITE penetrator mission (Gao et al., 2007) and ESA's asteroid sample return mission Marco Polo where the science objectives can be met by an X-ray spectrometer, a γ -ray spectrometer or both instruments. Typically, science objectives for a γ -ray probe on a planetary lander include:

- Determining the concentration of major rock-forming elements on a planetary surface.
- The determination of the concentration of elements that are considered essential for life such as C, N and P.
- Determining the concentration of trace elements on a planetary surface, in particular low Z elements that cannot be detected using XRF.
- Measuring the H content of a planetary surface as evidence for the presence of water/ice.
- Determining the concentration of radioactive elements on the surface.

In order to achieve these science objectives a trade-off study is usually required in efficiency, effective area and resolution versus engineering constraints imposed by the mission, including: radiation tolerance, thermal requirements, mass, power and volume budgets. Table 4-3 shows a comparison between the two detectors that had the best photopeak efficiency. In order to obtain the best spectral resolution on a remote sensing mission (whether in-situ or in orbit), the HPGe detector would seem the obvious choice. HPGe has a high atomic number and when cooled to 77 K, the leakage currents are small. However, the cryogenic cooling equipment required to operate the detector makes HPGe a power hungry and heavier option than a scintillator (Moszynski et al., 2006). Power, mass and volume are commodities that a planetary lander or sub-surface probe do not have in abundance and often miniaturisation is necessary to minimise the impact on engineering requirements while maximising the science return.

Property	HPGe	LaBr ₃ (Ce)
Volume of detector element (mm ³)	90822	12870
Atomic number (Z)	32	57, 35
Density (g cm ⁻³)	5.3	5.29
Bias (V)	+ 3500	+ 500 (for PMT)
Radiation tolerance (dose equivalent in silicon (krad))	60 (pre-irradiation performance could not be gained through annealing)	> 1000
Operational temperature (K)	77	Cooling not required
Mass (kg)	~ 2.5	~ 0.2
Cost Considerations	Higher than LaBr ₃ (Ce) due to the need for cooling equipment	No cooling equipment needed

Table 4-3. Properties of the HPGe and LaBr₃ detectors (Ambrosi et al., 2005; Owens et al., 2007a and 2007b).

Any space mission to another planetary body involves travelling through the interplanetary medium where particle radiation can be high; therefore, instruments have to be radiation tolerant or shielded to survive the journey. Shielding increases the mass of the spacecraft. Table 4-4 shows the typical proton fluences that a spacecraft may be subjected to in orbit of Mercury, Earth and Jupiter and the GCR proton fluence in interplanetary space. In HPGe detectors, displacement damage (due to the interaction of ionising and non-ionising radiation e.g. protons, electrons and neutrons) increases the electron and hole trapping centre density, therefore the mobilities of the electrons and holes in the material are reduced, resulting in signal loss. For space-based applications an n-type HPGe detector is traditionally used with an applied negative bias. In this configuration the electrons travel further to the inner contact rather than the holes (See Chapter 3, Section 3.7.1). Since electrons have far higher mobilities than holes, this reduces the impact of the damage on the detector response, which is why n-type materials are used for space missions rather than p-type (Darken and Cox, 1995). Owens et al. (2007b) carried out a study to expose an n-type HPGe detector to proton fluences of between 8×10^8 protons cm^{-2} and 6×10^{10} protons cm^{-2} , with a spectrum similar to the solar proton event of August 1972. These fluences are what a spacecraft may experience on a mission to Mercury. It was found that when exposed to a fluence of up to 6×10^{10} protons cm^{-2} (dose equivalent of 60 krad in Si), the required annealing time (where the detector is heated to repair the particle damage to the crystal, restoring the efficiency and resolution) increased from ~ 1 week (when exposed to a proton fluence of 8×10^8 protons cm^{-2}) to ~ 4 months, and pre-irradiation performance could not be reached (See Table 4-4). Annealing periods of weeks and months would reduce the time available to gather data, decreasing the scientific value of the instrument.

Table 4-4 shows that HPGe would need annealing for approximately once a year due to the GCR proton fluences while undergoing an interplanetary cruise. A HPGe detector on an inner solar system mission (e.g. to Mercury) would need regular periods of annealing. Any spectral analysis software would have to take into account peak tailing as a result of the damage accrued between annealing sessions. The MESSENGER mission to Mercury features a HPGe detector; annealing periods of two weeks are required every year to restore its performance (Goldsten et al., 2007). A HPGe detector would not be practical for a mission to Jupiter and its moons. For example, Europa orbits at 9.5 R_J ; such a mission could expose a detector to $> 10^{11}$ protons cm^{-2} year^{-1} , high enough for the HPGe to need extensive periods of annealing throughout the mission. It is also necessary to consider the cumulative proton exposure of a detector (and therefore detector damage) throughout a mission. For example, as seen in the Table, the Earth's proton environment extends to $3R_E$, and this energetic proton environment can contribute significantly to the proton exposure of a detector as a spacecraft passes through it.

Mission Type	Typical Integrated Proton Fluences Experienced (protons cm ⁻²)	HPGe Anneal Times	LaBr ₃ (Ce)
Solar Proton Events (SPE's): Proton fluence per event (probability per annum of event)			
Mercury (0.39 AU)	10 ⁹ (SPE 90 %)	Weeks -months	Tolerant
	10 ¹⁰ (SPE 70 %)	~ 4 months	
	10 ¹¹ (SPE 12 %)	Anneal times impractical	
	10 ¹² (SPE 1 %)		
Earth (1 AU)	10 ⁸ (SPE 90 %)	~ 1 week at 100°C	Tolerant
	10 ⁹ (SPE 70 %)	Weeks -months	
	10 ¹⁰ (SPE 12 %)	~ 4 months	
	10 ¹¹ (SPE 1 %)	Anneal times impractical	
Proton fluence per annum			
Earth (radii from Earth R _E)	10 ¹² at 2 R _E (max)	Dependent on time spent in Earth's magnetosphere	Tolerant
	10 ¹⁰ at 3 R _E (max)		
Interplanetary Cruise throughout solar system	~ 10 ⁸ at GeV energies (GCR)	Days - weeks per annum depending on anneal temperature	Tolerant
Jupiter (radii from Jupiter R _J)	10 ¹⁴ at 2 R _J (max)	Anneal times impractical for an extended stay at Jupiter	Annealing may be required
	10 ¹⁴ at 4 R _J (max)		Tolerant
	10 ¹² at 8 R _J (max)		
	10 ¹¹ at 12 R _J (max)		

Table 4-4. Typical integrated proton fluences (integrated above 10 MeV unless stated) expected for various solar system missions and the HPGe/ LaBr₃(Ce) anneal times required after an SPE or after an exposure of 1 year (Owens et al., 2007a, 2007b; Jun and Garrett, 2005; Brückner et al., 1991).

'Tolerant' implies tolerant to the flux in the second column, i.e. there was no measurable degradation in the energy resolution of the detector (Owens et al., 2007).

The HP³ mole had a limited volume in which to accommodate a set of detectors. CdTe detectors are a low mass alternative to HPGe that have reasonable resolutions (3 % at 0.662 MeV); however, single, high quality (low defect and impurity concentration) large volume ($> \text{cm}^3$) CdTe crystals are difficult to manufacture (Simon, 2008). It could be possible to stack a number of CdTe planar detectors to improve the efficiency while minimising the effects of trapping; however, this does increase the complexity of the detector read-out, and a large number of stacked detectors would be required to produce the interaction volumes necessary for high energy GRS. The hemispherical detector has a large volume of 500 mm³; Ambrosi et al. (2006) determined that it could carry out GRS with an acceptable efficiency up to 2.5 MeV. There are a number of important elemental lines at above 7 MeV in GRS. Ambrosi et al. (2006) indicated that theoretically four hemispherical detectors could be used to provide a detector volume of 2000 mm³ that could enable GRS up to 10 MeV (while still fitting within the HP³ mole), but this would again increase the complexity of the detector read-out. In contrast the production of large volume HPGe and LaBr₃(Ce) detectors is well established, and Quarati et al. (2007) found that the performance (resolution) of LaBr₃(Ce) does not change significantly with increasing crystal size (between volumes of 900 mm³ to 103,000 mm³).

Unlike the hemispherical CdTe and CsI(Tl) detectors, the LaBr₃(Ce) detector had both good resolution (~ 3.4 % at 0.662 MeV) and a higher photopeak efficiency than the HPGe detector. The total mass of the crystal, housing and PMT was 350 g, far less than a HPGe detector with all the necessary cryogenic cooling equipment. The approximate mass of a GRS package containing 2 \varnothing 25.4 mm x 25.4 mm LaBr₃(Ce) detectors that would be suitable for a geophysical package (aimed at composition and heat flow measurements)

including PMT and space-qualified detector electronics is ~ 250 g (~ 600 g including a MCA- see Table 4-5). This is a significant advantage for an in-situ mission where the available mass for scientific applications is extremely limited; further miniaturisation may be possible. As Figure 1-1 demonstrates, the available space in sub-surface probes is limited; in this case the detector is restricted to a diameter of 25 mm. However, the volume of the detector could be increased by making the detector longer.

Detector system component	Mass (g)	Volume (cm ³) Dimensions (cm)	Power (W)
LaBr ₃ (Ce)	69 x 2	13 x 2 (\varnothing 2.5 x 2.5)	-
PMT	18 x 2	13 x 2 (\varnothing 2.5)	0.125 x 2
ASIC	10	0.2 (1.0 x 1.0 x 0.2)	0.1
HV supply	31	16 (4.6 x 1.2 x 2.9)	1.15
MCA	< 300	235 (16.5 x 7.1 x 2.0)	0.3
Total (with $\sim 20\%$ margin)	< 620	< 340	< 2.2

Table 4-5. The mass, volume, and power requirements of the basic geophysical package (Ball et al., 2007; Hamamatsu, URL:http://jp.hamamatsu.com/en/product_info/). ASIC=Application specific integrated circuit.

The mass and volume of the LaBr₃(Ce) detector could be reduced further by using a more compact PMT. For example, the BURLE PlanaconTM PMT is 51 mm x 51 mm x 1.7 mm (BURLE, 2005) while the PMT used in this experiment (the Photonis XP 2060) is \varnothing 39 mm x 86 mm (Photonis, 2007). The LaBr₃(Ce) detector would also not require additional power for cryogenic cooling like the HPGe detector. The high bias for the LaBr₃(Ce)

detector is required for the PMT, this could be reduced by choosing another PMT or photodiode, but further study is required to find a suitable replacement and the choice may be mission dependent (there may be a trade-off between power requirements, size, radiation tolerance etc.). Although the $\text{LaBr}_3(\text{Ce})$ crystal performance is very temperature stable, the Photonis XP2060 PMT coupled to it is not (Moszynski, 2006); however, it is possible to replace the PMT with another more temperature stable PMT or photodiode. The high radiation tolerance of the material would also make it suitable for a planetary surface mission on a body with a thin or no atmosphere such as the Moon or Mars or on surfaces in intense radiation environments such as Europa. Owens et al. (2007b) carried out a study of the radiation tolerance of $\text{LaBr}_3(\text{Ce})$ detectors by irradiating them with the same proton energy spectra as the HPGe study to a fluence of 10^{12} protons cm^{-2} . They concluded that the material was radiation tolerant to a proton fluence of up to 10^{12} protons cm^{-2} (dose equivalent of 1 Mrad in Si). As a result the detector would be better suited to inner solar system GRS missions (where the radiation environment is more intense) than CdTe and HPGe that are not tolerant to those proton fluences (See Table 4-4). From the work carried out by Owens et al., it can be assumed that this detector would be suitable for any in-situ planetary science mission in this solar system, and that the detector would be suitable for carrying out GRS throughout any SPEs that occurred during the mission lifetime with the addition of a suitable anti-coincidence shield. A shaping amplifier and MCA that can cope with high count rates would also be necessary.

The $\text{LaBr}_3(\text{Ce})$ detector spectra had a number of γ -ray lines from naturally occurring radioactive isotopes in the detector crystal itself (See Figure 4-7). These were identified by comparing the background to the source γ -ray spectra. In all cases, a γ -ray line was

identified at ~ 1.460 MeV, which had two contributions; the 1.436 MeV γ -ray from the naturally occurring isotope ^{138}La and the 1.461 MeV ^{40}K decay line (from the room background). When fitted the ratio of the two contributions (^{138}La to ^{40}K) of the peak was 3:1. The two peaks have merged because the detector does not have sufficient resolution. Knowledge of the exact concentration of ^{138}La can be used to deconvolve the merged peaks, which will be essential if using the $\text{LaBr}_3(\text{Ce})$ detector for radiometric dating (the 1.461 MeV ^{40}K peak is required for this; see Chapter 2). Buis et al. (2007) reported that $\text{LaBr}_3(\text{Ce})$ crystals can contain $\sim 0.09\%$ of ^{138}La , which also emits γ -rays at 0.789 MeV (not visible in Figure 4-7). Actinium contamination is also common in these crystals, which can produce up to 10 lines in the 0.1 MeV to 0.5 MeV energy range. Buis et al. also lists the activation lines when the detector has been irradiated with a proton spectrum similar to that of an SPE spectrum. These lines would need to be subtracted from any planetary spectra collected on another planetary body by accurately characterising the detector on the ground.

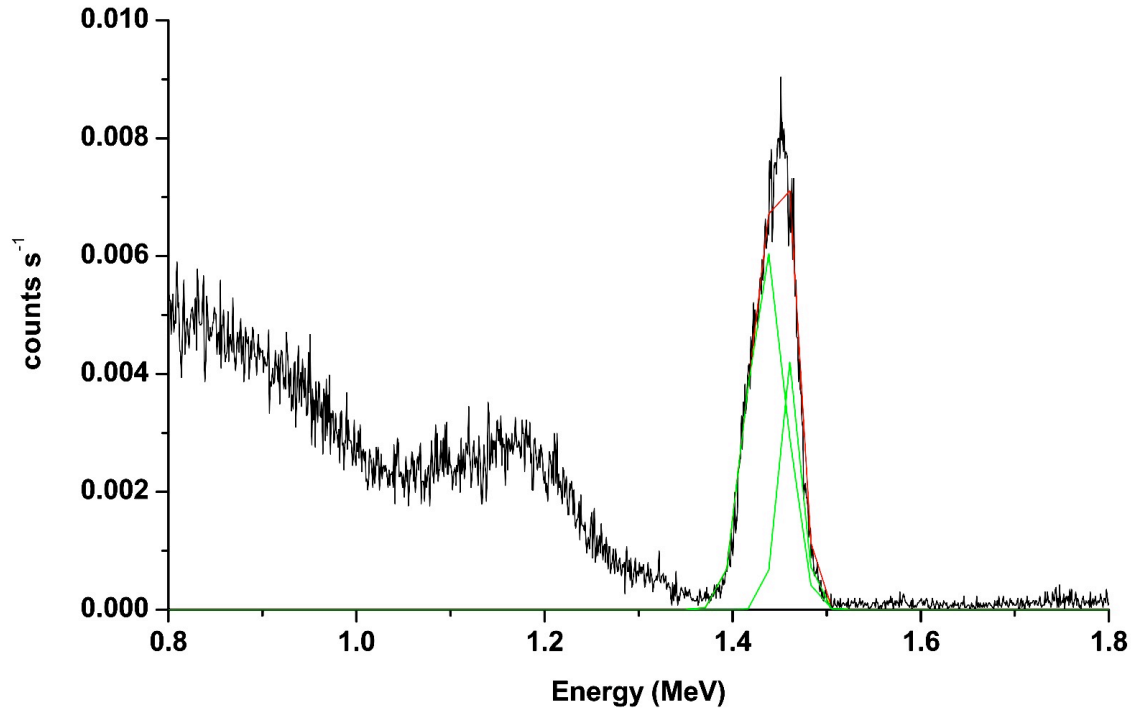


Figure 4-7. The background of the $\text{LaBr}_3(\text{Ce})$ detector.

The $\text{LaBr}_3(\text{Ce})$ spectrum contains background lines at the 0.511 MeV annihilation energy and a merged peak at ~ 1.4 MeV that has two contributions; the 1.436 MeV line from the radioactive ^{138}La content of the crystal and the 1.461 MeV ^{40}K peak from the room background (in the ratio 3:1). The other line from the La isotope at 0.789 MeV was not visible in the spectrum.

4.5.1 High-Energy Performance of the $\text{LaBr}_3(\text{Ce})$ Detector Compared with the HPGe Detector

The efficiency of the HPGe and $\text{LaBr}_3(\text{Ce})$ detectors at high energy is predicted in Figure 4-8 by using the data gathered on this campaign and fitting it with a power function. The ‘response function’ of the $\text{LaBr}_3(\text{Ce})$ detector follows an $E^{-0.90 \pm 0.03}$ power law and the HPGe an $E^{-0.71 \pm 0.03}$ power law.

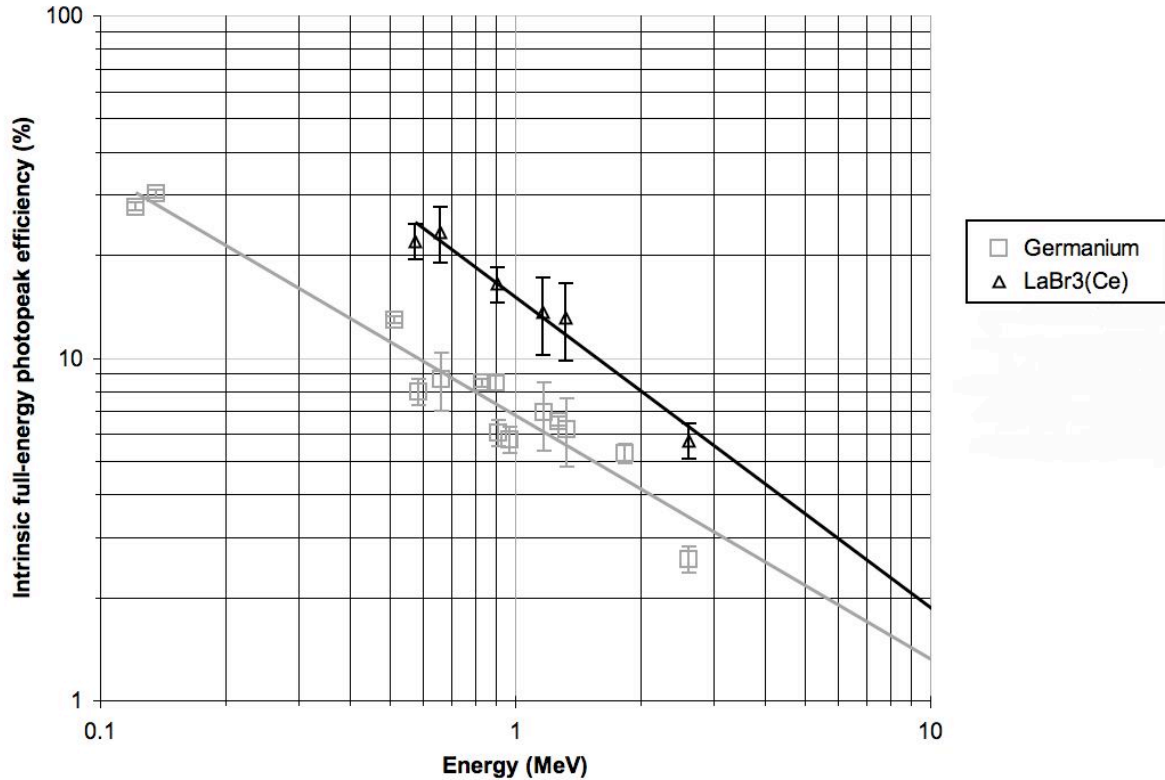


Figure 4-8. The high-energy performance of the HPGe and LaBr₃(Ce) detectors.

Despite the larger volume of the HPGe detector, the LaBr₃(Ce) detector is more efficient up to energies of 10 MeV.

Extrapolating to 10 MeV, the resolution of the LaBr₃(Ce) detector is 1.86 ± 0.16 % while the HPGe detector resolution is 1.32 ± 0.15 %. Evans et al. (2007) detailed the planetary γ -ray lines that the 2001 Mars Odyssey γ -ray spectrometer could resolve from orbit, and Lawrence et al. (1998) describe that there are many overlapping γ -ray peaks present in the Lunar Prospector γ -ray spectra due to the poor resolution of the BGO spectrometer. From Table 1 in Evans et al. and Lawrence et al., it can be seen that the LaBr₃(Ce) detector could resolve a lot of these primary planetary lines. Overlapping lines from the BGO spectra of the Lunar surface could be resolved; for example, the 6.915 MeV ($^{16}\text{O}(n,\gamma)$), 7.115 MeV ($^{16}\text{O}(n,\gamma)$) and the 6.760 MeV ($^{48}\text{Ti}(n,\gamma)$) all contribute to a peak at 6.978 MeV. There are some lines that could not be resolved even with LaBr₃(Ce); for example the two Fe γ -ray

lines at 7.631 MeV and 7.645 MeV would be indistinguishable given that the FWHM for the detector at these energies are 36.43 keV and 36.6 keV respectively. Using a Monte Carlo method to deconvolve/ determine the relative contributions of the overlapping γ -ray lines may be possible.

4.6 Conclusion

Two scintillator detectors and two semiconductor detectors were evaluated and compared to an HPGe detector. The trade-offs between using the different detectors in an in-situ mission were discussed and a recommendation was made on the most suitable detector for the geophysical package. The $\text{LaBr}_3(\text{Ce})$ detector appeared to be the most suitable detector for future in-situ planetary science missions. The resolution of the detector is inferior to a HPGe detector, but is still sufficient to resolve a large number of planetary γ -rays compared with the BGO scintillator detector (used on the Lunar Prospector spacecraft), while still retaining the superior efficiency that is associated with scintillators. Its relatively low mass, low power requirements and room temperature operation make it an ideal candidate for the γ -ray detectors of the geophysical package, since mass, volume and power will be heavily constrained on a planetary lander or sub-surface probe.

Chapter 5

Development and Verification of a Monte Carlo Model using Experimental Data

5.1 Introduction

This chapter describes the experimental verification of a Monte Carlo model developed using the MCNPX code. An experiment was performed at the Forschungs-Neutronenquelle Heinz Maier-Leibnitz (FRM-II) facility in Munich, Germany. Several calibration samples and terrestrial analogues of Martian meteorites were irradiated in a thermal neutron beam. The γ -ray data obtained from the samples and analogues were then compared to modelled γ -ray data to evaluate the model when simulating the detection of the γ -ray emissions from materials that are similar in composition to a planetary body (i.e. modelling the detector in-situ on a planetary body). The model was shown to be in good agreement with the experimental data. This model could ultimately be used to interpret the γ -ray data obtained by a γ -ray spectrometer (i.e. the geophysical package) on the surface or in the sub-surface of a planetary body.

5.2 Prompt γ -ray Activation Analysis

Prompt Gamma Activation Analysis (PGAA) is a nuclear analytical technique that can be used to determine the composition of a sample by using the γ -rays that are emitted as a

result of neutron irradiation. PGAA differs from GRS in that it only considers those γ -rays created via neutron capture reactions (the technique uses a thermal neutron beam). In contrast GRS examines γ -rays created by all the mechanisms listed in Chapter 2, Section 2.4 (Révay and Belgya, 2004). The advantages of PGAA over other analytical techniques are the same as those described in Chapter 2 for GRS; in addition, PGAA leaves little to no residual radioactivity in the sample, so an object analysed in this way can be reused and stored without any special requirements. The possible terrestrial uses of PGAA are extensive and include: screening of cargo at airports for explosives and other sensitive locations, food contamination analysis, the analysis of the composition of fossil fuels and the purity of materials; the analysis of the environmental impact of pollutants and the non-destructive analysis of archaeological samples (Sueki et al., 1996). These applications require neutron sources to induce PGAA.

5.3 Planetary Radiation Environment Modelling with MCNPX

A radiation environment model has been developed by M. Skidmore with the MCNPX code to simulate γ -ray instrumentation in-situ on the surface or in the sub-surface of a planetary body. MCNPX is a general purpose, 3D Monte Carlo radiation transport code developed by the Los Alamos National Laboratory that is capable of modelling coupled particle transport through matter (Pelowitz, 2005). MCNPX can model the physics associated with GCR and SCR interactions with matter, ranging from the intranuclear cascade that result in neutron generation to the eventual photon (γ -ray) production can all be modelled. It has previously been used to model the interaction of GCRs with planetary bodies including the Moon (McKinney et al., 2006). The model can be adapted to any

planetary surface. In the laboratory, calibration samples of known composition can be exposed to well-characterised neutron sources in order to carry out accurate GRS experiments with unknown samples to determine their compositions. Such measurements are rendered more difficult in orbit or on the surface of another planet; therefore, a Monte Carlo model that incorporates the estimated composition of a planetary surface is traditionally used to convert GRS data into concentration estimates of each element on the planetary surface. A comparison between the model and the data will enable the iterative refinement of the model until the composition used in the model accurately matches the results obtained from in-situ or remote sensing measurements. A model such as this (called a Forward model) has been used to interpret γ -ray data obtained by the γ -ray spectrometer on 2001 Mars Odyssey. The model developed by M. Skidmore was verified by comparing it to the γ -ray data acquired when PGAA was carried out on seven samples of known composition.

The model initially had a composition similar to the Martian surface for the purposes of the verification, but may be altered to model other planetary bodies, with or without atmospheres. Ideally this model should be verified using meteorite samples (to simulate the detector on the surface of the planetary body) and data acquired in-situ or in orbit around a planetary body. However, Martian meteorites are rare on Earth (~60 out of ~35,000 meteorites are from Mars) and are very difficult to obtain, especially in quantities of grams or more. Instead terrestrial analogues of Martian meteorites were used to verify the model because destructive methods could be used such as XRF, mass spectroscopy, chemical and gas analysis methods to determine their compositions. A description of these techniques can be found in Dyar et al. (1995) and Kring et al. (1995). The measured compositional

data was then used to produce a Monte Carlo model of the analogues to compare the modelled γ -ray data directly to the experimentally obtained PGAA data. The model is able to incorporate any detector with a known response function (otherwise known as efficiency as a function of energy, see Chapter 4). An accurate model could vastly improve the quality of the interpretation of any measurements a geophysical package might make in-situ on a planetary surface.

Section 5.4 summarises the experimental campaign carried out in January 2008 in the Advanced Neutron Tomography and Radiography System (ANTARES) facility at the FRM-II neutron reactor in Munich to irradiate seven samples of known composition and examine their γ -ray emission. Section 5.5 discusses the verification of the MCNPX model using the acquired data.

5.4 PGAA at FRM-II

The FRM-II reactor facility in Munich, Germany consists of a high flux neutron source that relies on the fission of a compact enriched uranium silicide core contained in a D₂O tank (TUM, 2001). The types of research carried out at FRM II include: condensed matter research, nuclear and applied physics research and the irradiation of samples for medical and neutron activation analysis techniques.

The Advanced Neutron Tomography and Radiography System (ANTARES) facility at FRM II is used for thermal neutron radiography and activation studies. The beam line includes filters and apertures to alter the intensity of the beam and to select parts of the

neutron spectrum. The facility is described in detail in Lorenz et al. (2008). The multi-filter consists of four crystals (sapphire, single bismuth crystal, polycrystalline bismuth crystal and beryllium) mounted in a wheel of polyethylene. Lorenz et al. studied the effects of the filters on the neutron beam intensity and published the data in 2008. This data was used to produce an input spectrum for the MCNPX model.

5.4.1 Terrestrial Analogues of Martian Meteorites

Meteorites that have Martian origins provide a way for scientists to determine the composition of the surface of Mars in more detail than can be achieved by remote methods. In a remote sensing mission, the number and type of analysis techniques used to determine surface composition depend on the mass and power constraints of the remote sensing platform; this is not the case on Earth where more sophisticated chemical and spectroscopic techniques may be used (Dyar et al., 1995). Conclusions on the formation and evolution of meteorites are frequently made by comparing them to analogues found on Earth. For example, a Martian meteorite with a high Fe content is often compared to an analogue from a volcanic region of the Earth that is also mafic to draw the conclusion that the meteorite may have been formed in a volcanic region of Mars.

Two terrestrial analogues of Martian meteorites were obtained from the Smithsonian Institution National Museum of Natural History and one was supplied by G. Benedix (affiliated with the Natural History Museum, London) for this study. They were:

- Theo's flow (TF), clinopyroxenite, Ontario, Canada (NMNH 117255-17, Division of Petrology and Volcanology, Department of Mineral Sciences, Smithsonian Institution).
- Colombian River basalt (CRB), basalt, USA (NMNH 116685, Division of Petrology and Volcanology, Department of Mineral Sciences, Smithsonian Institution).
- Mount Erebus (ME), basalt, Ross Island, Antarctica (supplied by G. Benedix).

As the surface of Mars is dominated by basalt (a rock common on all terrestrial planets), we chose to look at two different basalts from Earth. Basalt can have a variety of compositions and the two basalts used in this study, although not exact compositional analogues to Martian meteorites, do sample two different types of basalt. The TF analogue is a documented chemical analogue to the Martian meteorite, Nakhla (Lentz et al., 1999).

Two 5 g samples of each rock were sent to the University of Leicester Geology department for XRF analysis (using the PANalytical Axios Advanced XRF spectrometer) to determine their bulk composition. Each of these powdered samples was produced from different parts of the primary samples in order to reduce the effect of the heterogeneity of the samples. Table 5-1 shows the average concentration of each element in the samples. There was significant variation in the concentration of trace elements in each of the different samples of the analogues, which has implications in estimating the uncertainties imposed on the measurements. Since the bulk composition of the analogues was of primary interest, an average composition estimated from two samples regions of each analogue was deemed to be sufficient to give a representative average composition measurement of the bulk of the analogue.

Element	CRB		TF		ME	
	% (WF)	Error	% (WF)	Error	% (WF)	Error
Si	23.55	0.12	23.56	0.21	20.40	0.10
Ti	1.78	0.03	0.43	0.01	2.22	0.05
Al	6.92	0.01	2.68	0.08	7.59	0.19
Fe	10.94	0.07	7.80	0.02	8.65	0.13
Mn	0.16	0.01	0.15	0.01	0.15	0.05
Mg	2.54	0.01	8.78	0.28	5.43	0.72
Ca	6.04	0.02	11.49	0.18	6.97	0.22
Na	2.06	0.08	0.67	0.01	3.20	0.05
K	1.11	0.08	0.03	0.01	1.75	0.09
P	0.25	0.08	0.02	0.01	0.36	0.01
S	0.02	0.02	0.02	0.01	0.02	0.01
O	44.34	0.16	43.65	0.38	43.60	0.06
	ppm	Error	ppm	Error	ppm	Error
Ba	503.44	63.15	11.90	7.10	504.09	29.05
Ce	57.81	0.05	9.47	1.24	169.46	0.05
Cl	2670	5	57	4	14	4
Co	28.80	16.02	59.79	0.05	29.82	19.39
Cr	32.85	24.94	1402.43	29.73	395.35	156.29
Cs	-	-	-	-	3.79	0.05
Cu	20.92	8.87	14.92	0.91	34.25	8.08
Ga	22.86	0.15	8.66	0.73	21.80	1.81
La	24.08	0.05	4.37	0.05	84.46	0.05
Mo	2.45	0.05	1.20	0.15	6.61	0.58
Nb	14.42	0.50	1.73	0.39	117.40	9.25
Nd	28.88	0.05	8.64	0.05	74.05	0.05
Ni	5.96	1.09	278.57	4.67	152.57	46.54
Pb	7.56	0.39	2.48	0.84	2.07	0.39
Rb	33.86	1.44	2.38	0.75	44.29	3.70
Sc	56.92	12.5	67.83	5.83	377.28	6.43
Se	2.91	0.05	1.89	0.05	4.20	0.05
Sn	-	-	-	-	1.56	0.05
Sr	321.24	2.08	45.71	2.19	1009.01	30.57
Th	4.45	0.44	1.35	0.24	6.89	0.8
U	1.99	0.01	1.76	0.05	1.38	0.11
V	400.54	26.21	219.96	8.77	252.48	2.56
Y	45.94	0.95	15.10	0.35	36.69	0.70
Zn	137.86	1.14	65.44	1.87	103.58	2.82
Zr	203.53	1.83	41.83	0.70	483.17	22.43

Table 5-1. XRF compositional analysis of the Martian analogues (WF= weight fraction).

In addition to the three analogues, several calibration samples were produced at the University of Leicester containing particular elements of interest. Four samples were created; acid washed sand was used as a dilution agent and elements of interest in Martian surface studies (Cl, H and Fe) were added. Boynton et al. (2004) have determined the concentration of these elements over the Martian surface based on the γ -ray data collected by the 2001 Mars Odyssey γ -ray spectrometer. One sample containing only sand was used as a reference. Lithium hydroxide (LiOH) and polyvinylidene chloride (PVDC) were used to simulate an H content of $\sim 0.5\%$ in a planetary surface. The PVDC also contained Cl, although the concentration of Cl would be far in excess of what would be detected on Mars ($\sim 9.7\%$, whereas the concentration on the Martian surface is $\sim 0.5\%$ (Boynton et al., 2004)). Iron filings were used to simulate a silicate-based surface composed of $\sim 12.5\%$ Fe. The combination of using PGAA on the calibration samples and rock analogues had the additional advantage of being able to verify the model for regolith material with a density of $\sim 1-2\text{ g cm}^{-3}$ and more rocky/granular material with a density of $\sim 3\text{ g cm}^{-3}$ that may be encountered on a planetary surface.

Any material used to suspend the calibration samples and analogues would also be exposed to the neutron beam and would contribute to the γ -ray emission. The solution was to use plastic (low-density polyethylene) bags that are composed of predominantly H and C. This would mean that the H would contribute to the H signal (C has a very small thermal neutron capture cross-sections, so it was unlikely a peak would be detected since the plastic bag had a low mass compared to the calibration samples and analogues).

5.4.2 ANTARES Test Campaign

A diagram of the experimental chamber and the equipment configuration is shown in Figure 5-1. The calibration samples and analogues were suspended from a boom such that it was directly in the path of the neutron beam and directly above the γ -ray detector. This configuration was chosen to minimise the activation of the detector by the neutron beam. A large volume Ortec[®] GEM-15200-P HPGe detector, coupled to an Ortec[®] 570 spectroscopy amplifier and an Ortec[®] Maestro-32 MCA emulator (Version 6.06) was used to measure the γ -ray emission from the analogues. The bias was supplied by an Ortec[®] 459 HV supply.

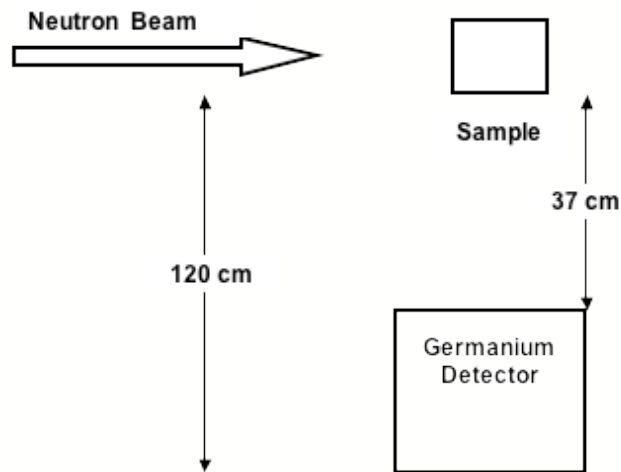


Figure 5-1. A diagram of the experimental set up in the ANTARES chamber.

The amplifier was set at minimum gain ($\times 10$); however, it still limited the detection of γ -rays to below 4.3 MeV. This meant that important neutron capture γ -ray peaks could not be detected, such as the 7.631 MeV and 7.645 MeV peaks for ^{56}Fe . However, many of the elements with these high energy peaks have lower energy counterparts that could be used for the γ -ray analysis. The HPGe detector was calibrated with several standards; ^{22}Na , ^{54}Mn , ^{88}Y and ^{57}Co .

Three filters were used in the beam line to reduce the dead time of the detector from 100 % to 6 %. They consisted of:

- A 5 cm thick polycrystalline Bi filter and a 5 mm thick Pb filter that attenuated the γ -ray background in the beam.
- A Cd filter with a \varnothing 2 mm pinhole aperture that reduced the flux of the neutron beam.

The samples and analogues were exposed to the beam for periods not exceeding 40 minutes.

5.4.3 Spectral Fitting

A sample γ -ray spectrum from the sand calibration sample is shown in Figure 5-2 with the key Si and H (from the sample container bag) γ -ray peaks. For comparison, a spectrum from the ME analogue (the analogue that produced one of the most complex spectra) is shown in Figure 5-3. The Al peak was very large compared with the other peaks that were from the calibration sample/ analogue. The HPGe detector was supported by an Al structure. The γ -rays from the activation of the Al and the detector material contributed to the γ -ray spectrum collected. It was impossible to separate the contributions to the Al γ -ray peaks from the support structure and the analogues, therefore the Al peaks could not be used in the verification process. The data was reduced by:

- a) Subtracting the background that was present with no sample in the beam (the background spectrum was collected over the same time period as the calibration samples/analogues).

- b) Fitting and subtracting the additional background created when the sample was in the beam (the sample contributed to the neutron scatter, affecting the background). As seen in Figure 5-2 and Figure 5-3, the background from the ME analogue is larger than that obtained from the sand calibration sample. This is because the ME analogue density was greater than the sand sample, and the ME analogue had a larger surface area exposed to the neutron beam. This caused a greater degree of scatter from the neutron beam as it hit the analogue; the additional scatter increased the γ -ray background from the chamber/Al structure/detector.
- c) Identifying each peak and calculating the peak areas (the count rate of each peak). The peak areas were calculated by fitting them with Gaussian functions in OriginTM. The HPGe detector was calibrated before and after the irradiations; the detector showed negligible radiation damage by the neutron beam (the calibration peaks had no low energy tails), therefore the peaks could be fitted accurately with Gaussian functions.

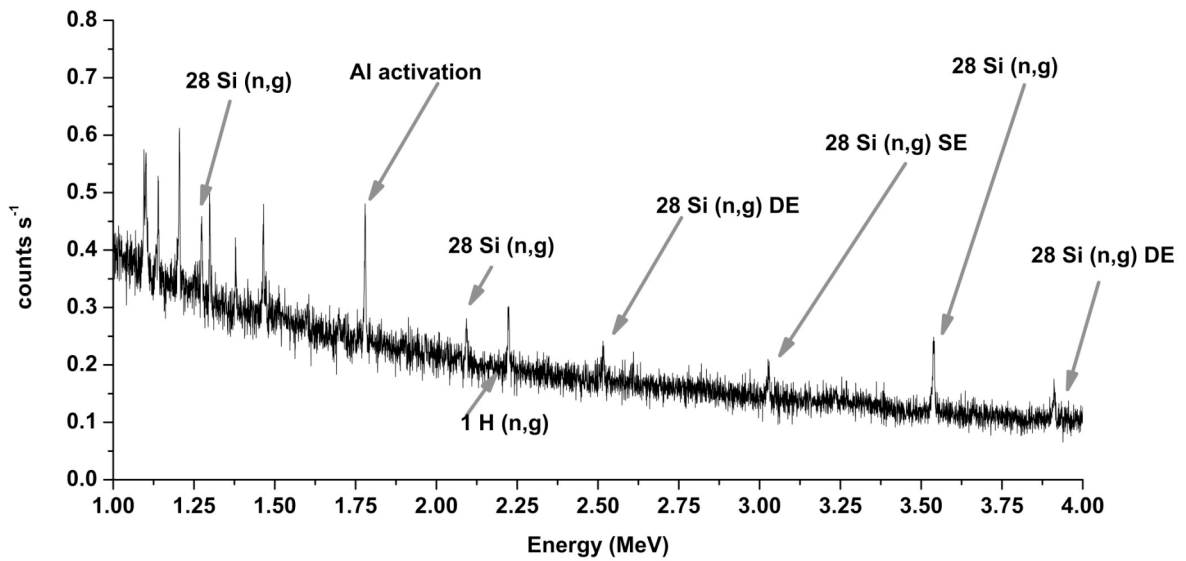


Figure 5-2. A portion of the spectrum from the sand calibration sample. The Si, Al and H peaks have been labelled. A single escape peak is labelled as SE and a double escape peak is labelled as DE.

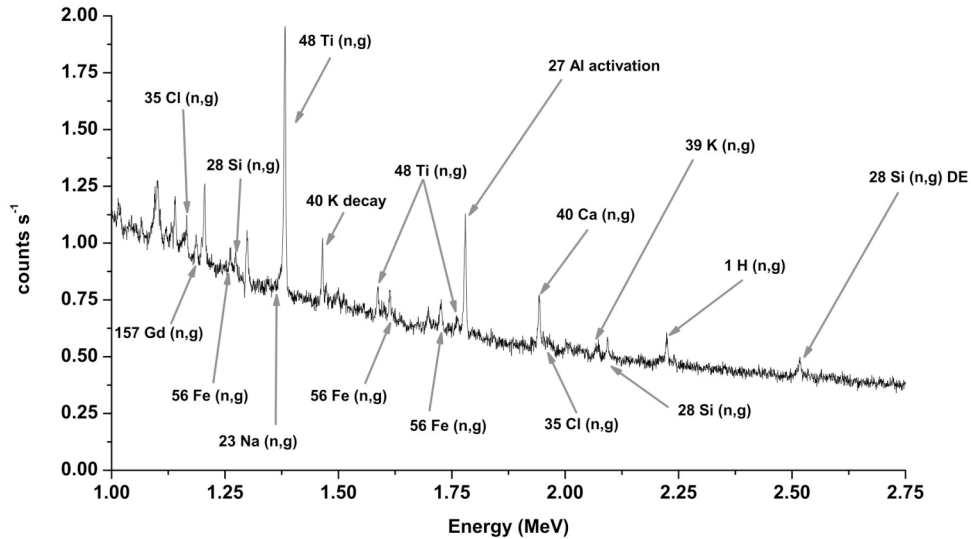


Figure 5-3. A portion of the spectrum from the ME analogue with the strongest γ -ray peaks labelled. A single escape peak is labelled as SE and a double escape peak is labelled as DE.

It was possible to identify many lines in the spectra that did not originate from the calibration samples and analogues. Although the beam was well collimated, thermal neutron scatter contributed to the signal by interacting with other structures in the experimental facility. Many of the γ -ray background peaks could be attributed to the HPGe detector itself. The background signal from the detector changed once a sample was placed in the beam line and there was an increase in the intensity of the peaks associated with the HPGe crystal. This was attributed to increased neutron scatter. For example, the neutron capture line at 0.595 MeV from the HPGe detector approximately doubled in intensity when the ME analogue was placed in the beam. The background from the experimental chamber also increased once a sample was placed in the beam. The B neutron capture reaction $^{10}\text{B}(n,\alpha\gamma)^7\text{Li}$ from the borated polyethylene lining the chamber walls produced a broad peak at 0.478 MeV that also doubled in intensity when the ME analogue was placed in the beam. The remaining peaks in the spectra were identified using the prompt γ -ray spectrum catalogue (Révay et al., 2004). The γ -ray libraries of the major elements present in the samples were examined to identify each of the γ -ray peaks, since these had the greatest abundances.

5.4.4 Results

The γ -ray peak element identification, cross-section and energy of each peak detected is shown in Table 5-2. The γ -ray peaks from the background have been omitted. Révay et al. (2004) was used to identify the γ -ray lines and any interference peaks. The elemental peaks selected to estimate the composition of a planetary surface with the Monte Carlo model are highlighted in bold. These peaks were chosen because they have no interference peaks from

other elements present in the analogues and the γ -ray count rates were relatively high compared to other γ -rays emitted by these elements. The Mg peaks either had overlaps with other elemental peaks or were not statistically significant (i.e. had uncertainties $> 20\%$). The Na peaks were either not statistically significant or were decay peaks from the decay of ^{24}Na (created by neutron capture); decay γ -rays from radioactivity were not modelled.

Energy (MeV)	Element and Reaction	Cross-section (barns)
0.292	$^{35}\text{Cl} (n, \gamma)$	0.089
0.314	$^{55}\text{Mn} (n, \gamma)$	1.46
0.342	$^{48}\text{Ti} (n, \gamma)$	1.84
0.352	$^{56}\text{Fe} (n, \gamma)$	0.273
0.390	$^{24}\text{Mg} (n, \gamma)$	0.00586
0.436	$^{35}\text{Cl} (n, \gamma)$	0.309
0.520	$^{35}\text{Cl} (n, \gamma)$	7.58
0.585	$^{24}\text{Mg} (n, \gamma)$	0.0314
0.632	$^{35}\text{Cl} (n, \gamma)$	0.111
0.692	$^{56}\text{Fe} (n, \gamma)$	0.137
0.768	$^{39}\text{K} (n, \gamma)$	0.903
0.787	$^{35}\text{Cl} (n, \gamma) / ^{35}\text{Cl}(n, \gamma)$	171/271
0.847	$^{55}\text{Mn} (n, \gamma) / ^{56}\text{Fe} (n, n\gamma)$	13.1
0.898	$^{56}\text{Fe} (n, \gamma)$	0.054
0.936	$^{35}\text{Cl} (n, \gamma)$	0.172
0.984	$^{48}\text{Ti} (n, \gamma)$	0.114
1.131	$^{35}\text{Cl} (n, \gamma)$	0.626
1.165	$^{35}\text{Cl} (n, \gamma)$	8.91
1.186	$^{39}\text{K} (n, \gamma)$	0.16
1.260	$^{56}\text{Fe} (n, \gamma)$	0.0684
1.273	$^{28}\text{Si} (n, \gamma)$	0.0289
1.374	$^{23}\text{Na} (n, \gamma) *$	0.53
1.382	$^{48}\text{Ti} (n, \gamma)$	5.18
1.461	^{40}K decay	
1.499	$^{48}\text{Ti} (n, \gamma)$	0.297
1.586	$^{48}\text{Ti} (n, \gamma)$	0.624
1.601	$^{35}\text{Cl} (n, \gamma)$	1.21
1.613/ 1.614/ 1.619	$^{56}\text{Fe} (n, \gamma) / ^{39}\text{K} (n, \gamma) / ^{39}\text{K} (n, \gamma)$	0.153/ 0.119/ 0.13
1.726	$^{56}\text{Fe} (n, \gamma)$	0.181
1.762	$^{48}\text{Ti} (n, \gamma)$	0.311
1.943	$^{40}\text{Ca} (n, \gamma)$	0.352
1.951	$^{35}\text{Cl} (n, \gamma)$	6.33
1.960	$^{35}\text{Cl} (n, \gamma)$	4.10
2.001	$^{40}\text{Ca} (n, \gamma)$	0.0659
2.034	$^{35}\text{Cl} (n, \gamma)$	0.239
2.074	$^{39}\text{K} (n, \gamma)$	0.137
2.075	$^{35}\text{Cl} (n, \gamma)$	0.252
2.094	$^{28}\text{Si} (n, \gamma)$	0.0331
2.209	$^{23}\text{Na} (n, \gamma)$	0.0259

2.224	$^1\text{H} (n, \gamma)$	0.333
2.311	$^{35}\text{Cl} (n, \gamma)$	0.35
2.519	$^{23}\text{Na} (n, \gamma)$	0.0699
2.677	$^{35}\text{Cl} (n, \gamma)$	0.533
2.801	$^{35}\text{Cl} (n, \gamma)$	0.183
2.846	$^{35}\text{Cl} (n, \gamma)$	0.349
2.870	$^{35}\text{Cl} (n, \gamma)$	1.82
2.975	$^{35}\text{Cl} (n, \gamma)$	0.377
3.026/ 3.027	$^{48}\text{Ti} (n, \gamma) / ^{48}\text{Ti} (n, \gamma)$	1 3/26
3.061	$^{35}\text{Cl} (n, \gamma)$	1.13
3.540	$^{28}\text{Si} (n, \gamma)$	0.119
3.916	$^{24}\text{Mg}(n, \gamma) / ^{48}\text{Ti} (n, \gamma) / ^{48}\text{Ti} (n, \gamma)$	0.032/ 0.13/ 0.0839

Table 5-2. γ -rays detected in the calibration samples and analogues by the HPGe detector at the ANTARES facility (Révay et al., 2004). The * indicates that the isotope created by the capture is radioactive and that γ -ray line is due to the radioactive decay of the isotope. (n, γ) = neutron capture reaction, (n, n γ) = inelastic scatter reaction. The escape peaks created in the HPGe detector are not included in this Table.

Energy (MeV)	Element	Average count rate per gram (counts s ⁻¹ g ⁻¹)	Error (counts s ⁻¹ g ⁻¹)	Present in analogue/ calibration sample
0.342	⁴⁸ Ti	0.2578	2.50 x 10 ⁻³	ME, CRB
0.352	⁵⁶ Fe	0.0302	9.55 x 10 ⁻⁴	ME, TF, CRB, FE
0.768	³⁹ K	0.0839	7.41 x 10 ⁻³	ME, CRB
1.164	³⁵ Cl	0.5445	1.59 x 10 ⁻²	ME, PVDC
1.382	⁴⁸ Ti	0.2338	3.17 x 10 ⁻²	ME, TF, CRB
1.586	⁴⁸ Ti	0.0285	7.67 x 10 ⁻⁴	ME
1.726	⁵⁶ Fe	0.0067	1.22 x 10 ⁻³	ME, TF, CRB, FE
1.943	⁴⁰ Ca	0.0185	1.51 x 10 ⁻³	ME, TF, CRB
1.951	³⁵ Cl	0.2508	2.31 x 10 ⁻²	ME, PVDC
2.001	⁴⁰ Ca	0.0032	6.26 x 10 ⁻⁴	ME, TF
2.094	²⁸ Si	0.0019	3.37 x 10 ⁻⁴	ME, TF, CRB, SI, FE, LiOH, PVDC
2.224	¹ H	0.6081	4.35 x 10 ⁻²	ME, TF, CRB, SI, FE, LiOH, PVDC
2.677	³⁵ Cl	0.0133	7.02 x 10 ⁻⁴	PVDC
2.870	³⁵ Cl	0.0517	3.55 x 10 ⁻⁴	PVDC
3.540	²⁸ Si	0.0038	5.43 x 10 ⁻⁴	ME, TF, CRB, SI, FE, LiOH, PVDC

Table 5-3. The average count rate per gram of each element within the analogues/ calibration samples for the primary elemental peaks (those highlighted in Table 5-2). SI= Sand calibration source; FE= Fe calibration source; PVDC= Cl and H calibration source; LiOH= H calibration source.

Table 5-3 shows the average count rate per gram of each of the statistically significant peaks in the analogues and calibration samples that could be used for elemental analysis (the peaks highlighted in bold in Table 5-2). Only the peaks with less than a 20 % uncertainty in the count rate are included. This meant that only the major elements of the analogues could be measured because they were present in large enough quantities to

produce a significant count rate. Very few statistically significant peaks could be attributed to trace elements due to the limited exposure times of each analogue/sample and the high γ -ray background. The trace element peaks detected typically had large neutron capture cross-sections, e.g. the capture cross-sections for Cl are several barns or more for the peaks listed in Table 5-2.

The ME analogue had γ -ray peaks at 1.165 MeV and 1.951 MeV, which could not be attributed to any of the strong γ -ray peaks of the major elements. These γ -ray energies were consistent with the strongest γ -ray lines of Cl (1.165 MeV and 1.951 MeV). Although Cl is only present in trace amounts (2670 ppm), its neutron capture cross-section is large (See Table 5-2); there is evidence that ME and other volcanic basalts may contain Cl (Buccianti and Prati, 1993; Kyle et al., 1992; Sano et al., 2005).

By comparing the count rate per gram of H present in the analogues/samples, it was evident that the TF analogue contained a small amount of H that could not be attributed to the plastic bag suspending it (possibly in the form of a hydroxide), estimated at $\sim 1.2 \text{ g} \pm 0.1 \text{ g}$ or $0.17 \% \pm 0.015 \%$ of the total mass of the TF analogue (Kyle et al., 1992).

5.5 Modelling the γ -ray Emission from PGAA using MCNPX

MCNPX was used to model the γ -ray emissions from the calibration samples and analogues. A model of the experiment was created with the geometry shown in Figure 5-1. The bulk density of each calibration sample/analogue was assumed to be uniform

throughout the sample/analogue (the density of the calibration samples was approximately $\sim 1.6 \text{ g cm}^{-3}$ and the analogues 3 g cm^{-3}). The background from the chamber and the detector (without any calibration sample/analogue in the beam) was measured and subtracted so this was not considered in the model (this reduces the complexity of the model).

MCNPX combines cross-section and reaction libraries with physical models in a single code (Pelowitz, 2005). The neutron cross-sectional data and photon production data used were from the Evaluated Nuclear Data File (ENDF/B-VI and -VII) libraries. Only low energy neutrons were modelled, so the data up to neutron energies of 20 MeV were used where available. Elements with no cross-sectional information in the ENDF databases or that had no photon production data utilised models by default.

5.5.1 The Model

Although ANTARES is predominately a thermal neutron beam facility; there is still a measurable epithermal neutron component present that will also contribute to the γ -ray emissions from the calibration samples/ analogues. The unfiltered ANTARES neutron spectrum is shown in Figure 5-4. The total unfiltered flux of the beam was $\sim 4.6 \times 10^{10} \text{ cm}^{-2}\text{s}^{-1}$. This spectrum was separated into 125 bins of increasing energy and the average contribution to the total neutron flux from each bin formed the input into the MCNPX program. In the campaign several filters were added to attenuate the neutron beam and γ -rays originating from the beam line that were listed in Section 5.4.2. The unfiltered beam was modelled passing through the Bi, Pb and pinhole filters to get the neutron

spectrum expected at the position of the calibration samples and analogues. The resultant neutron spectrum is shown in Figure 5-4; which demonstrates that the filters cut out the thermal neutron component below 10^{-10} MeV and attenuated the rest of the neutron spectrum. The total neutron flux fell from $\sim 4.6 \times 10^{10} \text{ cm}^{-2}\text{s}^{-1}$ to $\sim 1.5 \times 10^7 \text{ cm}^{-2}\text{s}^{-1}$ by including the filters. This was the spectrum used to model the γ -ray emission from the analogues.

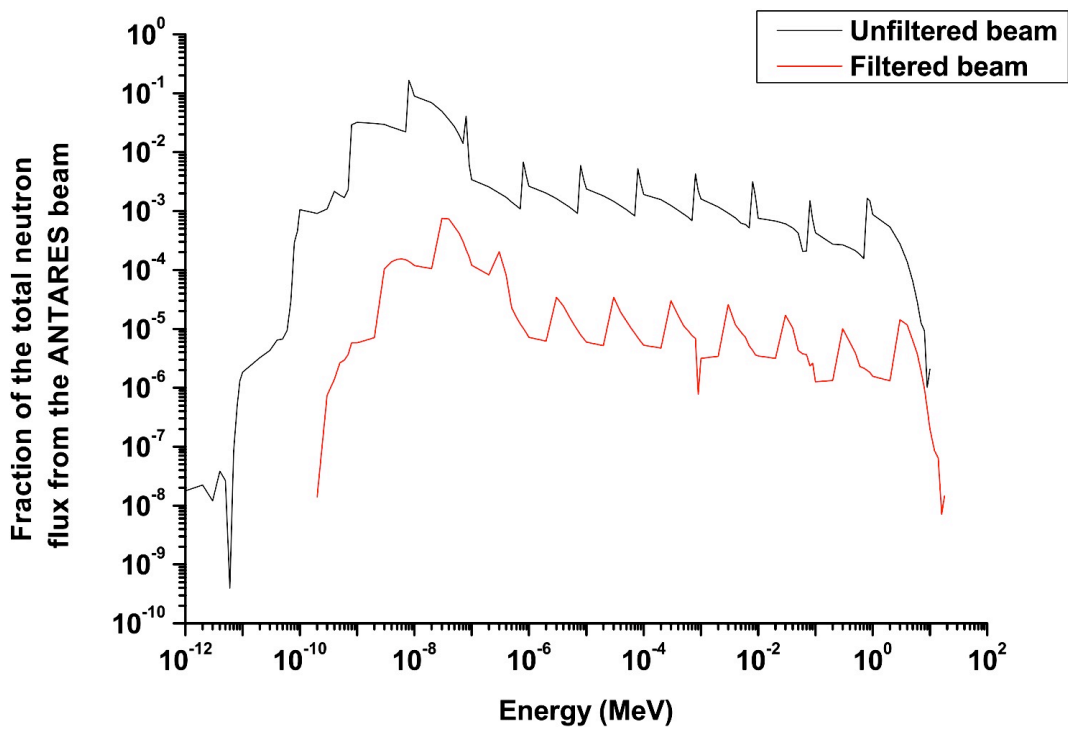


Figure 5-4. The unfiltered and filtered neutron spectrum that was provided by the ANTARES team and input into MCNPX. The spectrum was divided into 125 energy bins and the input was used in the MCNPX program.

The calibration samples and analogues were modelled using the compositions listed in Section 5.4.1 and in Table 5-1. The H in the plastic bag was also included in the composition of the modelled analogues/sample. Based on the experimental results, 1.2

grams of H was also added to the composition of the TF analogue (See Section 5.4.4). Based on the literature (Buccianti and Prati, 1993; Kyle et al., 1992; Topinka, 2007), 4 ppm of Sm and Gd were added to the ME and CRB analogue compositions in the model. Sm and Gd are strong thermal neutron absorbers and their presence in the analogues could affect the resultant γ -ray emission. Only neutron capture reactions were considered i.e. all other secondary processes that created γ -rays (including electron reactions) were not considered in the model. The detector was modelled as a void cylinder of dimensions \emptyset 4.79 cm x 5.04 cm and was positioned 37 cm below the analogues as shown in Figure 5-1. The spectrum of γ -rays entering the void detector was output from the simulation. Only γ -rays that entered the detector cell volume were tallied. The modelled γ -ray count rates for each peak highlighted in Table 5-2 were converted into the count rates detected by the HPGe detector using a response function ϵ as a function of energy E that was calculated in Chapter 4, corrected for the detector thickness and is expressed as $\epsilon(E) = kE(keV)^{-0.85 \pm 0.03}$, where k is a constant.

5.5.2 Results

The ratios of the experimental to modelled count rates for each element are shown in Figure 5-5 and Figure 5-6. These were peaks that had no interferences with other elemental peaks (See Table 5-2) and were statistically significant (< 20 % uncertainty). The modelled data is in good agreement with the experimental data; the experimental and modelled count rates are within 20 % of each (when taking the error into account) with the exception of a number of the TF lines; the possible reasons for the discrepancy are detailed in the discussion.

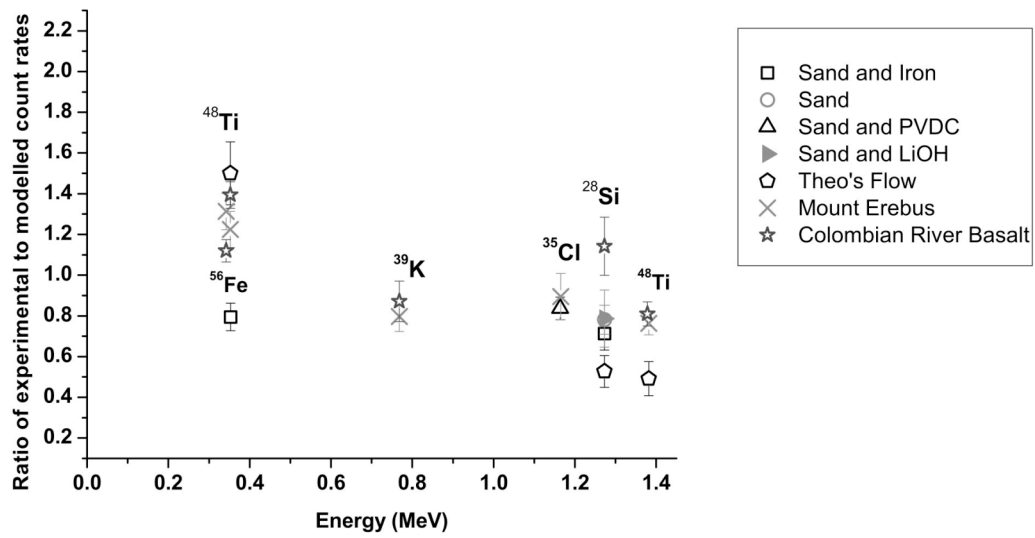


Figure 5-5. The ratio of the experimental to the modelled count rates for each γ -ray peak present in the calibration samples and analogues that had less than a 20 % uncertainty in the energy range 0 – 1.45 MeV and is highlighted in Table 5-2.

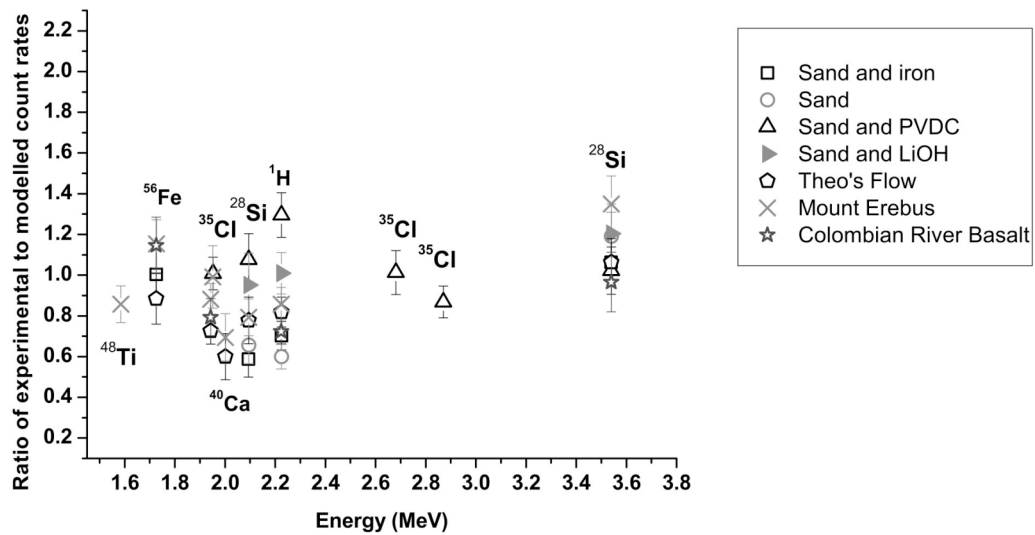


Figure 5-6. The ratio of the experimental to the modelled count rates for each γ -ray peak present in the calibration samples and analogues that had less than a 20 % uncertainty in the energy range 1.45 – 3.6 MeV and is highlighted in Table 5-2.

5.6 Discussion

There are always differences between model and experiment; these differences and their causes need to be understood. In general the modelled and experimental count rates were within 20 % of each other when taking into account the associated errors. Figure 5-5 and Figure 5-6 show that some of the experimental data to model ratios had values less than 1 (for example, a number of the TF ratios); there are several possible reasons for this, one was that the model did not take into account that the presence of the sample/ analogue in the beam changed the background count rate in the γ -ray spectrum. γ -rays from the chamber and the HPGe detector could have reduced the signal to background ratio. This effect could be partially responsible for suppressing the experimental count rate. The contribution of the aluminium structures in the chamber, the borated polyethylene lining the chamber walls and the HPGe detector itself to the γ -ray spectrum was investigated. It was found that the room background did not produce any line features that may have interfered with the γ -ray lines of interest and the continuum they produced did not suppress the γ -ray lines of interest. Another possible cause of the discrepancy was that the model did not take into account that the analogues/ calibration samples had rough surfaces (the model assumed that they were perfectly smooth). Rough surfaces would increase the degree of neutron scatter, thereby reducing the number of neutron interactions in the analogues/ calibration samples and the elemental γ -ray count rates. This would cause the experimental to modelled ratios to be less than 1. Modelling this effect was not possible.

Some of the lines of the analogues had ratios slightly lower (e.g. the CRB ^{56}Fe line at 1.726 MeV) or higher (e.g. the ME ^{28}Si at 3.540 MeV) than that of the same lines from the

calibration samples. The calibration samples were easy to model because they were homogeneous and their densities would be constant throughout the sample, therefore they had ratios close to 1. It was also easy to model their shapes within MCNPX. By contrast the analogues were heterogeneous, it was only possible to take an average density of the analogues and they were irregularly shaped. In the model the analogues were assumed to be homogeneous based on the average composition obtained from two samples in different regions of the analogues, assumed to have a constant density and had a cuboid shape. If the averaged composition across the whole analogue for an element was higher than modelled, or the density varied significantly (i.e. some regions were more dense than the average) across the analogue this could account for the experimental to modelled count rate ratios being slightly greater than 1 because the modelled count rate would be lower than the experimental one. A ratio of less than 1 indicates that the analogue had an average composition lower than that modelled or that the density was lower than modelled in some regions. Although the surface area of the analogues exposed to the beam could be accurately modelled, there were variations in the thicknesses of the analogues that were difficult to model accurately. A thinner region of an analogue would mean that fewer neutron interactions would take place, causing the experimental to modelled count rate to be less than 1. Where some of the analogues had ratios of greater than 1, this could indicate that the thickness of the regions where the neutron beam hit the analogues were higher than modelled. A solution to this problem would be to crush the analogues to homogenise them and to mould them into a shape that can be easily modelled (this was not possible because the CRB and TF analogues had to remain intact by request of the Smithsonian).

5.6.1 Limitations of the Monte Carlo Model

One of the disadvantages of this experiment is that it was not possible to examine the performance of the model at higher energies (4- 10 MeV), where many important capture γ -rays may be found e.g. ^{56}Fe at 7.631 MeV and 7.645 MeV. These limitations were imposed by the detector system response. A broader response could be achieved in the future by replacing the detector preamplifier with one that could process very high count rates (reducing the dead time), replacing the amplifier with one that could provide the necessary gain to process γ -rays up to 10 MeV, and using a detector that has a larger volume. The model needs to be verified at both higher γ -ray energies (4 – 10 MeV) and over a broader neutron spectral range (neutrons of thermal, epithermal and fast energies). It is also desirable to compare the model to real data gathered by γ -ray spectrometers in orbit around a planetary body. In order to achieve this data from Lunar Prospector and 2001 Mars Odyssey have been used to verify the model. The response of γ -ray spectrometers on these spacecraft range up to ~ 10 MeV. This work is described in Chapter 6.

Another limitation was the inability to detect the trace elements in the analogues with the exception of Cl. The concentration of the trace elements was low compared to the major elements; therefore the background may have been a limiting factor. The peaks detected that could be attributed to trace elements had large uncertainties in both the weight fraction and the count rates. A possible solution to these problems would have been to expose the analogues for longer time periods (this may be possible in the future) and to sample more regions of the analogues to reduce the uncertainty in the content of the analogue. The ME analogue model was used to estimate the time required to get a 10 % precision on some of

the trace element peaks if a future study was carried out; the strongest peaks of Cr and Ba (Révay et al., 2004) could get a 10 % precision within an exposure time of a few hours; however, for elements that have concentrations of only a few ppm (e.g. Th, U), the time required is > 30 hours. The Monte Carlo model will be used to determine the limits of detectability of trace elements on a planetary surface for various detectors given a realistic measurement period for a typical in-situ profile and will be reported in Chapter 8. The Mg peaks at 0.390 MeV and 0.585 MeV and the radioactive decay peaks of Na (created by neutron capture) were not present in the results from the model so the experimental peaks could not be used in the model verification.

5.7 Conclusion

A Monte Carlo radiation environment model designed to model geophysical instrumentation on the surface or in the sub-surface of a planetary body was verified using experimental data. Several terrestrial analogues of Martian meteorites and calibration samples of known composition were exposed to a thermal neutron beam at FRM II in Munich, Germany to induce γ -ray emission. It was found that the γ -ray emission could be attributed to the major rock-forming elements of the analogues and the elements of the calibration samples. The γ -ray emissions together with the known compositions of the analogues and samples (to represent a planetary surface) were used to verify a Monte Carlo model. The ratio between the modelled and experimental count rates generally gave consistent results (within 20 %) for elements that were common to the analogues and calibration samples. The model had a number of limitations, which will be remedied by

verifying the model using data acquired by the γ -ray spectrometer on 2001 Mars Odyssey.
This work will be reported in Chapter 6.

Chapter 6

Development and Verification of a Monte Carlo Planetary Radiation Environment Model using γ -ray Data from Lunar Prospector and 2001 Mars Odyssey

6.1 Introduction

Chapter 6 details the further development of the Monte Carlo radiation environment model to verify it for modelling the GCR, magnetospheric and solar wind interaction with a planetary body and for modelling orbital instrumentation. The model simulates the intranuclear cascade of high energy particles (GCRs and SCRs) that result in neutron generation to the eventual γ -ray production. It was verified using data from the γ -ray spectrometer on 2001 Mars Odyssey to compare it to ‘ground truth’ data from the surface of Mars and to evaluate its performance when modelling a detector with a known response function. Three different regions of the Martian surface were modelled and the modelled count rates for Si, H, Cl, Fe, Th and K were compared with the count rates obtained by the spectrometer. The model count rates were comparable with the experimental data. The model was then altered to reflect a lunar surface using Lunar Prospector data to verify the model was working.

Characterising a planetary radiation environment is important to: 1) investigate the interactions between the surrounding radiation environment (GCR, solar wind and magnetosphere) with the atmosphere, surface and sub-surface of a planetary body, 2) assess the habitability of a planetary body for indigenous life, 3) assess the risks associated with manned exploration missions to a planetary body and 4) predict/ interpret the results that remote sensing instrumentation may obtain from a planetary body (e.g. interpret the γ -ray emissions from a planetary surface produced by natural emissions from radioisotopes or PGAA to obtain meaningful estimates of the concentration of certain elements on the surface of a planet).

6.2 Verification Methodology

The radiation environment model was extended to investigate the interactions of a planetary body with the surrounding radiation environment, compare the performance of different γ -ray detector technologies (in-situ and in orbit) and their ability to determine the age, composition (the concentration of major rock-forming elements and trace elements to a high precision) and bulk density of a planetary surface. The model described in Chapter 5 was verified experimentally using the γ -rays detected by a γ -ray spectrometer when several terrestrial analogues of Martian meteorites were irradiated with a thermal neutron beam. The modelled γ -ray count rates for the major rock-forming elements were compared to the count rates achieved through experiment to examine the performance of the model when modelling in-situ geophysical instrumentation. However, the planetary model has not been compared to ‘ground truth’ data obtained from current orbital missions such as 2001 Mars Odyssey that features a γ -ray spectrometer with a well-known response function.

Comparing the model to this orbital data will complement the laboratory work detailed in Chapters 4 and 5, because the detector used in this mission was well-characterised on the ground prior to launch, the data will aid in verifying the performance of the model in simulating a detector's performance and will verify the model for orbital instrumentation so it can be used to model geophysical instrumentation in orbit and in-situ.

The estimated Martian surface composition (derived from the γ -ray data collected by the γ -ray spectrometer on 2001 Mars Odyssey using a forward model) was obtained for three different regions of the Martian surface from Boynton et al. (2007). The estimated composition and the γ -ray spectrometer response function were input into the planetary radiation environment model. The model simulated the γ -ray emissions from the Martian surface and the γ -ray spectrometer in orbit. The count rates for each element detected in orbit by the spectrometer were modelled. The model count rates were then compared to the 'ground truth' count rates obtained by the 2001 Mars Odyssey γ -ray spectrometer to determine the ability of the model to simulate the performance of the γ -ray instrumentation and to compare the model output to the 'ground truth' γ -ray data. The model was then altered to reflect a portion of the lunar surface using concentration estimates derived from the γ -ray data obtained by the γ -ray spectrometer on Lunar Prospector. The output of this simulation was used in conjunction with the results obtained from the Martian model to derive the concentration of each element on the modelled lunar surface. If the composition of the surface derived from the model was within error of the composition input into the model then the model can be considered to be working effectively. If the model and experimental results are in good agreement, the model can be used to determine the performance of other γ -ray instrumentation in orbit around or in-situ on other planetary

bodies such as Europa. It may also be used as a forward model to interpret γ -ray data acquired in the course of future planetary science missions.

6.3 Verifying the Model using 2001 Mars Odyssey γ -ray Data

6.3.1 γ -ray Data and Compositional Estimates from 2001 Mars Odyssey

A description of the 2001 Mars Odyssey γ -ray spectrometer can be found in Chapter 3, Section 3.8. The 2001 Mars Odyssey γ -ray spectrometer team created elemental maps for H, Cl, Si, K, Fe and Th from the γ -ray data and published their data in 2007 (Boynton et al., 2007). The published maps were in 150 x 150 grids over the 2001 Mars Odyssey primary mission between 8th June 2002 and 2nd April 2005. The derived concentrations of the six elements were extracted from these plots. A map of the surface of Mars is shown in Figure 6-1. Grid 1 covers the region 15° to 30° (Latitude); -45° to -30° (Longitude); and is coincident with the Mars Pathfinder landing site. The elemental composition data is shown in Table 6-1. Two further grids, one in the Northern hemisphere at 0° to 15°; 120° to 135° (grid 2) and one in the Southern hemisphere at -30° to -45°; -135° to -120° (grid 3) were also analysed (See Table 6-1).

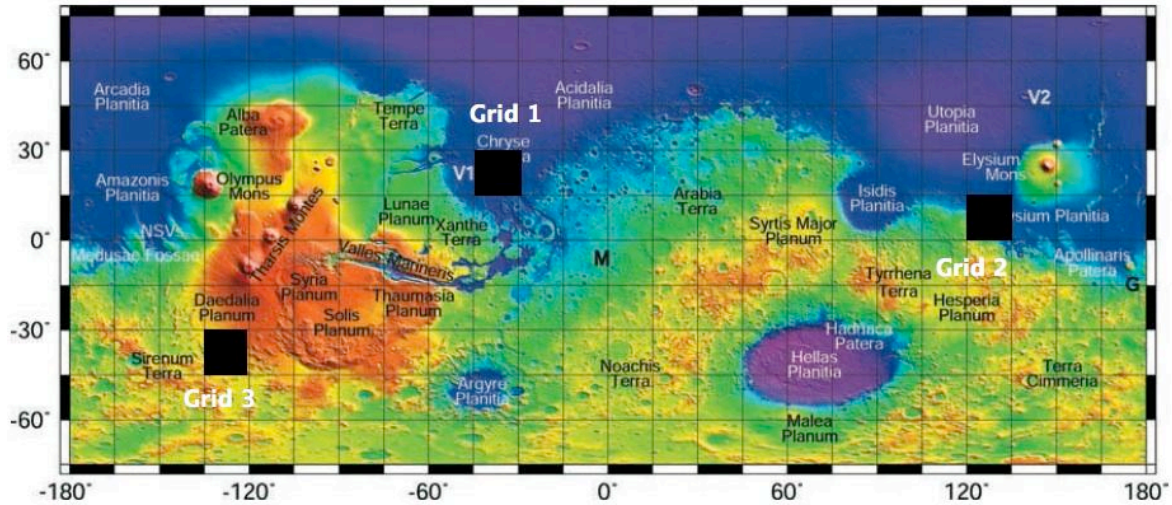


Figure 6-1. A map of the Martian surface, the grids are marked on the map (Boynton et al., 2007).

Element	γ -ray peak energy (MeV)	Estimated Concentration of the element		
		grid 1 (WF)	grid 2 (WF)	grid 3 (WF)
^{28}Si	1.779 (n,n γ)	$21.5 \pm 0.5 \%$	$20 \pm 0.5 \%$	$20 \pm 0.2 \%$
	3.540 (n, γ)			
^{56}Fe	1.726 (n, γ)	$17 \pm 1.4 \%$	$17 \pm 1.3 \%$	$14 \pm 0.6 \%$
	7.631 (n, γ)			
	7.646 (n, γ)			
^1H	2.223 (n, γ)	$0.3 \pm 0.05 \%$	$0.5 \pm 0.05 \%$	$0.28 \pm 0.03 \%$
^{35}Cl	1.951 (n, γ)	$0.4 \pm 0.05 \%$	$0.6 \pm 0.055 \%$	$0.35 \pm 0.03 \%$
	1.959 (n, γ)			
	6.111 (n, γ)			
^{40}K	1.460 (D)	$0.45 \pm 0.03 \%$	$0.4 \pm 0.025 \%$	$0.3 \pm 0.02 \%$
^{232}Th	2.615 (D)	$0.8 \pm 0.08 \text{ ppm}$	$0.7 \pm 0.07 \text{ ppm}$	$0.6 \pm 0.07 \text{ ppm}$

Table 6-1. A table of the six calculated elemental abundances for grids 1 to 3 in Boynton et al. (2007). The second column contains the key γ -ray peaks that are associated with that element (Boynton et al., 2007) and columns 3-5 show the estimated concentration derived by the 2001 Mars Odyssey γ -ray spectrometer team for the three grids. (n,n γ)= inelastic scattering; (n, γ)= neutron capture; D= radioactive decay generated γ -rays.

The γ -ray spectra for each grid were obtained from the NASA Planetary Data System (PDS) GRS data node (Boynton, 2003). The data consists of cumulative counts of γ -rays over 19.7 second periods binned into 16,384 channels. The γ -ray spectra have been processed so that they have a common energy scale in order to co-add or compare spectra (Crombie et al., 2003). Co-adding spectra often occurs in GRS in order to get a single spectrum with good counting statistics. A Java code was developed to extract the data from the γ -ray data binary files and convert them into ASCII format.

The γ -ray data was co-added in time, over the period ranging from 30th September 2002 to 23rd March 2005. A single spectrum was produced for each grid and the key γ -ray peaks, associated with the six elements mentioned above (See Table 6-1), were analysed. Evans et al. (2007) analysed the γ -ray spectra from the γ -ray spectrometer on 2001 Mars Odyssey and identified all the γ -ray peaks. The γ -ray information from the paper was used to identify the γ -rays in the spectra for each grid. In Chapter 5 the γ -ray peaks were easily fitted with Gaussian functions as the HPGe detector did not sustain damage in the experiment and peaks were chosen that had no other elemental interferences. However, in the 2001 Mars Odyssey γ -ray spectra there were many overlapping peaks and the HPGe detector sustained radiation damage that caused many of the peaks to have low energy tails. Evans et al. (2007) fitted the peaks with Gaussian, multiple Gaussian or asymmetric Gaussian (with a low energy tail, see Equation 6-1) functions to fit the spectra. The same fits were applied to the spectra for grids 1-3. It was necessary in many cases to fit the surrounding peaks to accurately isolate the peak of interest (See Figure 6-3); Evans et al. (2007) was used to identify and fit those peaks.

$$\text{If } x < x_C, \text{ then } y = y_o + \left[\frac{A}{0.5(\sigma_1 + \sigma_2)\sqrt{2\pi}} \exp\left(-0.5\left(\frac{x - x_o}{\sigma_1^2}\right)\right)\right],$$

$$\text{else } y = y_o + \left[\frac{A}{0.5(\sigma_1 + \sigma_2)\sqrt{2\pi}} \exp\left(-0.5\left(\frac{x - x_o}{\sigma_2^2}\right)\right)\right]$$

Equation 6-1

where A is the area beneath the peak, and the other quantities are described in Figure 6-2.

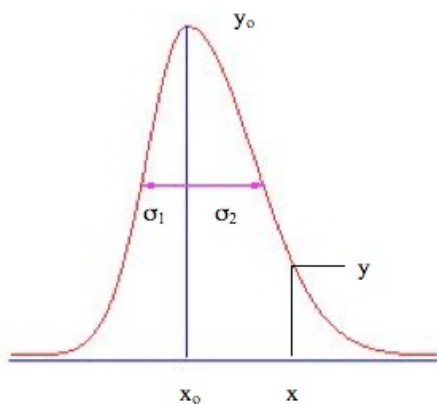


Figure 6-2. A description of the asymmetric Gaussian function.

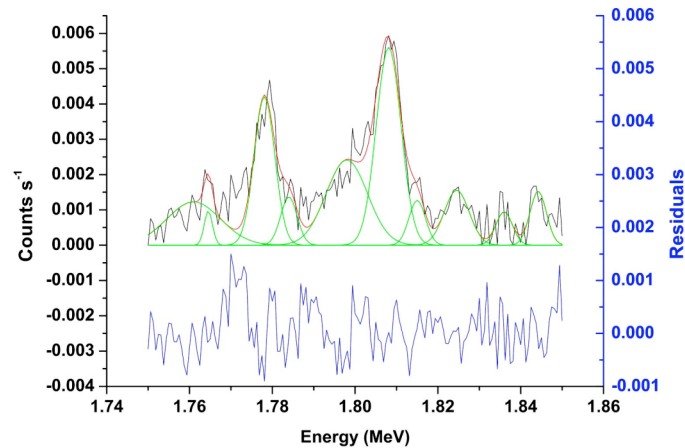


Figure 6-3. Example of the peak fitting procedure carried out in Origin for Silicon at 1.779 MeV. The peaks for Titanium at 1.762, 1.794 and 1.842 MeV, Uranium (^{214}Bi) at 1.764 MeV, Chromium at 1.784 MeV, Magnesium at 1.808 MeV, Iron at 1.810 MeV, Vanadium at 1.824 MeV Strontium at 1.836 MeV had to be fitted as well.

6.3.2 Subtraction of the Spacecraft Contribution to the γ -ray Peaks

GCR and SCR protons generate γ -ray emission from the 2001 Mars Odyssey spacecraft via direct or secondary particle (e.g. neutron) interactions; these can interfere with the emissions from the planetary surface. Since the spacecraft is closer to the γ -ray spectrometer compared to the planetary surface and there were no restrictions placed on the elemental composition of the spacecraft, this contribution may be significant (Evans et al., 2002). The Si, H and Fe γ -ray peaks may have had small contributions from the spacecraft, which the model cannot take into account without prior knowledge of the entire spacecraft composition.

In order to take into account the spacecraft background, Kelly et al. (2007) devised a method of subtracting the background created by the spacecraft. During the Martian winter,

the pole in the hemisphere experiencing the winter is covered with a thick layer of CO₂ ice. This layer is thicker at the southern pole during its winter because the southern hemisphere experiences more extreme winters. This layer of CO₂ ice attenuates nearly all of the γ -ray signal from that part of the planet, therefore the elemental signals collected by the GRS over the south pole over its winter can be assumed to be from the spacecraft and can be subtracted from the integrated count rates obtained for each element (Evans et al., 2007; Kelly et al., 2007). This method would be valid for quantifying the spacecraft contribution to the Si, H and Fe elemental peaks.

The data collected over the southern polar region (-60° to -90° (Latitude)) by the GRS over the Martian winter (11th March 2003- 26th June 2003) (Kelly et al., 2007) was reduced by fitting the spectra using the peak information given in Evans et al. (2007). The H and Fe contributions from the spacecraft were statistically insignificant; however, the Si γ -ray count rate originating from the spacecraft at 1.779 MeV was significant ($\sim \frac{1}{4}$ of the count rate originating from the planet) and was subtracted from the count rate from the peak, leaving only the count rate from the planet. Table 6-2 shows the count rates and uncertainties of H, Cl, Si, Fe, K, Th for grid 1.

Element	Energy (MeV)	Counts per minute in grid 1	Uncertainty in grid 1(%)
²⁸ Si	1.779	0.683	1.5
	3.540	0.155	4.1
⁵⁶ Fe	1.726	0.137	4.3
	7.631	0.302	2.9
	7.646	0.169	3.9
¹ H	2.223	0.289	3.0
³⁵ Cl	1.951	0.176	3.8
	1.959	0.182	3.7
	6.111	0.185	3.7
⁴⁰ K	1.460	3.774	0.8
²³² Th	2.615	0.334	2.8

Table 6-2. A table of the count rates and uncertainties for each peak listed for grid 1. The third column gives the count rate of each peak for the 15° x 15° grid, the fourth the uncertainty in the peak.

6.4 The Martian Monte Carlo Model

6.4.1 The Martian Atmosphere and Surface

A segment of the Martian surface was modelled as a cylindrical structure with a radius of 240 km, which corresponds to the average γ -ray spectrometer swath (See Figure 6-4). The concentration estimates from Boynton et al. (2007) were used in the Monte Carlo model of the Martian surface. The remaining major rock-forming elements were set to the concentration estimates derived by the Mars Pathfinder lander and reported in Kim et al. (2007). Based on these studies by Boynton et al. (2007) and Kim et al. (2007), the total surface composition is given in Table 6-3. The density of the surface was modelled as 1 g cm⁻³ (Masarik and Reedy, 1996).

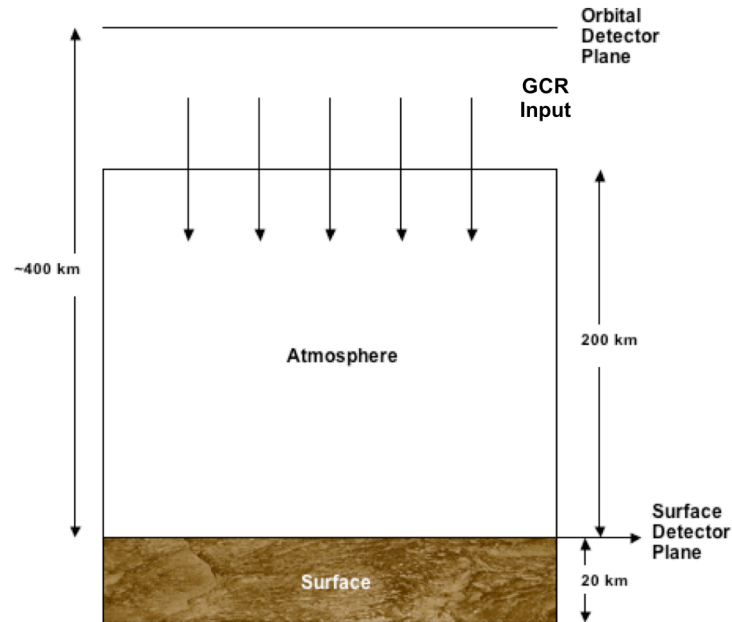


Figure 6-4. The geometry of the Monte Carlo model. The detector was modelled at an altitude of 400 km above the surface.

The atmosphere was modelled with the weight fractions reported in Table 6-3 that were obtained from Masarik and Reedy (1996). The atmosphere was initially modelled as 10 cylindrical regions with varying densities, based on the atmosphere having an average scale height of 10.8 km and a surface density of $0.000016 \text{ g cm}^{-3}$ (Masarik and Reedy, 1996). The atmospheric profile used in the model is shown in Figure 6-5. The topography of the three grids was not the same; grid 1 had an average elevation of -4 km , grid 2 had an average elevation of -1 km and grid 3 had an average elevation of $+2 \text{ km}$; this had implications for the thickness of the atmosphere. Kelly et al. (2007) reported that in the average atmospheric thickness in the northern hemisphere lowlands was $\sim 18 \text{ g cm}^{-2}$ and in the southern hemisphere highlands $\sim 12 \text{ g cm}^{-2}$. The atmospheres for each grid were re-modelled accordingly. The average temperature profile of the atmosphere and surface

was obtained from the Mars Pathfinder Atmospheric structure instrument (Bergman, 2003) for each of the atmospheric regions and is shown in Figure 6-6.

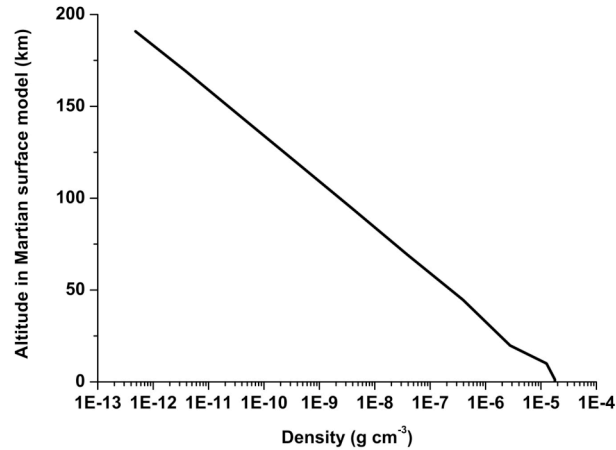


Figure 6-5. The density profile of the modelled Martian atmosphere used in the Monte Carlo model based on an average scale height of 10.8 km.

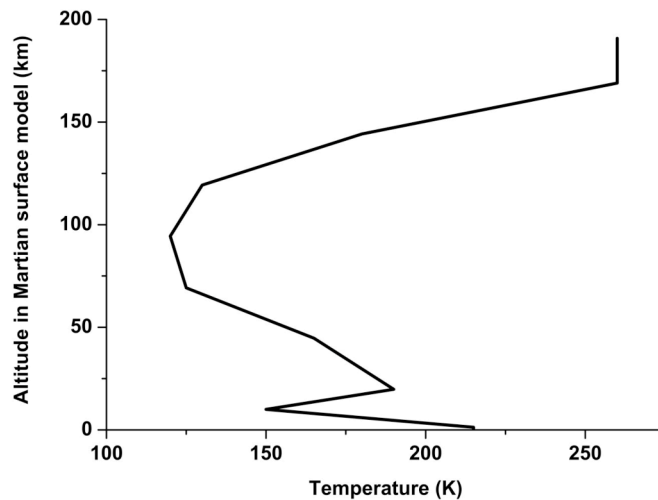


Figure 6-6. The atmosphere temperature profile of the modelled Martian atmosphere. Data taken from Bergman et al. (2003).

Element	Surface Concentration (% WF)	Atmosphere Concentration (% WF)
Si	0.215	
O	0.404	0.6960
Fe	0.17	
Ca	0.0477	
Al	0.0504	
Mg	0.0477	
Na	0.0176	
Ti	0.005	
K	0.0045	
Mn	0.0034	
S	0.02	
Cl	0.004	
H	0.003	
C	0.006	0.2610
Cr	0.0015	
Gd	4×10^{-6}	
Sm	3×10^{-6}	
Th	8×10^{-7}	
U	1.3×10^{-7}	
N		0.0270
Ar		0.0160

Table 6-3. The composition of the Martian surface and atmosphere used in the model for grid 1 (Boynton et al., 2007; Kim et al., 2007; Masarik and Reedy, 1996).

The model was created with the following parameters:

- It was assumed that the planetary surface was flat, local variations in topography were ignored.
- The surface material in the region examined was homogenous.

- The γ -ray spectrum intensity scales linearly with increasing proton flux, as long as the energy distribution of the protons remains constant. This choice made the modelling easier, reducing the time taken to run successive simulations.
- Delayed γ -ray emission was ignored. All the elements listed in Table 6-1 produced prompt γ -rays.
- Only proton and neutron interactions were considered i.e. all other secondary processes that created γ -rays (including electron interactions) were not considered in the model. Only the γ -rays created via neutron reactions were of interest and this would also reduce the time between successive simulations.
- It was assumed that the trace element contribution to the γ -ray spectra was negligible. Only trace elements that had large neutron cross sections (Sm or Gd) or were of interest (Th, Cl) were included in the model. This was to simplify the model output; many trace elements have γ -ray lines that interfere with those of the major rock-forming elements (e.g. Ni has a γ -ray line at 1.455 MeV and K has a γ -ray line at 1.461 MeV) and additional elements would increase the time to run successive simulations. Since the verification did not consider most of the trace elements they were omitted from the modelled surface, but they would have to be introduced in future modelling if trace element detection was being studied.

6.4.2 GCR Flux

The 2001 Mars Odyssey team assumed a negligible production of γ -rays from solar wind protons primarily due to the ability of the thin Martian atmosphere to attenuate protons below 100 MeV. Significant SCR proton fluxes above 100 MeV are only present during

SPEs, and the data acquired during these events was often disregarded because of the increased background and detector deadtime. The GCR proton flux at the top of the atmosphere was modelled using data from Simonsen and Nealy (1991) and is shown in Figure 6-7.

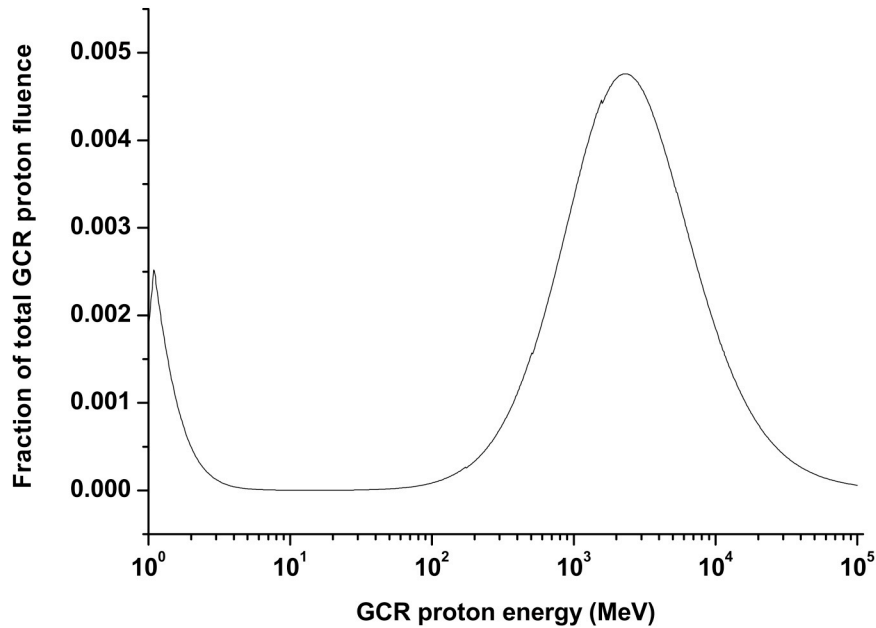


Figure 6-7. The GCR input spectrum into the 2001 Mars Odyssey simulation (Simonsen and Nealy, 1991). The spectrum was divided into 835 energy bins and formed the input into the planetary MCNPX model.

Masarik and Reedy (1996) reported that the GCR flux is $4.56 \text{ nucleons cm}^{-2} \text{ s}^{-1}$ at Mars, $\sim 14 \%$ of this flux consists of α particles and heavier elements. Masarik and Reedy found through Monte Carlo modelling that the particle and γ -ray creation in the surface and atmosphere of Mars due to α particles and heavier elements can be modelled by increasing the overall modelled GCR proton flux by 40 %. (Masarik and Reedy, 1996). This simplifies

the Monte Carlo model and has been applied here. In the simulations 1×10^7 source protons were generated in a monodirectional, parallel beam.

6.4.3 Modelling the HPGe Detector

The γ -ray spectrometer swath has an average radius of 240 km and an average orbital altitude of ~ 411 km (See Figure 6-4). Each grid had a different average elevation and this was taken into account in the model. In the model the γ -ray photons per source proton were measured at an altitude of ~ 411 km. Three correction factors were then applied to the model results:

- 1 To obtain the modelled γ -ray flux cm^{-2} , the γ -ray photons per source proton at an altitude of 411 km were multiplied by the GCR proton flux ($3.92 \text{ cm}^{-2} \text{ s}^{-1}$), then multiplied by a factor of 1.4 to take into account the γ -ray emission created by the GCR α particles and heavier elements.
- 2 The response function of the HPGe detector as a function of energy was taken into account. The response function was obtained from Kerry et al. (2002) and is shown in Figure 6-8.
- 3 The modelled flux absorbed in the detector cm^{-2} was multiplied by the surface area of the detector exposed to the γ -rays originating from the surface to determine the expected count rate (s^{-1}) at the detector.

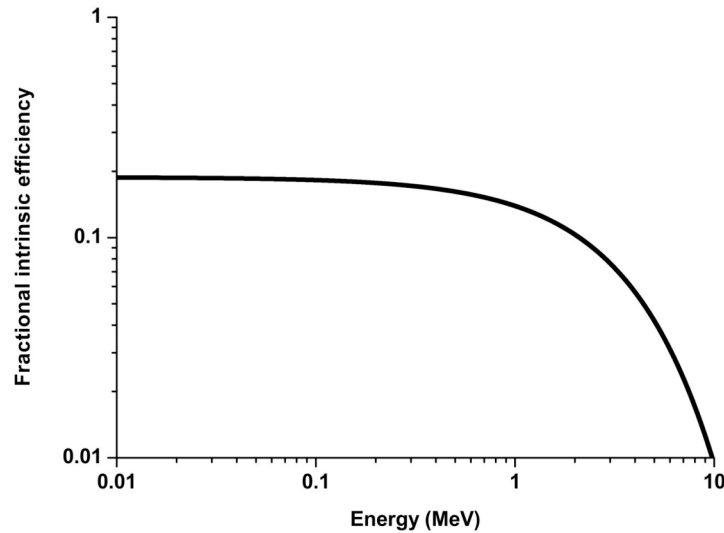


Figure 6-8. The intrinsic efficiency of the HPGe detector on 2001 Mars Odyssey. Data taken from Kerry et al. (2002).

6.4.4 Modelling the Radioactive γ -ray Emission of the Martian Surface

The Monte Carlo model could not directly model the decay of radioactive elements within the surface and their transport through the surface and atmosphere. Instead, a second simulation was carried out using the same Martian atmosphere and surface model with the addition of radioisotopes such as ^{232}Th and ^{40}K producing 2.614 MeV and 1.461 MeV γ -rays respectively. These were modelled as isotropic γ -ray sources with an even emission probability over the whole surface. The number of γ -rays per second emitted from the surface of Mars per gram of surface material (C/m) was estimated using the following equation (GRS team, 2005);

$$\frac{C}{m} = N \times R \times \lambda \times P_{\gamma} \times m_f \quad \text{Equation 6-2}$$

where N is the number of atoms per gram of the radioactive element, R is the fraction of the element that is radioactive, λ is the decay constant of the radioactive species, P_γ is the probability of γ -ray emission at that energy, m_f is the mass fraction of the element in the surface material.

The modelled 2.614 MeV and 1.461 MeV γ -ray photons cm^{-2} per source photon were multiplied by the expected number of decay γ -rays that could be emitted per second from the surface of Mars, and this was used to derive the expected detector count rate (s^{-1}), in conjunction with the correction factors b and c described in Section 6.4.3.

6.5 Verifying the Model using Lunar Prospector γ -ray Data

The Martian model was altered to reflect the lunar surface, the atmosphere was removed and the composition was derived from γ -ray data acquired in orbit by Lunar Prospector. The simulations were carried out in order to verify that the model was working and to validate it for other types of planetary surfaces. This was achieved by comparing the count rate per weight fraction from the Martian model to the lunar surface model and by deriving an estimate of the concentration of Fe, Si, K and Th, on the simulated lunar surface, from these data. The concentration estimates obtained from the model were then compared to the input composition (derived from the Lunar Prospector data). If the concentrations were within error, the model was deemed to be working.

6.5.1 The Lunar Surface

In 2006, the Lunar Prospector team published concentration estimates for the major rock-forming and radioactive trace elements (Si, Ca, Mg, Ti, Fe, K and Th) on the lunar surface. The concentration estimates were derived from the Lunar Prospector γ -ray spectrometer data in conjunction with the Lunar Prospector forward model. The composition of the modelled lunar surface was based on a grid 0° to 20° (latitude); -20° to -40° (longitude) (shown in Prettyman et al. (2006)). The remaining element concentrations were estimated from the Monte Carlo forward modelling carried out by the same authors. The total surface composition is given in Table 6-4. The density of the surface was modelled as 1 g cm^{-3} .

Element	Surface Concentration (WF)
Si	0.1680
O	0.4100
Fe	0.1320
Ca	0.1210
Al	0.0794
Mg	0.0326
Na	0.0026
Ti	0.0216
K	0.0033
Mn	0.0005
P	0.0001
Ni	0.0002
Cr	0.0007
Gd	1.3×10^{-6}
Sm	1.1×10^{-6}
Th	9.3×10^{-6}
U	1.6×10^{-7}
Eu	7.8×10^{-7}

Table 6-4. The composition of the modelled lunar surface, based on the composition estimates derived by Prettyman et al. (2006) for Si, Ca, Mg, Ti, Fe, K, Th and the estimated concentrations used in the Lunar Prospector team's MCNPX modelling of the lunar surface (Prettyman et al., 2006).

6.6 Results

In order to carry out a comparison between the results of the model and experimentally obtained data by the γ -ray spectrometer on 2001 Mars Odyssey, the ratio of the experimental count rate to the modelled detected count rates for the elements of interest were plotted for each grid on the Martian surface (See Figure 6-9). The ratios indicate how

well the model count rate compares to the count rate detected by the γ -ray spectrometer on 2001 Mars Odyssey (i.e. how well the model performs).

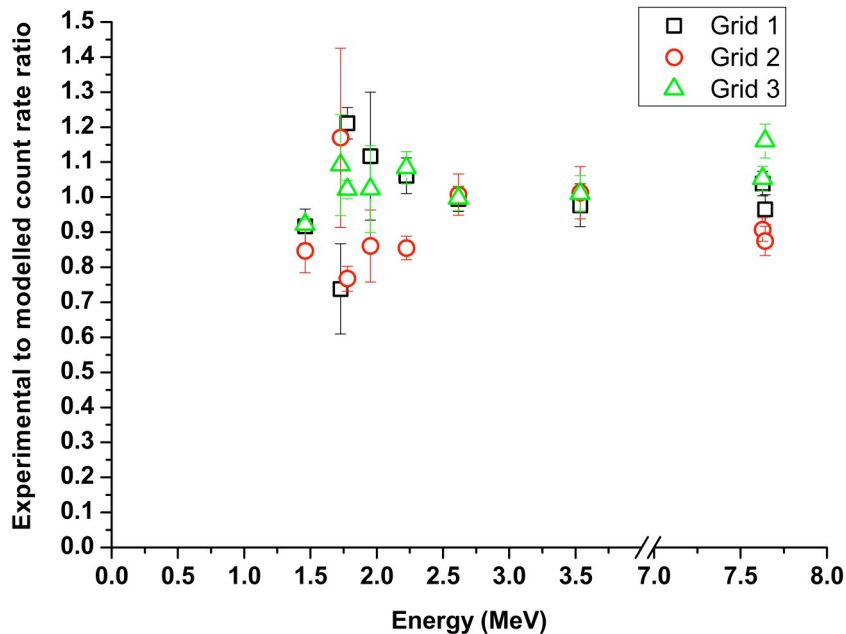


Figure 6-9. The experimental to modelled count rate ratio for the elemental lines given in Table 1 for grids 1 – 3 on the Martian surface. The ratios are generally accurate to within a factor of 20 % when taking into account the associated error.

The Martian model was altered to reflect the lunar surface, the atmosphere was removed and the composition was derived from γ -ray data acquired in orbit by Lunar Prospector. The simulations were carried out in order to verify that the model was working and to validate it for other types of planetary surfaces. The count rate / weight fraction from the Martian model for several elements are shown in Table 6-5. These data were compared to the lunar surface model count rates and an estimate of the concentration of Fe, Si, K and Th on the simulated lunar surface was derived. These estimates were then compared to the original input concentrations (see Table 6-6).

Energy (MeV)	Count rate per minute / WF of element	Error
1.460	1527	98
1.779	4.61	0.23
2.615	646369	72913
3.540	3.06	0.20
6.111	0.016	0.002
7.631	5.13	0.41
7.646	4.39	0.35

Table 6-5. The count rate per minute per weight fraction (WF) of the element for the Martian surface model.

Energy (MeV)	WF as estimated by the LP γ -ray spectrometer	WF derived by model
1.460	0.0033	0.0035 ± 0.00035
1.779	0.168	0.14 ± 0.0012
2.615	9.3×10^{-6}	$1.1 \times 10^{-5} \pm 1.5 \times 10^{-6}$
3.540	0.168	0.19 ± 0.028
7.631	0.132	0.12 ± 0.01
7.646	0.132	0.16 ± 0.02

Table 6-6. The weight fractions of K, Th, Fe and Si for each γ -ray peak of interest input into the model and the estimated weight fraction of each element based on the output of the model and the results shown in Table 6-5.

6.7 Discussion

Figure 6-9 shows that the experimental to modelled count rate ratios for each Martian surface grid are in within 20 % of one other. One of the disadvantages of the method of

verification detailed in Chapter 5, was that the model could not be verified for γ -rays up to 10 MeV. In this chapter, the model has been verified up to 7.7 MeV.

It has been shown here that there is up to a 20 % discrepancy between the 2001 Mars Odyssey data and the model, but the discrepancy can be attributed to several differences between the model and experiment. For example, an average GCR spectrum was used. The GCR spectrum varies with solar activity; at solar maximum the GCR flux at Mars is at minimum because the interplanetary magnetic field associated with solar maximum attenuates the GCR flux to a greater degree than at solar minimum. A slightly lower GCR flux at solar maximum would cause the model to overestimate the resultant γ -ray emissions from the planet, causing the experimental to modelled ratio to be less than 1. Since there are no high energy particle monitors around Mars an estimate of the average GCR flux had to be made and the variability could not be accounted for.

In the model it was assumed that the atmospheric thickness and composition remained constant in each grid throughout the mission; however, this is not the case in reality (there are seasonal, diurnal and meteorological variations) and Kerry et al. (2002) state that the atmospheric attenuation reduces the field of view of the detector by several degrees depending on the atmospheric conditions. It was also assumed in each grid that the topography was uniform; this is not the case in reality. If the atmosphere is thicker or the topography lower than that modelled, then this would cause the model to overestimate the count rate in orbit and the ratio will be less than 1. A mean orbital altitude was used (411 km) in the model; however, the orbit of the 2001 Mars Odyssey spacecraft is slightly elliptical. A higher orbital altitude than that modelled would cause the experimental to

modelled ratio to be less than 1. The angle that the detector made with the Martian surface was not taken into account, i.e. some of the spacecraft structure may have modified the flux detected by the detector by physically obstructing the detector view of the surface; any structure obscuring the surface that was not modelled would also cause the ratio to be less than 1. Although these factors may affect the results obtained by the orbital 2001 Mars Odyssey γ -ray spectrometer, an in-situ instrument would not be as affected by changes in the atmosphere and topography. Since the geophysical package is expected to remain stationary with all the detector surface areas exposed to the γ -ray emission, for the purposes of this work these factors were not modelled.

The model was verified for atmospheric-less planetary bodies by altering the Martian model to reflect a lunar composition and by removing the atmosphere. The count rates were then compared to the Martian model data. An estimate of the concentration of K, Th, Si and Fe was made based on the comparison between the Martian and lunar models. Table 6-6 shows how those derived compositions compare to the compositions input into the model. The modelled estimated weight fractions for Si, K and Th were within 20 % of the weight fractions input into the model. Fe had two lines of interest that gave one higher and one lower weight fraction than the model input concentration. However, if the average values are taken, the average weight fraction is within error of the model input concentration (e.g. the Fe line at 7.646 MeV gave a concentration of 16 % while the line at 7.632 MeV gave a concentration of 12 %. Taking an average of the two estimates gives $(14 \pm 2)\%$, this is within error of the actual value of 13.2 %).

The modelling has highlighted the need to have accurate knowledge of the particle environment that induces the γ -ray emissions from a planetary surface. A neutron source with a known spectrum could reduce the uncertainty in the relative contributions of the planetary surface and in-situ platform to the γ -ray spectra collected. This would increase the accuracy of the composition estimates derived from the spectra. Combined RTG power and neutron sources are being studied at the University of Leicester and will be discussed in future publications.

6.8 Conclusion

A Monte Carlo model of the Martian radiation environment has been developed. It was verified using data from the γ -ray spectrometer on 2001 Mars Odyssey to compare it to ‘ground truth’ data from the surface of Mars and to evaluate its performance when modelling a detector with a known response function. Three different regions of the Martian surface were modelled and the modelled count rates for Si, H, Cl, Fe, Th and K were compared with the count rates obtained by the spectrometer. The model count rates were comparable with the experimental data. The model was then altered to reflect a lunar surface to check the model was working. The composition derived from the model was found to be within error of the composition input into the model, therefore the model was deemed to be working. The verified model can be adapted to any surface of a planetary body and has been used to determine the performance of geophysical instrumentation being developed at the University of Leicester (Chapter 8).

Chapter 7

γ -ray Spectroscopy in Mars Orbit During Solar Proton Events

7.1 Introduction

GRS can be used to determine the composition of planetary surfaces, but it has yet to be successfully carried out in-situ. This work describes some of the results obtained from the γ -ray spectrometer on 2001 Mars Odyssey during SPEs and discusses whether the increased γ -ray emissions induced from a planetary surface due to the SCR proton interactions are useful in GRS. The chapter shows that although increased γ -ray emissions were expected from the Martian surface during a SPE, they were not detected from orbit probably due to insufficient signal to background; however, this does not preclude the possibility of measuring changes in flux correlated with changes in solar activity on the surface of the planet.

7.2 SPEs

Chapter 2, Section 2.2 detailed how SCR and GCR protons interact with a planetary surface to generate γ -ray emission. A SPE refers to an enhancement in solar proton emissions from the Sun, but generally speaking these events include heavy ions, which form a similar proportion of the total number of emitted particles as the heavy ions in the GCR particle distribution (Morthekai et al., 2007). SCR protons dominate the spectrum and are the type

of particles that are accelerated to high energies (> 1 MeV) by shocks associated with coronal mass ejections (CMEs), magnetospheric bow shocks, and co-rotating interaction regions (Reames, 1999a). The mechanism that generates the most intense events is the CME, which is the result of magnetic energy being released from reconnecting coronal fields. This process can cause the acceleration of protons to energies > 100 MeV, even reaching energies of several GeV. These energies are reached via collision-less shock waves that are driven out from the solar corona. CMEs can occur (on average) 2.5 times a day at solar maximum; however, only about 1-2 % of these actually form shocks (Reames, 1999a). Proton acceleration occurs when protons are scattered back and forth across the shock many times by magnetic turbulence upstream and downstream from the shock. Reames (1999a) provides a more detailed explanation of the acceleration mechanisms.

The protons accelerated by the shock can stream outwards from it, and tend to follow the magnetic field lines that make up the IMF (Cleghorn et al., 2004). Protons of 10 MeV can have speeds up to 1 AU/hour (Reames, 1999b); higher energy protons travel faster, therefore the onset of the CME can be detected very quickly via radiation monitors in orbit about the Earth. The shock wave itself also travels outwards from the Sun at speeds of 750 kms^{-1} to 2500 kms^{-1} (Reames, 1999b). Protons within the shocks generate resonant waves that ‘trap’ other protons in the shock’s path; these are accelerated in the same way as the protons within the shocks. These shocks can spread over a wide angular range, reaching 180° width at 1 AU (Cane, 1988). The peak flux of energetic protons is usually observed when the shock wave passes (Reames, 1999a), even for protons at energies of > 500 MeV. If a planet is well connected to the CME via one of the IMF lines, then an observer at 1 AU could see a sharp rise in particle flux (associated with the SPE) approximately 12 hours

after the onset of the event (Futaana et al., 2008). If the planet is not well connected to the CME then the particle flux will increase more gradually, or not at all. The location of the CME emission point on the Sun, the width of the shock wave and the speed of the shock all determine whether the SPE could affect the planet or not.

SCR protons have higher energies than solar wind protons, therefore they have larger interaction lengths so they can penetrate further into a planetary atmosphere or surface before interacting with it (See Chapter 2). In the case of Mars, if the particles were able to reach the denser surface material of the planet, the probability of a nuclear reaction occurring would increase, therefore more secondary particles would be produced than in any interaction with the Martian atmosphere. This should result in an increase in γ -ray emission from the planetary surface. The increase in γ -ray emission would result in increased signal to background and will positively impact the counting statistics. Improved counting statistics would be of great benefit to a lander-based γ -ray spectrometer. Often lander-based instruments have to share limited resources with other instruments thus reducing data acquisition times.

Studying the effects of a SPE on a planetary surface is of great interest, not only for the purposes of planetary composition studies, but also in understanding the radiation hazard astronauts could face on the surfaces of other planets. The Earth's atmosphere is sufficient to protect us from the energetic particles released in a SPE, but the Martian atmosphere is not, and there would be no protection at all on the lunar surface. Models of the Martian surface radiation environment have been developed in order to study the dose rate that astronauts would be exposed to during quiet solar conditions and during SPEs. Morthekai

et al. (2007) modelled the dose rate with depth in the Martian regolith using GEANT-4 and compared it to the estimated dose rate at the surface determined by the Martian Radiation Environment Experiment (MARIE) on 2001 Mars Odyssey that ceased functioning in 2003. They determined that GCR and SCR protons are only slightly attenuated in the Martian atmosphere; most are deposited in the regolith. From balloon experiments carried out in the upper atmosphere on Earth, we know that the secondary particle production (including neutrons and γ -rays) as a result of the nuclear interaction of protons with planetary material reaches a maximum at approximately 50 g cm^{-2} (Morthekai et al., 2007). Given that the Martian atmospheric thickness is approximately 16 g cm^{-2} (Morthekai et al., 2007), this maximum would occur within the Martian regolith. This is in agreement with the Monte Carlo model described in Chapters 5 and 6. Figure 7-1 shows results from the Monte Carlo model, which shows the flux of neutrons and γ -rays as a function of depth in the Martian surface. The Figure demonstrates that the secondary particle flux of protons at energies $> 500 \text{ MeV}$ reaches a maximum at tens of centimetres beneath the surface.

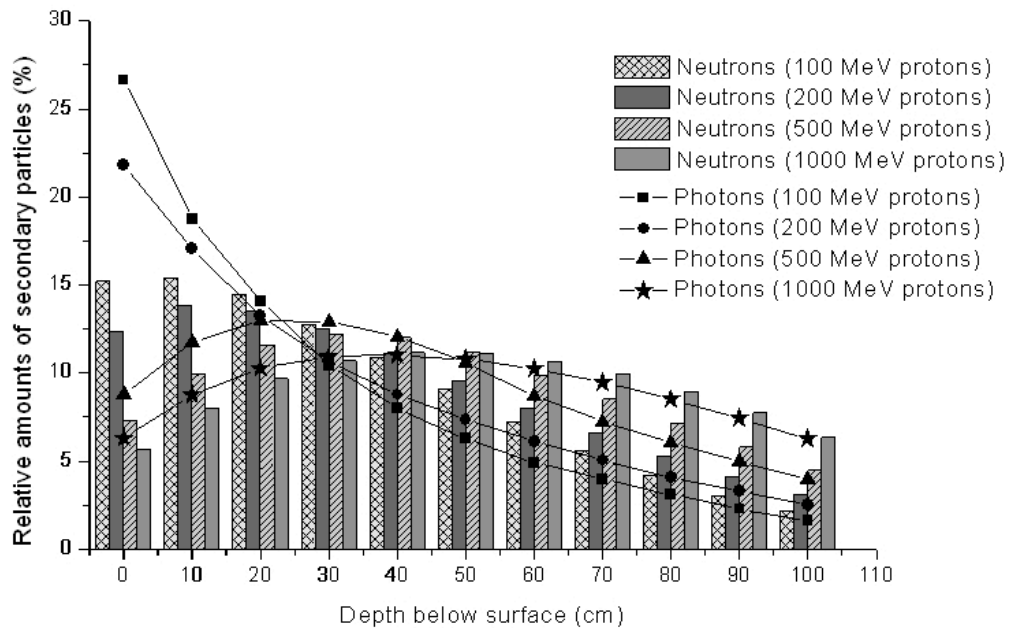


Figure 7-1. Relative amounts (%) of secondary particles in the MCNPX simulated Martian surface. The plot indicates where the number of secondary particles reaches a maximum for protons of different energies. The energy stated in the brackets in the legend next to the particle type indicates the energy of protons that were interacting with the simulated surface. For protons of > 500 MeV, the number of secondary particles appears to reach a maximum within the Martian regolith.

7.3 Detection of SPEs at the Earth and Mars

There has been a documented correspondence between SPEs detected at the Earth by the Space Environment Monitors (SEM) on the Geostationary Operational Environmental Satellites (GOES) and at Mars by MARIE. The SEM on the GOES satellites, measures the effect of the Sun on the near-Earth environment from a geostationary orbit. The SEM includes two instruments capable of measuring energetic protons: the energetic particle sensor (EPS) and the high-energy proton and alpha particle detector (HEPAD); capable of detecting protons in the energy range 0.8 - 500 MeV and 350 – 700 MeV respectively. The GOES satellites and the SEM are detailed fully in the GOES databook (Space Systems

Loral, 1996). Cleghorn et al. (2004) reported six SPEs between March and mid-September 2002 that were detected by both spacecraft; however, the location of the two planets in relation to the CME meant that the spacecraft observed different effects. For example, in the 16th to the 18th March 2002 SPE, GOES-8 experienced a small enhancement of the high energy proton flux; whereas MARIE showed that the Martian environment experienced a sharp rise in energetic proton levels (Cleghorn et al., 2004). The small enhancement is consistent with > 10 MeV particles diffusing across IMF lines, whereas Mars was well connected to a flux tube originating at the point of the CME. In the events that occurred on the 23rd April, it was MARIE that observed a gradual enhancement and the GOES spacecraft that observed the sharp rise. Cleghorn et al. concluded that increases in particle flux could be detected at both planets during a SPE, depending on how well the planets were connected to the CME and the associated shock wave. Futaana et al. (2008) studied the SPE that occurred in December 2006 using instruments on Mars Express in Mars orbit, Venus Express in Venus orbit and the GOES spacecraft in Earth orbit. The Venus Express and Mars Express Analyser of Space Plasmas and Energetic Atoms (ASPERA) instruments (See Futanna et al., 2008 for a more detailed description of the instrument) observed a large enhancement in the background count levels in December 2006 at their respective locations, the timing of the enhancement was consistent with the time it would take for the energetic particles to reach Venus and Mars if they travelled along the field lines of the interplanetary magnetic field. Evidently some SPEs can be detected at multiple locations in the solar system, depending on how well they are connected to the CME event.

7.3.1 SPE Effects on the 2001 Mars Odyssey γ -ray Spectrometer

Evans et al. (2003) reported that a SPE causes increases in the γ -ray and background count rates and can lead to the distortion of a γ -ray spectrum collected by 2001 Mars Odyssey. The increase in background dominated the signal reducing the ability to identify any spectral lines in the data. In some cases the flux levels saturated the system and the detector dead time rose significantly. During the largest SPEs the 2001 Mars Odyssey γ -ray spectrometer is switched off due to pile up and leakage current increases induced by high ion and γ -ray fluxes (Evans et al., 2003). This implies that the data during large SPEs, such as the July 2002 and November 2003 events were not collected. The data for these time periods are not available on the NASA PDS Geosciences node. However, data was collected during SPEs that did not disable the γ -ray spectrometer (therefore it can be assumed that pile up effects and leakage current increases were not significant) and did not have a negative impact on the γ -ray data. Lawrence et al. (2004) demonstrated that the lunar spectra from the Lunar Prospector γ -ray spectrometer increased during a moderate SPE, then decreased to normal levels over a period of several days; however, it was not conclusive about whether the increased γ -ray emission originated from the planet or the spacecraft. Lawrence et al. also suggested that using these enhanced peaks in the spectra to determine the elemental composition of the surface could provide additional information about the Moon, but no further discussion on this topic followed. This study builds on from the work carried out by Lawrence et al. (2004), by exploring data 2001 Mars Odyssey collected during SPEs to ascertain if any useful information may be inferred from it.

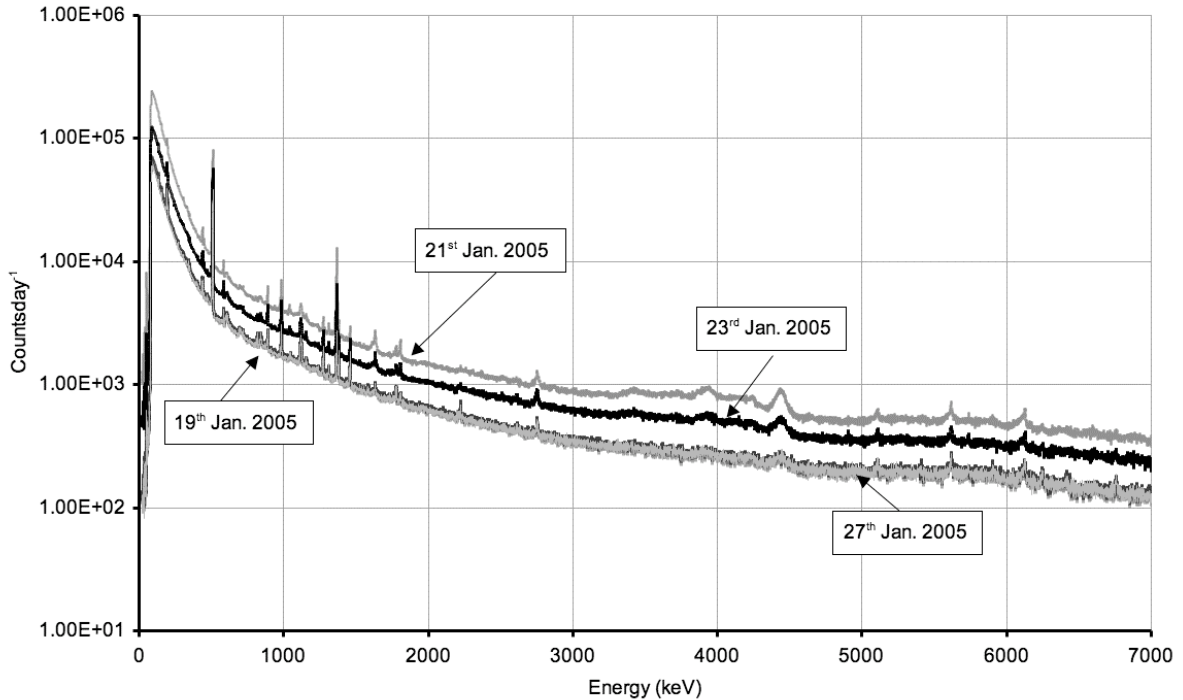


Figure 7-2. γ -ray spectra from the 2001 Mars Odyssey γ -ray spectrometer collected over a SPE that occurred in January 2005. Data taken from the NASA PDS Geosciences node (Boynton, 2002).

Figure 7-2 gives an example of the 2001 Mars Odyssey γ -ray spectrometer spectra taken over a SPE that occurred in January 2005, which was also detected by the GOES spacecraft in orbit around the Earth. The spectra increased sharply in intensity then took several days to return to the original background levels. According to Evans et al., (2007) changes in the γ -ray spectrum caused by the solar event of July 2002 resulted in a distortion and broadening of the elemental peaks. The aim of the Evans work was to generate summed and averaged peak intensities for each spectral element over a period of 650 days; the inclusion of the data associated with the SPE would have introduced errors in the estimated concentration of elements on the Martian surface. For this reason all data collected over SPEs were excluded from the published spectra.

7.4 SPE Data

The globally summed γ -ray spectra collected by the γ -ray spectrometer on 2001 Mars Odyssey were analysed to investigate how a SPE affects the γ -ray peaks of specific elements in the spectra. Data on the solar proton fluence was obtained from the GOES satellite data node (NGDC, 2008). The data collected indicated that SPE events occurred during the primary 2001 Mars Odyssey mission (2002 to 2006).

7.4.1 SPE Data for 2001 Mars Odyssey γ -ray Spectrometer

As mentioned above, a SPE detected at the Earth does not always affect the Martian radiation environment. Since the malfunction of MARIE in 2003, there have been no operational high energy particle monitors in orbit around Mars to better study the effects of SPEs on the planet. A solution was to examine HEND data, and the γ -ray background levels of the γ -ray spectrometer spectra. The HEND on-board 2001 Mars Odyssey is sensitive to high-energy protons, as well as fast and epithermal neutrons (however, there is no way to distinguish between the signals generated by the two particles). The HEND can be used as an indicator of when there is increased particle flux at Mars, i.e. when the SPE protons have reached Mars orbit. The γ -ray background in the γ -ray spectrometer spectra also increased, indicating that high-energy protons were interacting with the spacecraft and planet, generating γ -rays. The continuum was measured at two energies that did not appear to have any lines of planetary or spacecraft origin; 1.070 MeV and 7.196 MeV. These two indicators, combined with the data from GOES were used to determine whether a SPE had occurred and whether it had reached Mars.

Figure 7-3 shows the proton fluence measured by the SEM on GOES over 2005. Two high-energy events were identified in January and September. Figure 7-4 shows the proton fluence as detected by the SEM on GOES, and the particle flux detected by the fast neutron detector on the HEND and the γ -ray continuum when the Earth and Mars were in near opposition (January 2005). Figure 7-5 shows the same variables for when the Earth and Mars were closely aligned (August-September 2005). It was concluded that all three instruments detected SCR protons or their secondaries, therefore the two planets could have been well connected to the CME. Unfortunately this does limit the usefulness of the data, since we are reliant on a SPE affecting both the Earth and Mars systems in order to verify that the increases in the HEND particle flux and γ -ray background in the γ -ray spectrometer are due to SCR protons reaching Mars.

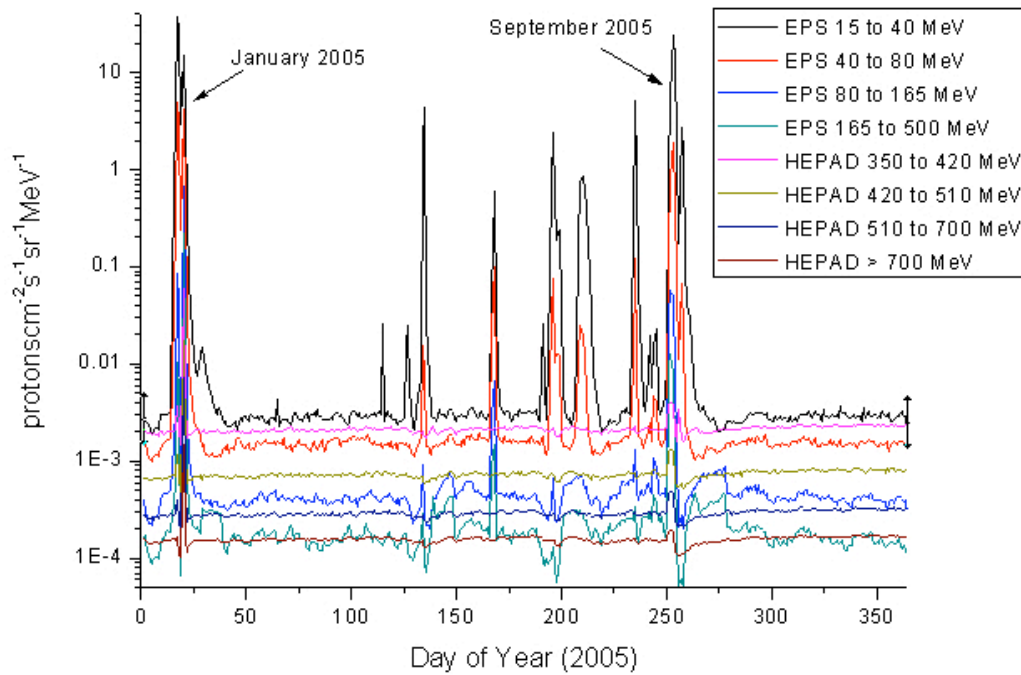


Figure 7-3. EPS (15 MeV to 80 MeV) and HEPAD (320 MeV to > 700 MeV) data from GOES-11 for 2005 (Corrected proton channel data from GOES-11). Data taken from NGDC (2008).

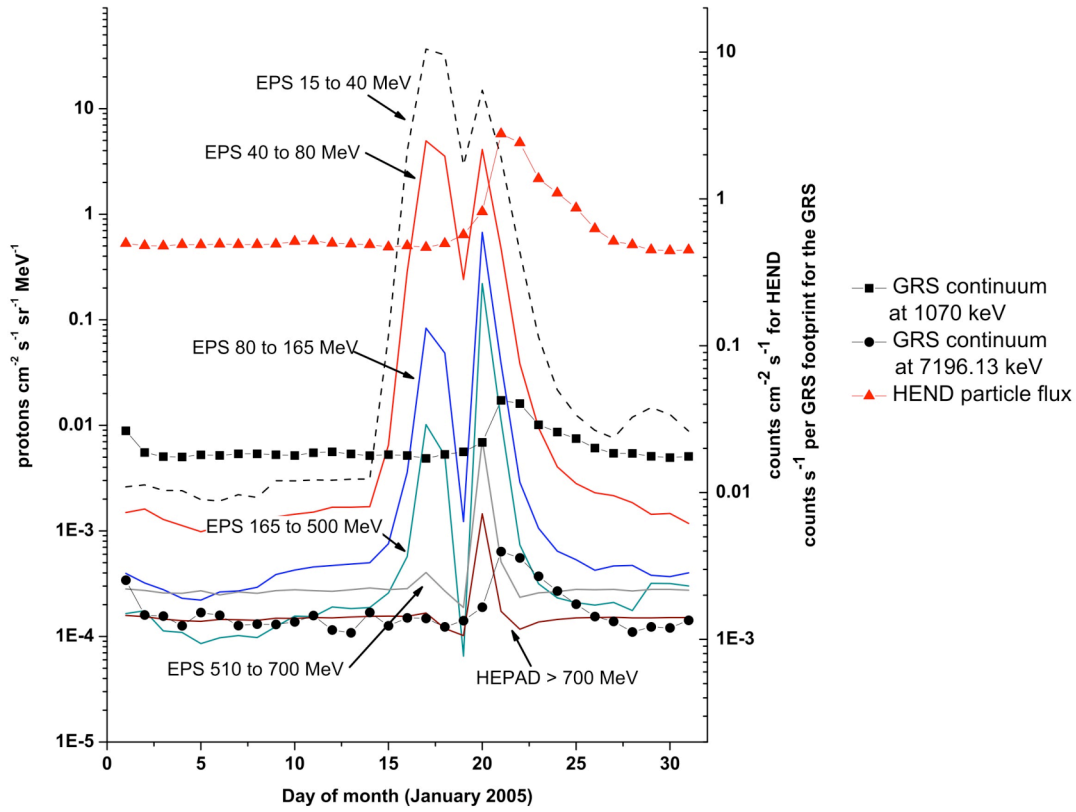


Figure 7-4. The EPS and HEPAD measured proton fluence from GOES-11 in orbit of the Earth, the HEND particle flux and the γ -ray spectrometer continuum count rate at 1.070 MeV and 7.196 MeV from 2001 Mars Odyssey in the orbit of Mars in January 2005. It shows increases in proton flux across the energy range 15 MeV to 700 MeV during the SPE. Data taken from NDGC (2008); Boynton (2002); Boynton (2004).

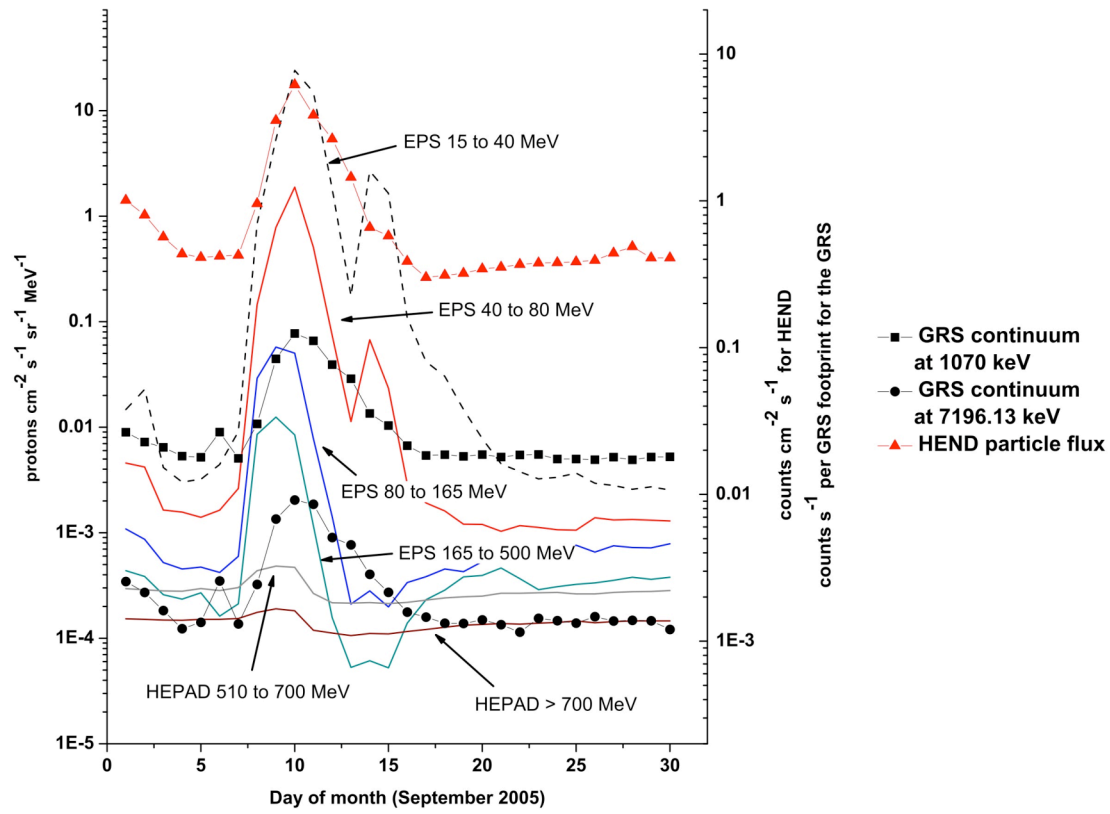


Figure 7-5. The EPS and HEPAD measured proton fluence from GOES-11 in orbit of the Earth, the HEND particle flux and the γ -ray spectrometer continuum count rate at 1.070 MeV and 7.196 MeV from 2001 Mars Odyssey in the orbit of Mars in September 2005. It shows increases in proton flux across the energy range 15 MeV to 700 MeV during the SPE. Data taken from NDGC (2008); Boynton (2002); Boynton (2004).

7.5 γ -ray Data Analysis

The corrected γ -ray spectra data from the 2001 Mars Odyssey γ -ray spectrometer and the HEND data were obtained from the NASA PDS Geosciences node (Boynton, 2002). The γ -ray spectra for the SPEs and their decay phases in January and September 2005 were

co-added to produce a single spectrum with enough counts in it to ensure that uncertainties in the peaks were lower than 10 %. The spectral analysis was carried out using the same techniques as those described in Chapter 6, Section 6.2.

7.6 Results

Table 7-1 shows the peak count rates extracted from the 2001 Mars Odyssey γ -ray spectrometer data. In order to compare the 2001 Mars Odyssey γ -ray spectrometer count rates in Table 7-1 to normal solar condition data, readers are directed to Table 1 in Evans et al. (2007).

Energy (MeV)	Possible source/s	Reference energy (MeV) [1]	SPE spectra		
			counts/min	Uncertainty (%)	FWHM (keV)
0.808	$^{70}\text{Ge} (n, \gamma) / ^{73}\text{Ge} (n, \gamma)$	0.808	0.78	0.9	5.719
0.835	^{54}Mn	0.835	1.454	0.7	6.825
0.841	^{54}Mn	0.840	1.467	0.7	4.77
0.846	$^{56}\text{Fe}^*$	0.846	1.121	0.8	5.539
0.872	$^{69}\text{Ge} \text{ EC}$	0.873	0.366	1.3	5.702
0.882	$^{69}\text{Ge} \text{ EC}$	0.882	2.72	0.5	8.219
0.936	$^{52}\text{Cr}^* / ^{52}\text{Mn}$	0.935	0.94	0.8	
0.983	$^{48}\text{Ti}^* / ^{48}\text{V}$	0.983	7.737	0.3	4.547
0.992	$^{64}\text{Zn}^*$	0.991	2.25	0.5	4.98
1.014	$^{27}\text{Al}^*$	1.014	0.333	1.4	5.295
1.021	$^{10}\text{C} / 511 \text{ keV SUM}$	1.021	0.424	1.2	6.111
1.039	$^{48}\text{Sc} / ^{70}\text{Ge}$	1.039	1.769	0.6	6.05
1.049	$^{66}\text{Ga} \text{ EC}$	1.048	1.208	0.7	6.434
1.077	$^{68}\text{Zn}^*$	1.077	0.305	1.4	5.712
1.091	$^{70}\text{Ge} (n, \gamma)$	1.095	0.251	1.6	8.122
1.108	$^{69}\text{Ge} \text{ EC}$	1.108	0.43	1.2	4.521

1.129	$^{26}\text{Mg}^*$	1.129	1.355	0.7	11.775
1.147	$^{47}\text{Sc}^*$	1.147	0.456	1.2	5.577
1.157	$^{44}\text{Sc}/^{44}\text{Ca}^*$	1.157	1.754	0.6	6.335
1.204	$^{73}\text{Ge} (n, \gamma)$	1.204	0.268	1.5	5.136
1.237	$^{56}\text{Fe}^*/^{214}\text{Bi}$	1.238	0.877	0.8	9.419
1.285	$^{47}\text{Ti}^*$	1.284	0.512	1.1	4.71
1.312	$^{48}\text{Ti}^*/^{48}\text{V}$	1.312	2.354	0.5	7.024
1.333	^{60}Co	1.332	1.07	0.8	7.702
1.346	$^{69}\text{Ge} \text{ EC}$	1.347	0.82	0.9	7.154
1.368	$^{24}\text{Mg}^*$	1.368	20.513	0.2	9.547
1.410	$^{54}\text{Fe}^*/^{55}\text{Fe}^*$	1.408/ 1.408	0.946	0.8	8.242
1.454	$^{58}\text{Ni}^*$	1.454	0.659	1	6.149
1.525	$^{40}\text{Ca}^*$	1.524	0.754	0.9	8.858
1.553	$^{50}\text{Ti}^*$	1.553	0.456	1.2	8.505
1.611	$^{56}\text{Fe} (n, \gamma)$	1.612	4.185	0.4	29.082
1.634	$^{20}\text{Ne}^*/^{20}\text{F}$	1.633	1.861	0.6	13.657
1.723	$^{48}\text{Ti} (n, \gamma) \text{ SUM}$	1.723	0.271	1.5	8.418
1.727	$^{56}\text{Fe} (n, \gamma)$	1.725	0.494	1.1	17.683
1.794	$^{48}\text{Ti} (n, \gamma)$	1.793	0.295	1.5	9.611
1.808	$^{26}\text{Mg}^*$	1.808	2.599	0.5	11.951
1.810	$^{56}\text{Fe}^*$	1.810	0.78	0.9	10.165
1.824	$^{48}\text{V} + 511 \text{ keV}$	1.823	0.205	1.8	5.063
1.982	$^{18}\text{O}^*$	1.982	1.207	0.7	30.162
2.009	$^{46}\text{Ti}^* \text{ SUM}$	2.009	0.985	0.8	22.522
2.028	$^{29}\text{Si}^*$	2.028	1.324	0.7	33.203
2.108	^{56}Fe	2.112	1.141	0.7	65.339
2.211	^{27}Al	2.211	0.482	1.1	17.661
2.295	$^{48}\text{Ti}^* \text{ SUM}$	2.295	0.265	1.5	11.939
2.300	$^{48}\text{V} \text{ SUM EC}$	2.300	0.184	1.9	5.503
2.312	^{14}O	2.312	0.339	1.4	7.762
2.376	$^{48}\text{Ti}^*$	2.375	0.988	0.8	17.686
2.517	$^{28}\text{Si} (n, \gamma) \text{ DE}$	2.517	2.265	0.5	38.151
2.599	$^{56}\text{Fe}^*$	2.600	0.632	1	18.373
2.638	$^{48}\text{Ti} (n, \gamma)$	2.635	2.984	0.5	41.734

2.719	$^{56}\text{Fe} (n, \gamma)$	2.721	0.282	1.5	14.819
2.750	^{16}O	2.741	3.719	0.4	37.525
2.867	$^{24}\text{Mg} *$	2.869	0.535	1.1	21.193
3.222	$^{48}\text{Ti} (n, \gamma) \text{ SE}$	3.222	0.244	1.6	25.918
3.370		3.369	0.929	0.8	53.3
3.410	$^{56}\text{Fe} (n, \gamma)$	3.413	1.211	0.7	3
3.437	$^{56}\text{Fe} (n, \gamma)$	3.436	2.024	0.6	57.767
3.475	$^{48}\text{Ti} (n, \gamma)$	3.475	3.993	0.4	89.495
3.539	$^{28}\text{Si} (n, \gamma)$	3.539	0.762	0.9	38.855
3.735	$^{48}\text{Ti} (n, \gamma) / ^{40}\text{Ca} *$	3.733/ 3.736	0.39	1.3	23.417
3.863	$^{48}\text{Ti} (n, \gamma) \text{ DE}$	3.859	0.346	1.4	21.717
3.934	$^{12}\text{C} * \text{ SE}$	3.927	3.125	0.4	72.299
4.218	$^{56}\text{Fe} (n, \gamma)$	4.218	0.408	1.2	23.215
4.247	$^{16}\text{O} \text{ NE DE}$	4.247	0.791	0.9	28.69
4.433	$^{12}\text{C} *$	4.438	8.388	0.3	77.595
5.089		5.088	0.72	0.9	47.019
5.107	$^{16}\text{O} \text{ DE}$	5.106	0.607	1	13.639
5.239	$^{15}\text{O} *$	5.239	0.438	1.2	34.734
5.268	$^{16}\text{O} \text{ NE}$	5.269	0.681	1	30.149
5.619	$^{16}\text{O} * \text{ SE}$	5.617	1.985	0.6	17.513
5.629	^{16}O	5.617	1.966	0.6	90.382
5.868	$^{28}\text{Si} (n, \gamma) \text{ SE}$	5.868	0.945	0.8	96.982
5.906	$^{48}\text{Ti} (n, \gamma) \text{ SE}$	5.907	0.382	1.3	23.77
6.127	^{16}O	6.128	3.638	0.4	34.644
6.139	^{16}O	6.128	1.653	0.6	116.765
6.365	$^{28}\text{Si} \text{ SE}$	6.366	0.435	1.2	61.102
6.421	$^{48}\text{Ti} (n, \gamma)$	6.418	0.974	0.8	37.743
6.611	$^{16}\text{O} \text{ SE}$	6.604	0.77	0.9	81.312
6.874	^{28}Si	6.877	0.19	1.8	41.892
6.901		6.903	0.489	1.1	62.615
6.927	^{16}O	6.915	0.506	1.1	100.502
7.117	$^{56}\text{Fe} (n, \gamma) \text{ SE}$	7.120	1.188	0.7	73.431
7.131	^{16}O	7.115	0.386	1.3	37.913

Table 7-1. 2001 Mars Odyssey γ -ray spectrometer peak data analysis results for the summed SPE data over 2005. The reference energies [1] were obtained from Evans et al. (2007). Key: The reactions that take place for the γ -rays to be created in the list above are inelastic scatter reactions (n,n γ) unless stated otherwise; (n, γ) = neutron capture; NE = non-elastic reaction; * = multiple reactions to create the γ -ray; EC = γ -ray created as a result of electron capture.

The γ -ray lines included in the tables are those that have an uncertainty of less than 10 % and have statistically significant increases compared to the normal solar condition data (the data was considered significant if the count rate increase was greater than a 3-sigma limit to the normal solar condition data). The uncertainty was set at this level to ensure that the peaks were easily distinguishable against the increased background and that they could be fitted accurately.

7.7 Discussion

When comparing the results of this study to Table 1 in Evans et al. (2007), two aspects are clear:

- Many of the lines believed to be of planetary origin (such as many of the Cl lines) could not be identified in the SPE data. The majority of lines that could be positively identified and were statistically significant were ones that are suspected to have a significant contribution from the spacecraft itself (such as Fe, Mg, Ti, Ge, Si, Al, C, O, Zn, F, K, V, Cr, Ca and other elements produced as a result of activation of the spacecraft by the high energy particle interactions, e.g. the $^{48}\text{Ti}(p,n)^{48}\text{V}$ or the $^{48}\text{Ti}(n,p)^{48}\text{Sc}$ reaction), or the atmosphere (C and O).
- The identified lines often became broader or suffered from low energy tailing as a result of the SPE, this is evident from the larger FWHM of the peaks.

The lines of both planetary and spacecraft origin that were ‘lost’ in the SPE spectra were often close to a line that underwent a strong enhancement/ broadening as a result of the SPE, making that line unidentifiable. It is suspected that the weaker lines could have been ‘swamped’ by the increased γ -ray background from the spacecraft.

The conclusion of this study is that it cannot be confirmed that any of the γ -ray peaks identified in the SPE spectra originated from the surface of Mars. A few S and Cl lines were identified in the spectra at 3.370 MeV (S), 5.089 MeV (Cl) and 6.901 MeV (Cl) and are highlighted in Table 7-1. However, it is suspected that the peak increases were due to other sources other than these planetary elements, because other S and Cl peaks could not be identified in the rest of the spectra. The two Cl peaks are escape peaks, but the full photopeak could not be identified in the spectra, agreeing with the theory that these peaks must be due to other sources. The alternative sources could be $^{48}\text{Ti}(n,\gamma)$ or $^{56}\text{Fe}(n,\gamma)$ for the 3.370 MeV line, $^{52}\text{Cr}(p,\gamma)$ for the 5.089 MeV line, $^{52}\text{Cr}(p,\gamma)$ for the 6901.3 keV line.

7.8 Conclusion

This study has shown that there is a correspondence between the proton fluence emitted from the Sun and the γ -ray emission detected in Mars orbit, but it is inconclusive whether this causes increased γ -ray emission from the planet and whether it may be of use in an in-situ GRS mission. The elemental peaks detected by the 2001 Mars Odyssey γ -ray spectrometer can all be attributed to elements that are present on the 2001 Mars Odyssey spacecraft. From this study it is clear that for a future in-situ GRS mission it would be

essential to minimise the elements present on the in-situ lander/ probe to avoid interferences with planetary lines and to fully characterise the contribution of the lander/ probe to the γ -ray spectrum collected.

Chapter 8

Neutron Sources for In-situ Planetary Science Missions

8.1 Introduction

This chapter describes the modelling of a geophysical package with the Monte Carlo code MCNPX to determine the impact that a neutron source would have on in-situ composition measurements, radiometric dating and in particular trace element detection. The suitability of \varnothing 2.54 x 2.54 cm LaBr₃(Ce) detectors in the geophysical package for in-situ missions was examined. ²⁵²Cf, Am-Be or Pu-Be neutron sources were compared in a trade-off study to determine mission suitability, potential for thermal and electric power production, mass and shielding requirements. This study was linked to a parallel examination of the suitability of radioisotope thermal generators (RTGs) for in-situ planetary science applications. The aim of the modelling was to optimise the source type and detector geometry in order to measure the elemental peaks of interest with a precision of 1 % for major elements or 10 % for trace elements, based on the Poisson statistics of the detected counts above background.

8.2 The Geophysical Instrument: Neutron Sources

The geophysical package was modelled by using the verified GCR interaction model described in Chapter 6. The aim was to determine whether the γ -ray emissions generated by the SCR and GCR interactions with a planetary surface produced count rates that were statistically significant to detect the peaks associated with the major rock forming elements over a timescale of 1 year. Table 8-1 shows the time periods required for the geophysical package (at a depth of 2m) to obtain a 1 % precision on some of the elemental peaks of interest. The geophysical package would require years to get a 1 % precision on these peaks if relying on GCR-induced emissions alone (the GCR flux is only $\sim 4 \text{ cm}^{-2} \text{ s}^{-1}$). Therefore, while GRS using GCR and SCR induced γ -ray emissions is suitable for orbital measurements where counts are being collected over a large areas (km^2), it is not feasible in-situ, where γ -ray collection takes place over areas of m^2 . A SPE only takes place over a matter of days; therefore the increased γ -ray emission associated with a SPE would not be significant compared with the long term GCR-induced emissions. The solution for in-situ GRS is to include a neutron source as part of a geophysical package.

Element	Energy (MeV)	Time to 1 % precision (yrs)
⁴⁸ Ti	1.381	123
⁴⁰ Ca	1.943	1202
³⁵ Cl	1.960	174
¹ H	2.225	77.4
²³ Na	2.754	1467
²⁸ Si	3.540	217
²⁴ Mg	3.916	1845
⁵⁵ Mn	7.243	2046
⁵⁶ Fe	7.643	225
²⁷ Al	7.725	3119

Table 8-1. The estimated time periods required for the geophysical package to get 1 % precision on some elemental lines that are of interest in planetary composition studies. The geophysical package was modelled at 2 m depth in the Martian surface.

A study was carried out at the University of Leicester to investigate the feasibility of using a number of radioisotopes (e.g. ²⁵²Cf) or (α ,n) sources (e.g. Am-Be) for both power generation and as neutron sources (O'Brien et al., 2009). The planetary radiation environment model (See Chapters 5 and 6) was used in this study to examine the performance of a geophysical detector package on a planetary surface similar to that of the Moon and Mars (a silicate-based surface), and one similar to the surface of Europa (a water-based surface). Exploring Europa is a target of the Europa Jupiter System Mission (Joint Jupiter Science Definition Team, 2009). Penetrators could play a role in exploring the surfaces of the Moon and Europa (Joint Jupiter Science Definition Team, 2009).

In the MCNPX model the detectors have the dimensions \varnothing 2.54 x 2.54 cm (12.9 cm³). The model was used to determine whether the total detector volume was suitable to detect

elements of interest to a precision of better than 1 % for major rock-forming elements and 10 % for trace elements over a typical mission lifetime (1 year). The model was also used to examine several neutron sources, see Section 8.3.

8.3 Neutron Sources for In-situ Applications

The small volume of regolith probed by the two 12.9 cm³ detectors of the geophysical package precludes the detection of the major rock-forming elements from GCR- and SCR-induced γ -rays. An in-situ neutron source increases the γ -ray emission from the surface by several orders of magnitude compared with GCR- and SCR-induced γ -ray emissions, reducing the timescales required to get good signal-to-background. In the Martian model the time for the geophysical package to obtain a 10 % precision on the Si peak at 3.540 MeV using a 50 mg ²⁵²Cf source (10^{11} s⁻¹) is of the order of hours.

Types of in-situ neutron sources that could be considered include: spontaneous fission sources (e.g. ²⁵²Cf), deuterium-tritium (D-T) neutron tubes and radioisotopes which decay with α particles packed in a low-Z elemental matrix, such as Am-Be or Pu-Be (Ambrosi et al., 2006) There are several advantages to using a neutron source in GRS, including:

- The reduction of spectral acquisition times by several orders of magnitude.
- The neutron flux and energy spectrum would be known exactly, leading to a more accurate interpretation of the γ -ray data acquired.

A research team at the University of Leicester is working on the development of RTGs (O'Brien et al., 2008) in collaboration with several European partners in the UK, Germany

and France and the Center for Space Nuclear Research at the Idaho National Laboratory in the US. Possible RTG sources could include Am, Pu, Cm in their respective oxide forms such as AmO₂. For the purposes of this study ²⁵²Cf is also considered. Oxides could also be theoretically enriched with 99 % ¹⁸O in order to boost neutron emissions; given that the 5 MeV (α ,n) cross section for ¹⁸O is 0.1 barns as opposed to zero for ¹⁶O but much less than the 500 barns for 5 MeV (α ,n) reactions with Be. A Cm based source could also be considered but these will form part of a future feasibility study. These sources could provide power for the in-situ platform as well as providing a neutron source for GRS. For example, ²⁵²Cf primarily decays via α particle emission (96.91 %), a small percentage (3.09 %) undergoes fission (which provides the neutrons). The half life of the decay is 2.645 years (Martin et al., 1999). This radioisotope is already used in terrestrial PGAA applications as a neutron source and when encapsulated the source can withstand high shocks (Martin et al., 1999). The neutron spectra from ²⁵²Cf, Am-Be, AmO₂ with enriched ¹⁸O and Pu-Be are shown in Figure 8-1.

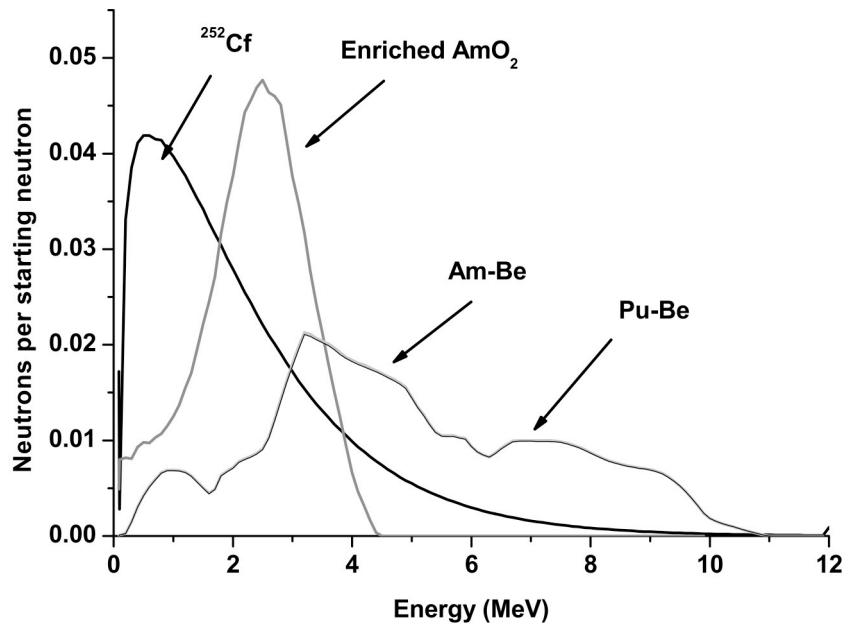


Figure 8-1. Neutron spectra from ^{252}Cf , Am-Be, Pu-Be and enriched AmO_2 sources. Data taken from O'Brien et al. (2009).

The neutron spectra from Am-Be and Pu-Be are very similar; however, the total flux $\text{s}^{-1} \text{g}^{-1}$ is different for the two sources.

8.4 The Physical Model

The planetary radiation environment model described in Chapters 5 and 6 was altered to model the geophysical package as a function of depth (See Figure 8-2 and Figure 8-3). The MCNPX code is shown in Appendix A. Additional elements (Cr, S, Ni, Zn and P) were later added to the composition specified in the model. The concentrations of these elements were based on results obtained by the alpha particle X-ray spectrometer on the Spirit rover, which is measuring the composition of the Martian surface, see Table 8-2 (Gellert et al., 2004).

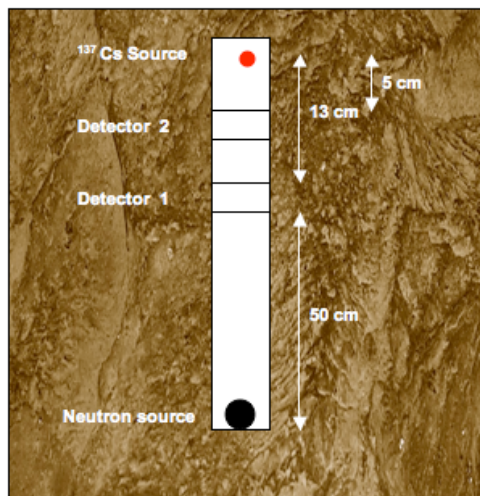


Figure 8-2. The geometry of the geophysical package in the MCNPX model.

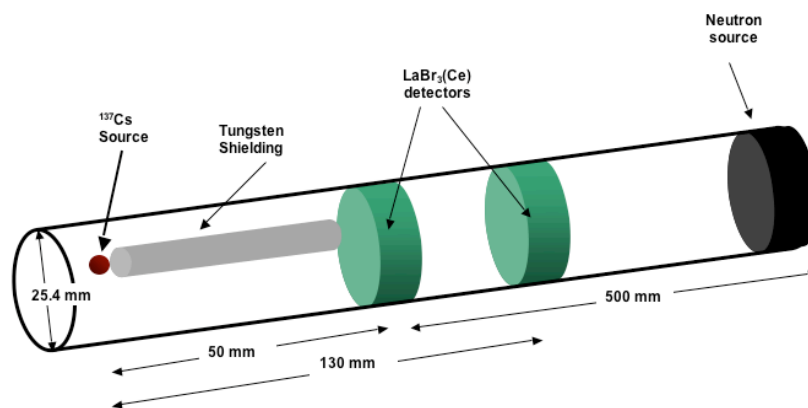


Figure 8-3. The geometry of the geophysical package used in the model.

The two detectors were positioned 8 cm apart and are a maximum of 50 cm from the neutron source. The neutron source will require Cd shielding; for the ^{252}Cf source a thickness of 1.6 cm is required (See Section 8.6.3). The ^{137}Cs source provides the backscattered γ -rays used to determine the bulk density profile.

Additional elements added to radiation environment model	Estimated concentration from the APXS
Cr	0.24 %
Ni	450 ppm
P	0.37 %
S	2.33 %
Zn	300 ppm

Table 8-2. The concentrations of the additional elements added to the radiation environment model for the Martian surface (Gellert et al., 2004).

8.4.1 Neutron and γ -ray Distributions

The neutron sources, described in Section 8.3, were modelled as isotropic point sources and the neutron spectra used in the model are shown in Figure 8-1. For each simulation 10^8 neutrons were transported through the geometry. The model was used to determine the spectrum of γ -rays produced by the various neutron sources as a function of depth to a maximum of 5 m. This chapter reports the results obtained with two \varnothing 2.54 cm x 2.54 cm detectors separated by 8 cm (Ambrosi et al., 2006), when the neutron source is 50 cm (i.e. on a sub-surface probe) and 2 m (i.e. the neutron source positioned on the surface and the detectors on a mole) away from the detectors. For the simulation the detector volumes were specified as voids and the γ -ray counts in the detector volumes per source neutron were measured (See Figure 8-3). Several correction factors were then applied to the results:

- The experimentally verified (Chapter 4) detector response function for $\text{LaBr}_3(\text{Ce})$ was applied to the counts.
- The absorbed γ -ray flux for the two detectors was summed (this was to improve the counting statistics by providing double the detector volume).

- The neutron flux per gram of material for each source and a nominal mission lifetime of one year were used as scaling factors to determine the total detected number of γ -rays (See Table 8-3). The neutron flux of the Am-Be, Pu-Be and enriched AmO₂ sources remains constant with time; however, ²⁵²Cf has a half life of 2.645 year, therefore the flux will decrease over the nominal mission lifetime (Martin et al., 1999). The number of neutrons (N_{total}) emitted by the ²⁵²Cf source over a year was calculated using the integral:

$$N_{total} = A_o \int_0^{1\text{year}} \exp(-\lambda t) dt \quad \text{Equation 8-1}$$

where A_o is the initial activity of the source ($1 \times 10^{11} \text{ s}^{-1}$), t is the time and λ is the decay constant.

Neutron source	Integrated Flux over year (g ⁻¹)	Approximate source mass required for power generation (g)
²⁵² Cf	2.3×10^{12}	0.05
Am-Be	1.4×10^6	2000
Enriched AmO ₂	3.7×10^5	2000
Pu-Be	7.2×10^6	2000

Table 8-3. The total flux emitted by the neutron sources per second integrated over energy and the amount of source mass required to generate 100 W of thermal power. Data taken from O'Brien et al. (2009).

- The mass of ²⁵²Cf, ²⁴¹Am and ²³⁸Pu required for in-situ radioisotope power generation was also used to scale the total detected number of γ -rays detected, see Table 8-3.

The nominal mission duration of one year would require sending data in batches and co-adding the spectra to obtain the required precision for each peak. The precision of each

peak, P , for each element after a year was then calculated with the assumption that at least 1×10^4 counts above background are required for a 1 % precision or better for the major rock-forming elements and 100 counts above background are required for a 10 % or better precision level for the trace elements.

The γ -rays produced by ^{232}Th and ^{40}K decay were included in the simulation using the method described in Chapter 6.

8.4.2 Feasibility of K-Ar Dating with γ -rays

The concentration of ^{40}K is determined via the natural emission of γ -rays at 1.461 MeV. The concentration of ^{40}Ar may be determined via the γ -rays emitted from ^{40}Ar neutron capture (the strongest neutron capture line is at 4.745 MeV). If the γ -ray event statistics from the prompt activation of ^{40}Ar had an uncertainty of 10 % or less, then this K-Ar dating method could be feasible. The ^{40}Ar neutron capture peak with the largest cross section is 4.745 MeV (Révay et al., 2004).

The oldest parts of the Martian surface are 4.5 Gyr old, coinciding with the Noachian epoch (Hahn and McLennan, 2007). The southern hemisphere is where the oldest parts of the surface are found. Assuming that no ^{40}Ar was present on Mars when it formed, the expected concentration of ^{40}Ar that would be present today (excluding the ^{40}Ar in the atmosphere) can be calculated to be approximately 0.6 ppm (See Chapter 2, Section 2.8). For a younger surface of approximately 1.8 Gyr (from the Amazonian epoch (Hahn and McLennan, 2007)), the concentration of ^{40}Ar would be 0.097 ppm. ^{40}Ar was included in the model to determine whether any ^{40}Ar γ -rays could be detected via activation methods. The

^{40}Ar γ -rays created per unit volume of modelled surface was calculated and compared to the detected counts in the $\text{LaBr}_3(\text{Ce})$ detectors over the mission lifetime in order to determine what factors were primarily responsible for determining the feasibility of carrying out such a measurement. Two primary determining factors were considered: the neutron flux and detector geometry, which included the detector volume and location on the Martian surface.

8.4.3 Modelling the Surface of Europa

The model was altered to reflect the composition of the Jovian moon Europa. Zolotov and Shock (2000) estimated the abundance of elements that may be present within the icy surface primarily composed of H_2O . Table 8-4 gives the modelled surface composition. The temperature of the surface was assumed to be ~ 100 K (Swindle et al., 2005).

Element	Concentration (WF)
H	0.076
O	0.60
Cl	0.003
Na	0.00093
Mg	0.00062
S	0.28
Ca	0.00077
K	0.0025
Br	0.00002
C	0.0097
Sr	0.000014
B	4.4×10^{-7}
F	0.000058
Li	7.5×10^{-6}
Rb	0.000011
P	0.014
I	1.8×10^{-6}
Ba	0.000017
Cs	1.2×10^{-6}

Table 8-4. Elements and their abundances in the Europa radiation environment model. Data taken from Zolotov and Shock (2000).

The low concentration of some of the trace elements within the model meant that sufficient counting statistics could not be obtained without simulating a very large number of neutrons, which was not feasible. Instead the concentration of the trace elements was increased to 5 % in each of the simulations. Assuming that there is a linear relationship between detected count rate and concentration, the γ -ray count rates were later scaled to reflect the true concentrations of trace elements. This allowed the minimum detectable

concentration of each element to be calculated. In all cases the correction factors given in Section 8.4.1 were applied.

8.5 Results

Figure 8-4 and Figure 8-5 show the peak precision for the elements on the Martian surface listed at the end of the nominal mission lifetime when the detectors are positioned 50 cm away from the neutron source. Figure 8-6 and Figure 8-7 show the peak precision for the elements listed at the end of the nominal mission lifetime when the detectors are positioned 2 m away from the neutron source.

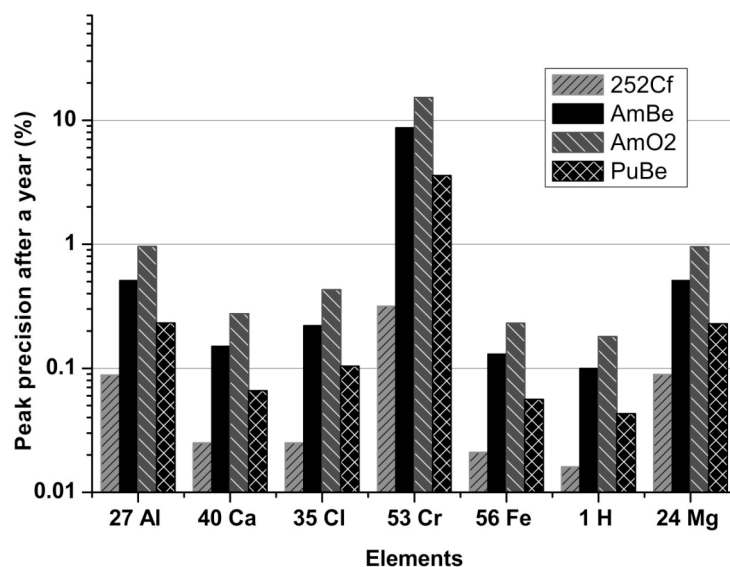


Figure 8-4. The peak precision for the major γ -ray peak of each element on the Martian surface, using the different neutron sources when the detectors are 50 cm away from the neutron source. The γ -ray energies are: ^{27}Al = 7.725 MeV, ^{40}Ca = 1.943 MeV, ^{35}Cl = 1.960 MeV, ^{53}Cr = 0.835 MeV, ^{56}Fe = 7.643 MeV, ^1H = 2.224 MeV, ^{24}Mg = 3.916 MeV (Révay et al., 2004; Firestone, 2003).

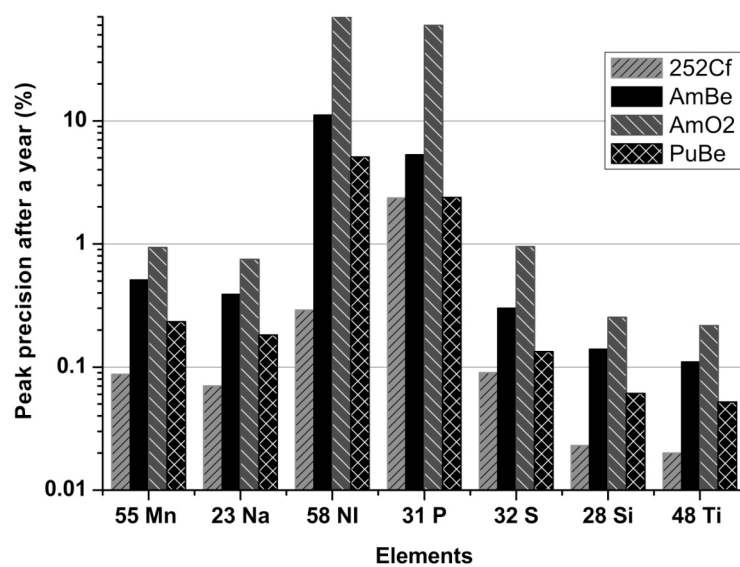


Figure 8-5. The peak precision for the major γ -ray peak of each element on the Martian surface, using the different neutron sources when the detectors are 50 cm away from the neutron source.

The γ -ray energies are: ^{55}Mn = 7.243 MeV, ^{23}Na = 2.754 MeV, ^{58}Ni = 1.455 MeV, ^{31}P = 3.134 MeV, ^{32}S = 2.237 MeV, ^{28}Si = 3.540 MeV, ^{48}Ti = 1.381 MeV (Révay et al., 2004; Firestone, 2003).

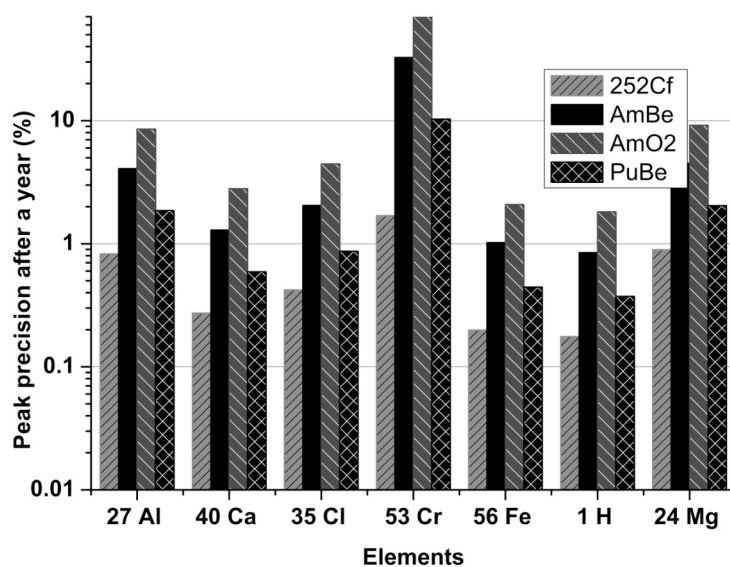


Figure 8-6. The peak precision for the major γ -ray peak of each element on the Martian surface, using the different neutron sources when the detectors are at 2 m depth with the neutron source on the surface.

The γ -ray energies are: ²⁷Al= 7.725 MeV, ⁴⁰Ca= 1.943 MeV, ³⁵Cl= 1.960 MeV, ⁵³Cr= 0.835 MeV, ⁵⁶Fe= 7.643 MeV, ¹H= 2.224 MeV, ²⁴Mg= 3.916 MeV (Révay et al., 2004; Firestone, 2003).

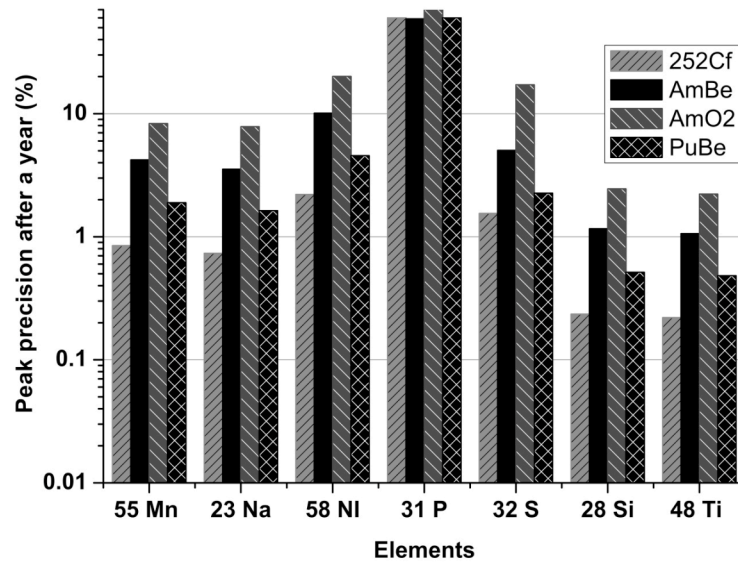


Figure 8-7. The peak precision for the major γ -ray peak of each element on the Martian surface, using the different neutron sources when the detectors are at 2 m depth with the neutron source on the surface.

The γ -ray energies are: ^{55}Mn = 7.243 MeV, ^{23}Na = 2.754 MeV, ^{58}Ni = 1.455 MeV, ^{31}P = 3.134 MeV, ^{32}S = 2.237 MeV, ^{28}Si = 3.540 MeV, ^{48}Ti = 1.381 MeV [(Révay et al., 2004; Firestone, 2003).

Table 8-5 gives the peak precision for the radioactive elements ^{40}K and ^{232}Th over the same time period; the peak precisions are independent of depth for the radioactive elements.

Element	Energy (MeV)	Peak Precision after a year (%)
K	1.461	0.053
Th	2.614	0.24

Table 8-5. The peak precision of the radioactive elements ^{40}K and ^{232}Th over the nominal mission lifetime (1 year).

Table 8-6 and Table 8-7 show the average number of ^{40}Ar 4.745 MeV γ -rays created per cm^{-3} of planetary surface and the detected γ -ray peak precision for a \varnothing 2.54 x 2.54 cm

LaBr₃(Ce) detector and a \varnothing 5.08 x 5.08 cm LaBr₃(Ce) detector using the different neutron sources for surfaces of ages 1.8 Gyr and 4.5 Gyr. The same nominal mission lifetime of one year was considered. At 2 m depth, no ⁴⁰Ar peak could be detected, no matter which neutron source was used.

Age of surface 4.5 Gyr	Counts yr ⁻¹ using ²⁵² Cf source	Peak Precision after a year (%)			
		²⁵² Cf	Am-Be	AmO ₂	Pu-Be
⁴⁰ Ar γ -ray creation cm ⁻³	5.5 x 10 ⁵	---	---	---	---
2 \varnothing 2.54 x 2.54 cm LaBr ₃ (Ce) detectors	74	11.65	No peak	No peak	No peak
2 \varnothing 5.08 x 5.08 cm LaBr ₃ (Ce) detectors	~ 2400	2.05	12.80	22.49	5.27

Table 8-6. The counts and peak precision of the ⁴⁰Ar peak at 4.745 MeV over the nominal mission lifetime (1 year) for surfaces of ages 4.5 Gyr. The first row shows the number of 4.745 MeV γ -rays created in a 25 cm radius from the ²⁵²Cf neutron source, the second the number of counts expected above background for 2 \varnothing 2.54 x 2.54 cm LaBr₃(Ce) detectors for all of the neutron sources and the third the number of counts expected above background for the 2 \varnothing 5.08 x 5.08 cm LaBr₃(Ce) detectors for all of the neutron sources. The \varnothing 2.54 x 2.54 cm LaBr₃(Ce) detectors only detect a ⁴⁰Ar peak above background when using the ²⁵²Cf neutron source.

Age of surface 1.8 Gyr	Counts yr ⁻¹ using ²⁵² Cf source	Peak Precision after a year (%)			
		²⁵² Cf	Am-Be	AmO ₂	Pu-Be
2 Ø 2.54 x 2.54 cm LaBr ₃ (Ce) detectors	--	No peak	No peak	No peak	No peak
2 Ø 5.08 x 5.08 cm LaBr ₃ (Ce) detectors	370	5.20	No peak	No peak	13.48

Table 8-7. The counts and peak precision of the ⁴⁰Ar peak at 4.745 MeV over the nominal mission lifetime (1 year) for surfaces of ages 1.8 Gyr. The first row shows the number of 4.745 MeV γ -rays created in a 25 cm radius from the ²⁵²Cf neutron source, the second the number of counts expected above background for 2 Ø 2.54 x 2.54 cm LaBr₃(Ce) detectors for all of the neutron sources and the third the number of counts expected above background for the 2 Ø 5.08 x 5.08 cm LaBr₃(Ce) detectors for all of the neutron sources. The Ø 2.54 x 2.54 cm LaBr₃(Ce) detectors only detect a ⁴⁰Ar peak above background when using the ²⁵²Cf neutron source.

Table 8-8 shows the peak precision obtained on the surface of Europa over a year and the limits of detectability for each elemental peak.

Element	Energy (MeV)	Peak Precision after a year (%)	Minimum detectable concentration for 10% peak precision (ppm)
B (NE)	0.478	3.25	0.05
Ba (n,n γ)	1.435	7.53	9.64
C (n, γ)	3.684	0.45	19.22
Ca (n, γ)	1.943	0.20	0.3
Cl (n, γ)	1.952	0.10	0.28
Cl (n, γ)	1.960	0.13	0.48
H (n, γ)	2.224	0.01	0.06
Li (n,n γ)	2.186	4.11	1.27
K (D)	1.461	0.12	0.39
Mg (n, γ)	2.828	1.51	14.10
Mg (n, γ)	3.916	2.06	26.40
Na (NE)	2.754	0.37	12.61
P (n,n γ)	3.134	1.84	476
S (n,n γ)	2.237	0.08	19.38

Table 8-8. The precision of the strongest γ -ray peaks for the major rock-forming and radioactive elements over the nominal mission lifetime (1 year) when the neutron source is 50 cm away from the geophysical package. NE= non-elastic scattering generated γ -ray (Révay et al., 2004; Firestone, 2003). The elements F, Br, Rb and Sr did not have photon production data or the cross sectional information was not detailed enough to produce good quality γ -ray spectra.

8.6 Discussion

8.6.1 Modelling the Martian and European Surfaces

As can be seen from Figure 8-4 and Figure 8-5, the peak precision of the elements listed is better than 10 % for all of the neutron sources when the detectors are 50 cm away with the exception of the P and Ni γ -ray peaks for the enriched AmO₂ neutron source. Many of the

elements have a peak precision of better than 1 %. When the detectors are at 2 m depth P, S, Ni and Cr cannot be obtained with a 10 % precision using the AmO₂ source. As seen in Figure 8-1, the neutron spectrum from the enriched AmO₂ drops sharply before 4 MeV, so the neutron flux is low at high energies compared to the other neutron sources; it also has the smallest neutron flux per gram. These effects contribute to the lower γ -ray emission associated with this source. Table 8-8 demonstrates that all of the elements listed could be measured with a precision of 10 % or less. F, Br, Rb, Sr and Zn are elements that are present on the Mars and Europa (Gellert et al., 2004; Zolotov and Shock, 2000); however, the cross sectional information and photon production data was either not detailed enough or not available so γ -rays from these elements could not be modelled. More detailed cross-sectional libraries and photon production data would be useful in the future to make the modelling more accurate.

8.6.2 Radiometric Dating

As shown in Table 8-5, obtaining the concentration of ⁴⁰K from the 1.461 MeV decay γ -ray peak is easily achieved over a time period of a year. However, as seen in Table 8-6 and Table 8-7, when modelling the neutron capture from ⁴⁰Ar in the Martian sub-surface for surfaces of 4.5 and 1.8 Gyr, insufficient counts were obtained for the required 10% precision using two detectors of dimensions \varnothing 2.54 cm x 2.54 cm at a distance of 50 cm from the neutron source. At 2 m depth no ⁴⁰Ar γ -rays are detected. From the model, the average ⁴⁰Ar 4.745 MeV γ -ray fluence in the volume of regolith surrounding the ²⁵²Cf neutron source is in excess of 10^5 counts cm⁻³ over the mission lifetime. Although sufficient γ -rays are produced to enable K-Ar dating, the detector geometry, effective area and in

particular the volume or the number of detected events is the limiting factor in this situation. By increasing the size of the detectors to \varnothing 5.08 x 5.08 cm or 9 times the volume, the peak precision reaches the required 10 % value needed to determine the age of a planetary surface when using the ^{252}Cf and (if the surface is older than 2.89 Gyr) Pu-Be neutron sources. At 2 m away from the neutron source, the ^{40}Ar count rate is not sufficient to detect the peak with any of the neutron sources even with larger volume detectors. This technique could be used to determine the age of a planetary surface to a better precision than when using XRF and mass spectroscopy when the detectors and neutron sources are separated by 50 cm.

8.6.3 The Neutron Sources and Detector

The $\text{LaBr}_3(\text{Ce})$ detector resolution is approximately 3.4 % at 662 keV. Although this is superior to many other scintillator detectors, this is not sufficient to resolve some of the elemental lines (See Chapter 4). It is important to characterise the neutron spectrum so that the peaks can be fitted or deconvolved (separated into each γ -ray line's contribution when two peaks have merged due to the insufficient resolution of the detector) through the model.

The $\text{LaBr}_3(\text{Ce})$ detector will become activated by the neutron source, and there will also be a contribution to the spectrum from the radioactive decay of ^{138}La (Chapter 4, Section 4.6.) at 1.436 MeV. This will add background to the γ -ray spectrum, and may interfere with other peaks (such as the 1.435 MeV peak of ^{138}Ba). Careful simulations are required to model the effect of the activation and the decay of ^{138}La on the γ -ray spectrum being

collected, so that the background can be removed. Reducing the concentration of the radioactive ^{138}La impurity in $\text{LaBr}_3(\text{Ce})$ will continue as the crystal growth methods improve. γ -ray emission also occurs from the neutron sources; for example, the decay γ -ray spectrum of ^{252}Cf is highly complex (Gehrke et al., 2004); the Am-Be reaction produces 26 keV and 59 keV γ -rays from the decay of ^{241}Am , and 4.438 MeV γ -rays from the Be neutron capture reaction (Mowlavi and Koochi-Fayegh, 2004; Vega-Carrillo et al., 2002). The 4.438 MeV γ -ray to neutron emission ratio in Am-Be is ~ 0.6 , therefore it will contribute substantially to the γ -ray spectrum. This γ -ray emission must be well-shielded from the γ -ray detectors or be accounted for and subtracted from the in-situ γ -ray spectra to remove these interferences.

The neutron source selected will require a trade-off between power generating capability, neutron flux, mass, volume and the impact of the radiation produced on other instruments present in any in-situ payload. The duration of the cruise phase will be a deciding factor; the short half-life of ^{252}Cf implies that it would not be useful on missions that have long cruise phases such as those to the moons of Jupiter and Saturn. The configuration of the in-situ platform will also play a role (i.e. whether the geophysical package is placed on a penetrator or a mole attached to a lander). Table 8-9 shows the properties of the four neutron sources studied, and the amount of Cd shielding required to reduce the neutron flux entering the detectors to $10^3/4\pi \text{ s}^{-1}$, thus reducing the dose received by the detectors.

Property	²⁵² Cf	Am-Be	Enriched AmO ₂	Pu-Be
Source Mass (g)	0.05	2000	2000	2000
Neutron flux (s ⁻¹)	1 x 10 ¹¹	2.8 x 10 ⁹	7.4 x 10 ⁸	1.4 x 10 ¹⁰
Average Energy (MeV)	2.10	4.98	2.31	4.94
Cd shielding thickness required to reduce flux from source to 10 ³ /4π s ⁻¹ (cm)	~ 1.6	~ 1.3	~ 1.2	~ 1.5
Mass of Cd shielding required (g)	70	57	53	66
Elements detectable to better than 10 % at 50 cm away from the source	All	All	All except Cr, Ni and P	All

Table 8-9. The properties of the neutron sources (O'Brien et al., 2009).

The ²⁵²Cf and Pu-Be sources provided the largest neutron fluxes and therefore the largest γ -ray count rates. For radiometric dating a ²⁵²Cf or Pu-Be neutron source would need to be accompanied by two \varnothing 5.08 x 5.08 cm detectors. However, the choice will be dominated by the power requirements of the in-situ platform.

LaBr₃(Ce) is radiation tolerant to 1 Mrad in Silicon (10¹² protons cm⁻² with a solar proton event spectrum (Owens et al., 2007b)); however, when considering an in-situ mission to Europa it will be necessary to consider the effect of high-energy electrons on the performance of the detectors.

8.7 Conclusion

A study has been carried out to model a geophysical package capable of carrying out GRS, and radiometric dating on two types of planetary surface. Possible neutron sources were simulated on a silicate-based surface and were compared to determine whether they could provide sufficient neutron flux in addition to the power required to operate an in-situ platform. The study demonstrated that the \varnothing 2.54 cm x 2.54 cm LaBr₃(Ce) detectors were sufficient to determine most of the elemental peaks of interest to a precision of better than 10 % with all the neutron sources, with the exceptions listed in Table 8-9; however, to obtain all the elemental peaks of interest, a high flux source such as the ²⁵²Cf or Pu-Be is required. In order to carry out K-Ar dating to a precision better than previously obtained both a high flux source such as ²⁵²Cf or Pu-Be and a detector of dimensions \varnothing 5.08 x 5.08 cm is required.

Chapter 9

Summary

This chapter briefly summarises the main conclusions of the thesis and outlines some future research aims.

Measuring the effect of geological and chemical processes, weather, biological processes and the interaction of SCR and GCR radiation with a planet is fundamental to understanding the formation, evolution and alteration of a planet. The geophysical package detailed in this thesis can be used to better understand the effect of these fundamental physical processes by measuring composition, constraining heat flow and measuring the age of a planetary surface. There are a number of future ESA and NASA planetary science missions that are in the planning or initial study phases, where the scientific objectives include determining the surface composition, measuring planetary surface heat flow and constraining planetary chronology. The geophysical package is capable of operation on landers and penetrators; both of these are possible in-situ platforms being proposed for these missions. In addition radioisotope power sources are being proposed for both thermal management and electricity generation; the power source might provide the source of neutrons to induce the γ -ray emission from the planetary surface.

Several γ -ray detector materials including CdTe, HPGe, CsI(Tl) and LaBr₃(Ce) were investigated for the geophysical package (Chapter 4). The conclusion was that LaBr₃(Ce) was the most suitable detector to carry out GRS on an in-situ platform. The detector is

compact, has low power requirements, does not require cooling, is very radiation tolerant compared to HPGe and has a resolution similar to that of compound semiconductor detectors. This does not preclude the use of semiconductor detectors in the future; the limiting factors in using HPGe detectors in in-situ missions are the mass and power requirements of the cooling system needed to keep the detector material at 77 K. If cooling equipment for HPGe detectors becomes more compact in the future, it would provide superior resolution. Likewise if CdTe crystal growing techniques improve (to allow the creation of larger crystals) and the impurity concentration is substantially reduced (to reduce the trapping effects), the material may also prove to be superior. However, semiconductor detectors are not as radiation tolerant as LaBr₃(Ce) and this could be a significant factor when choosing detector materials for missions to planetary bodies where the radiation environment is intense (e.g. Europa has an intense radiation environment due to its location within the Jovian magnetosphere). Using a LaBr₃(Ce) detector that has a resolution that is comparable to CdTe (Chapter 4) instead of CdTe would reduce the complexity of the detector output information (because multiple detector read-outs or CPPs would not be required), simplifying the instrument. The mass of the geophysical package when featuring LaBr₃(Ce) detectors is ~650 g. Further work is required to determine whether miniaturisation of the detector electronics could reduce the mass and volume of the package. The performance of the package could become more efficient as PMT and photodiode technology matures.

Chapters 5 and 6 detailed the verification of a Monte Carlo model of a planetary radiation environment using experimental data obtained at FRM II and data acquired by γ -ray spectrometers on 2001 Mars Odyssey. There was good agreement between the model and

the experimental data acquired at the FRM II facility; the ratio of experimental to modelled count rates gave consistent results for elements that were common to both the calibration samples and analogues with the exception of Fe. When verifying the model against data obtained in the orbit of Mars by the γ -ray spectrometer on 2001 Mars Odyssey, the model and data agreed within 20 % of each other. Differences can be attributed to the inability to model the exact radiation environment on the surface of Mars. Although this planetary radiation model is useful, there are always differences between model and experiment. In the future the accuracy of the model can be improved with more detailed cross sectional libraries and photon production data. As mentioned in Chapter 8, several elements had insufficient cross section or photon production data including Rb, Sr, Zn and Br, which meant that these elements could not be modelled. In order to model these elements accurately experiments must be carried out to determine the neutron cross sections with energy at neutron reactor facilities such as FRM II. Knowledge of the bulk density profile of a planetary surface will improve the accuracy of the model, allowing a more accurate interpretation of the data γ -ray acquired by the geophysical package and thus an improved composition profile of a planetary surface. Current forward models use a uniform density throughout the surface, this does not impact the interpretation of the orbital γ -ray data from spacecraft such as 2001 Mars Odyssey because it collects the γ -ray emission over a large swath (~ 240 km); however, when using GRS in-situ the variation in density will become significant, it will dictate over what area the composition is being probed (γ -rays have attenuation lengths between 15 g cm^{-2} and 40 g cm^{-2}).

Chapter 7 reported an investigation into the increased γ -ray emission that may occur from the surface of a planet as a result of a SPE, in this case Mars. There was correspondence

between SPEs and increased γ -ray emission detected in orbit of Mars; however, the results were inconclusive as to whether the increased γ -ray emissions could be attributed to the 2001 Mars Odyssey spacecraft or the planet. All the elements that could have originated from the planetary surface were present on the 2001 Mars Odyssey spacecraft, which was far closer to the γ -ray detector. The MCNPX model was used to determine whether SCR and GCR-induced γ -ray emissions were sufficient to carry out GRS in-situ of a planet. Several important conclusions were taken from the study:

- That it was essential to know the composition of the platform (spacecraft/lander/penetrator) upon which a γ -ray detector was based to allow accurate background subtraction and removal of elemental interferences from the γ -ray spectra to leave only γ -rays of planetary origin.
- In order to carry out GRS in-situ, a neutron source would be required, SCR and GCR-induced emissions are not sufficient to allow elemental composition analysis to 10 % precision within a reasonable timescale.

The model was used to investigate the suitability of several neutron sources to induce γ -ray emission on the planetary surface that could also be used for power generation (Chapter 8). It indicated that either a ^{252}Cf or Pu-Be based RTG would provide enough neutron flux to obtain γ -ray peaks with a better than 10% precision for both rock-forming and trace elements of interest within a timescale of a year. Two \varnothing 2.54 cm x 2.54 cm $\text{LaBr}_3(\text{Ce})$ detectors may be used to carry out both γ -ray backscatter densitometry and GRS; however, the detector volume is insufficient to carry out radiometric dating using the K-Ar method. If radiometric dating is desirable, then in addition to the neutron sources, two detectors of

dimensions of $\varnothing 5.08 \text{ cm} \times 5.08 \text{ cm}$ (103 cm^3) are required. A geophysical package using $\varnothing 2.54 \text{ cm} \times 2.54 \text{ cm}$ $\text{LaBr}_3(\text{Ce})$ detectors could have a mass smaller than 650 g. Using detectors of $\varnothing 5.08 \text{ cm} \times 5.08 \text{ cm}$, the mass of the detector system becomes $\sim 1.5 \text{ kg}$. The mass constraints of an in-situ platform may dictate whether radiometric dating is feasible for a particular mission. In order to carry out K-Ar dating, knowledge of the concentration of ^{36}Ar is also required to remove the ^{40}Ar contribution created via non-radiogenic means. However, this isotope could not be detected within the model; further work is required to understand the minimum detectable limits of this isotope of Ar.

In order to probe below the oxidant extinction depth, it would be necessary for the geophysical package and RTG to be installed on a penetrator/ sub-surface probe. If the package were installed on a mole and the RTG on a lander, the distance between source and detectors would be in excess of 2 m, and as shown in Chapter 8, this would not allow the detectors to obtain a 10 % precision on a number of peaks (e.g. P and Cr), even with the strongest neutron sources. The choice of neutron source is ultimately a trade-off between the mass and volume constraints of the in-situ platform, the total power requirements of the mission, the mission cruise phase (^{252}Cf only has a half-life of 2.654 years so it would not be suitable for missions to the outer solar system) and the desired neutron flux/the elements of interest in the in-situ mission.

The geophysical package proposed can operate on any surface in conjunction with a neutron source. It can operate regardless of whether an atmosphere is present or not, and may be used on liquid (Titan) or solid planetary surfaces (such as Mars or Europa), as γ -ray

emission from the surface can penetrate any casing required on the in-situ platform. However, it is important to model it on the individual planetary body and in the configuration of the in-situ platform (i.e. penetrator/ lander). It may also be necessary to model the natural radiation environment of the planetary body to examine the effect on the detector and additional background it may create in the γ -ray spectrum. For example, Europa has an intense radiation environment that will subject the detector material to high doses of radiation and will contribute to the γ -ray background originating from the in-situ platform. It will be necessary to model the dose subjected to the detector materials from both the planetary radiation environment and the neutron source to determine whether a detector material is suitable for a given mission. If the neutron source is well characterised, the γ -ray background from the in-situ platform can be modelled very accurately and used for background subtraction. Flight hardware could be used in conjunction with a neutron source and terrestrial analogues of Martian meteorites to obtain experimental data that could be used to further verify the model. The model developed may be used as a forward model to interpret the data acquired by the geophysical package on a planetary surface if it was selected for a mission. The γ -ray contribution from the neutron sources (Chapter 8) needs to be studied further to enable subtraction from the γ -ray spectra.

The geophysical package has been modelled and shown to be suitable for γ -ray backscatter densitometry and GRS, and may be used for radiometric dating if larger volume detectors are used. The studies described in this thesis can contribute to the development of the geophysical package to optimise the performance of the instrument for future planetary applications.

Appendix A

MCNPX general planetary radiation environment code modelling the geophysical package and neutron source

Simulating geophysical package with Cf-252 source on Mars- user can change the density profile and composition of the atmosphere and surface as required.

```

1 0 1 -2 -3 (-4:5:6) (-5:7:6) (-7:8:6) (-8:9:6) (-9:10:6)
    (-10:11:6) (-11:12:6) (-12:13:6) (-13:14:6) (-14:15:6)
    (-15:16:6) (-16:17:6) (-17:18:6) (-18:19:6) (-19:20:6)
    (-20:21:6) (-21:22:6) (-22:23:6) (-23:24:6) (-24:25:6)
    (-25:26:6) (-26:27:6) (-27:47:6) (-29:30:6)
    imp:h=1 imp:n=1 imp:p=1 $Internal Universe
2 0 -1:2:3 imp:h=0 imp:n=0 imp:p=0 $ External Universe
3 1 -4.796E-13 4 -5 -6 imp:h=1
    imp:n=1 imp:p=1 tmp=2.32659E-8 $First atmospheric shell
4 1 -3.914E-12 5 -7 -6 imp:h=1
    imp:p=1 imp:n=1 tmp=2.32659E-8 $Second atmospheric shell
5 1 -3.89E-11 7 -8 -6 imp:h=1
    imp:n=1 imp:p=1 tmp=1.55106E-8 $Third atmospheric shell
6 1 -3.914E-10 8 -9 -6 imp:h=1
    imp:n=1 imp:p=1 tmp=1.12021E-8 $Fourth atmospheric shell
7 1 -3.91E-9 9 -10 -6 imp:h=1
    imp:n=1 imp:p=1 tmp=1.03404E-8 $Fifth atmospheric shell
8 1 -3.88E-8 10 -11 -6 imp:h=1 imp:n=1 imp:p=1
    tmp=1.077125E-8 $Sixth atmospheric shell

```

9 1 -3.91E-7 11 -12 -6 imp:h=1
 imp:n=1 imp:p=1 tmp=1.421805E-8 \$Seventh atmospheric shell
 10 1 -2.781E-6 12 -13 -6 imp:h=1
 imp:n=1 imp:p=1 tmp=1.63723E-8 \$Eighth atmospheric shell
 11 1 -1.257E-5 13 -14 -6 imp:h=1 imp:n=1 imp:p=1
 tmp=1.29255E-8 \$Ninth atmospheric shell
 12 1 -0.00001779 14 -15 -6 imp:h=1
 imp:n=1 imp:p=1 tmp=1.85395E-8
 \$Tenth atmospheric shell to surface
 13 2 -1 15 -16 -6 imp:h=1 imp:p=1 imp:n=1 tmp=1.85395E-8
 \$ 1st surface layer to 2 cm depth- dust layer
 14 2 -2 16 -17 -6 imp:h=1 imp:p=1 imp:n=1 tmp=1.85395E-8
 \$ 2nd surface layer to 10 cm depth
 15 2 -2 17 -18 -6 imp:h=1 imp:p=1 imp:n=1 tmp=1.85395E-8
 \$ 3rd surface layer to 20 cm depth
 16 2 -2 18 -19 -6 imp:h=1 imp:p=1 imp:n=1 tmp=1.85395E-8
 \$ 4th surface layer to 30 cm depth
 17 2 -2 19 -20 -6 imp:h=1 imp:p=1 imp:n=1 tmp=1.85395E-8
 \$ 5th surface layer to 40 cm depth
 18 2 -2 20 -21 -6 imp:h=1 imp:p=1 imp:n=1 tmp=1.85395E-8
 \$ 6th surface layer to 50 cm depth
 19 2 -2 21 -22 -6 imp:h=1 imp:p=1 imp:n=1 tmp=1.85395E-8
 \$ 7th surface layer to 62 cm depth
 20 2 -3 22 -23 -6 imp:h=1 imp:p=1 imp:n=1 tmp=1.85395E-8
 \$ 8th surface layer to 80 cm depth
 21 2 -3 23 -24 -6 imp:h=1 imp:p=1 imp:n=1 tmp=1.85395E-8
 \$ 9th surface layer to 90 cm depth
 22 2 -3 24 -25 -6 imp:h=1 imp:p=1 imp:n=1 tmp=1.85395E-8
 \$ 10th surface layer to 1 m depth
 23 2 -3 25 -26 -6
 imp:h=1 imp:p=1 imp:n=1 tmp=1.85395E-8

\$ 11th surface layer to 1.5 m depth
 24 2 -3 26 -27 -6 (-53:54:49) 61
 imp:h=1 imp:p=1 imp:n=1 tmp=1.85395E-8
 \$ 12th surface layer to 5 m depth containing detectors and neutron source
 25 2 -3 27 -47 -6
 imp:h=1 imp:p=1 imp:n=1 tmp=1.85395E-8
 \$ 13th surface layer
 26 0 29 -30 -6 imp:h=1 imp:n=1 imp:p=1
 \$Detector in orbit (if required- need to include a surface tally for surface 29 if wish to
 track gamma rays e.g. F2:p 29)
 27 0 -50 48 -49 imp:h=1 imp:p=1 imp:n=1
 \$ 1st detector at 2m depth
 28 0 51 -60 -49 imp:h=1 imp:p=1 imp:n=1
 \$ 2nd detector at 2 m depth
 29 2 -3 53 -54 -49 (-56:52:49) imp:h=1 imp:p=1 imp:n=1
 \$ Casing of penetrator (in this case composition set to the surface
 \$ of the planet)
 30 2 -3 56 -52 -49 (-48:50:49) (-51:60:49) (-57:51:49)
 imp:h=1 imp:p=1 imp:n=1 \$ Inside of penetrator
 \$ (in this case composition set to the surface of the planet)
 31 2 -3 57 -51 -49 imp:h=1 imp:p=1 imp:n=1
 \$ W Shield for 137 Cs source
 \$ (in this case composition set to the surface of the planet)
 32 5 -15.1 -61 imp:h=1 imp:p=1 imp:n=1
 \$ Neutron source 252 Cf

 1 py 0 \$Universe surface cards
 2 py 50000000 \$Universe surface cards
 3 cy 200000 \$ Cylindrical boundary of Universe
 4 py 21100000 \$Atmosphere surface cards, layer 1
 5 py 22960000 \$Atmosphere surface cards, layer 2

6 cy 100000 \$ Cylindrical boundary of planetary surface 100 m radius-

\$ for orbital measurements this can be larger

7 py 25440000 \$Atmosphere surface cards, layer 3

8 py 27920000 \$Atmosphere surface cards, layer 4

9 py 30420000 \$Atmosphere surface cards, layer 5

10 py 32900000 \$Atmosphere surface cards, layer 6

11 py 35380000 \$Atmosphere surface cards, layer 7

12 py 37880000 \$Atmosphere surface cards, layer 8

13 py 40360000 \$Atmosphere surface cards, layer 9

14 py 40840000 \$Atmosphere surface cards, layer 10

15 py 41100000 \$Surface

16 py 41100002 \$Surface 2 cm depth

17 py 41100010 \$Surface 10 cm depth

18 py 41100020 \$Surface 20 cm depth

19 py 41100030 \$Surface 30 cm depth

20 py 41100040 \$Surface 40 cm depth

21 py 41100050 \$Surface 50 cm depth

22 py 41100062 \$Surface 62 cm depth

23 py 41100080 \$Surface 80 cm depth

24 py 41100090 \$Surface 90 cm depth

25 py 41100100 \$Surface 100 cm depth

26 py 41100150 \$Surface 150 cm depth

27 py 41100500 \$Surface 500 cm depth

28 py 41101000 \$Surface 1000 cm depth- use if required

29 py 1400000 \$ Orbital detector surface cards altitude 397 km

30 py 1400010

31 py 39999950

32 cy 385000 \$ Shells within atm and surface, 3.85 km

33 cy 770000 \$ Shells within atm and surface, 7.7 km

34 cy 1155000 \$ Shells within atm and surface, 11.55 km

35 cy 1540000 \$ Shells within atm and surface, 15.4 km

36 cy 1925000 \$ Shells within atm and surface, 19.25 km
 37 cy 2310000 \$ Shells within atm and surface, 23.10 km
 38 cy 2695000 \$ Shells within atm and surface, 26.95 km
 39 cy 3080000 \$ Shells within atm and surface, 30.80 km
 40 cy 3465000 \$ Shells within atm and surface, 34.65 km
 41 py 41101500 \$ Surface 1500 cm depth- use if required
 42 py 41102000 \$ Surface 2000 cm depth- use if required
 43 py 41102500 \$ Surface 2500 cm depth- use if required
 44 py 41103000 \$ Surface 3000 cm depth- use if required
 45 py 41103500 \$ Surface 3500 cm depth- use if required
 46 py 41104000 \$ Surface 4000 cm depth- use if required
 47 py 41120000 \$ Surface 20,000 cm depth
 48 py 41100214.3 \$ Long sonde top of detector
 49 cy 1.27 \$ Detector radius 100 cm
 50 py 41100216.84 \$ Long sonde bottom detector
 51 py 41100206.3 \$ Short sonde top detector
 52 py 41100224.7 \$ Casing of probe bottom
 53 py 41100200 \$ The sub surface probe dimensions: top
 54 py 41100225 \$ The sub surface probe dimensions: bottom
 55 cy 1.57 \$ Radius of the probe
 56 py 41100200.3 \$ Casing of probe top
 57 py 41100201.3 \$ 137 Cs source position start of Cd shielding
 58 py 41100206.5 \$ \$ End of Cd shielding
 59 c/y 0 0.76 0.5 \$ Axis of Cd shielding
 60 py 41100208.84 \$ Short sonde bottom detector
 61 s 0 41100266.84 0 0.5 \$ 252Cf source 50 cm from detectors

m1 6000 -0.261 8016 -0.696 7000 -0.027 18000 -0.0160
 \$Atmosphere material card, CO2, Ar, N
 m2 8016 -0.40685874 14000 -0.215 20000 -0.0477
 16000 -0.02 13027 -0.0504 11023 -0.0176

```

12000 -0.0477 26056 -0.17 17000 -0.004
1001 -0.0033333 19000 -0.0045 22000 -0.005
25055 -0.0034 24000 -0.0015 6000 -0.006
64000 -0.000004 62000 -0.000003 90232 -0.0000008
92238 -0.0000013 $Surface material card
$ based on Mars Pathfinder
m3 6000 1 $ C fibre for casing of probe- not applied in this programme, change
$ cell 29 to m3 if want to include casing
m4 74000 1 $ Cd for 137 Cs shielding- not applied at present; change cell 31 to m4
$ if want to include shielding in programme
m5 98252 1 $ 252Cf
mode p n
phys:p 10 1 1 0 1
nps 5E8 $ No of particles 5E8
sdef cel=32 par=sf erg=-3 pos=0 41100266.84 0
$Cf-252 fission spectrum at the surface of Mars (50 cm from
detectors)
f4:p 27 $ Detector 1 at 2m depth: photons in void detector- tally from 1 keV to 10 MeV
e4 0.001 0.002 0.003 0.004 0.005 0.006 0.007 0.008 0.009
0.010 0.011 0.012 0.013 0.014 0.015 0.016 0.017 0.018 0.019
0.020 0.021 0.022 0.023 0.024 0.025 0.026 0.027 0.028 0.029
0.030 0.031 0.032 0.033 0.034 0.035 0.036 0.037 0.038 0.039
-----c Removed for brevity-----
9.970 9.971 9.972 9.973 9.974 9.975 9.976 9.977 9.978 9.979
9.980 9.981 9.982 9.983 9.984 9.985 9.986 9.987 9.988 9.989
9.990
f14:p 28 $ Detector 2 at 2m depth: photons in void detector- tally from 1 keV to 10 MeV
e14 0.001 0.002 0.003 0.004 0.005 0.006 0.007 0.008 0.009
0.010 0.011 0.012 0.013 0.014 0.015 0.016 0.017 0.018 0.019
0.020 0.021 0.022 0.023 0.024 0.025 0.026 0.027 0.028 0.029
0.030 0.031 0.032 0.033 0.034 0.035 0.036 0.037 0.038 0.039

```

-----c Removed for brevity-----

9.970 9.971 9.972 9.973 9.974 9.975 9.976 9.977 9.978 9.979

9.980 9.981 9.982 9.983 9.984 9.985 9.986 9.987 9.988 9.989

References

- Adams, J. A. S. and Gasparini, P., (1970), 'Detectors', γ -ray Spectroscopy of Rocks, Methods in Geochemistry and Geophysics, Elsevier Publishing Company, Chapter 2, pp. 23-67.
- Adler, I. et al., (1973), 'Apollo 15 and 16 Results of the Integrated Geochemical Experiment, The Moon', Kluwer Academic Publishers, pp. 487-504.
- Ambrosi, R. M., Ball, A. J., Nelms, N., Skidmore, M. S., (2007), DEN Monte Carlo Model (Version 2.2), HP3-TN-DEN-06-UL, Updated: 03/09/07.
- Ambrosi, R. M., Ball, A. J., Nelms, N., Talboys, D., Bentley, M. S., Spohn, T., Nadalini, R., Hagermann, A., Richter, L., Calcutt, S., Fraser, G. W., Bridges, J., Zarnecki, J. S., Cockell, C. S., Grady, M. M., Simon, H., Siffert, P., Skidmore, M. S., (2006), 'X-ray and γ -ray Spectrometers for the Heat Flow and Physical Properties Instrument (HP³) on the ExoMars Geophysical and Environmental Package', *Presented at the 4th International Planetary Probe Workshop, Pasadena, 27-30th June 2006, Submitted to: Conference Proceedings, 4th International Planetary Probe Workshop 27-30th June 2006.*
- Ambrosi, R. M., Talboys, D., Sims, M. R., Bannister, N. P., Makarewicz, M., Stevenson, T., Hutchinson, I. B., Watterson, J. I. W., Lanza, R. C., Richter, L., Mills, A., Fraser, G. W., (2005), 'Neutron Activation Analysis, Gamma-ray Spectrometry and Radiation Environment Monitoring Instrument Concept: GEORAD', *Nuclear Instruments and Methods in Physics Research A*, 539, pp.198-216.
- Andolz, F. J., (1998), Lunar Prospector Mission Handbook, NASA AMES Research Center, Lockheed Martin Missiles and Space Co., LMMS/P458481, 10/04/98.
- Ball, A. J., Bentley, M. S., Nelms, N., Ambrosi, R. M., Hall, C., Mucklow, C. E. T., (2007), HP³ DEN Detailed Design Document (Version 1.2), HP3-TN-DEN-05-OUPSSRI, Updated: 24/08/2007.
- Ball, A. J., Solomon, C. J., Zarnecki, J. C., (1996), 'A Compton Backscatter Densitometer for the RoLand Comet Lander—Design Concept and Monte Carlo Simulations', *Planetary and Space Science*, 44, pp. 283-285.
- Bao, X. J., Schlesinger, T. E. and James, R. B., (1995), 'Electric Properties of Mercuric Iodide', Volume 43: Semiconductors for Room Temperature Nuclear Detector Applications, T. E. Schlesinger and R. B. James (Eds.), Semiconductors and Semimetals, R. K. Willardson, A. C. Beer and E. R. Weber (Eds.), Academic Press Ltd., Chapter 4, pp. 111- 168.

- Barnes, A., (1992), 'Acceleration of the Solar Wind', *Reviews of Geophysics*, 30, pp. 43-55.
- Belgya, T. and Révay, Zs., (2004), 'Gamma-Ray Spectrometry', Handbook of Prompt Gamma Activation Analysis with Neutron Beams, G. L. Molnár (Ed.), Kluwer Academic Publishers, Chapter 4, pp. 71- 112.
- Berger, M. J., Coursey, J.S., Zucker, M.A. and Chang, J., (2005), ESTAR, PSTAR, and ASTAR: Computer Programs for Calculating Stopping-Power and Range Tables for Electrons, Protons, and Helium Ions (Version 1.2.3), National Institute of Standards and Technology, Gaithersburg, MD URL: <http://physics.nist.gov/Star> [2008, November 28].
- Bergman, J., (2003), Windows to the Universe, University Corporation for Atmospheric Research,
URL:http://www.windows.ucar.edu/tour/link=/mars/images/MPF_T_profile2_gif_image.html.
- Bhardwaj, A. and 13 colleagues, (2007), 'X-rays from Solar System Objects', *Planetary and Space Science*, 55, pp. 1135-1189.
- Boynton, W. V., and 27 colleagues, (2007), 'Concentration of H, Si, Cl, K, Fe, and Th in the Low- and Mid-latitude Regions of Mars', *Journal of Geophysical Research* 112, E12S99, doi:10.1029/2007JE002887.
- Boynton, W. V. et al., (2004), 'The Mars Odyssey Gamma-Ray Spectrometer Instrument Suite', *Space Science Reviews*, 110, pp. 37-83.
- Boynton, W.V., (2004), Mars 2001 Odyssey γ -ray Spectrometer Derived High Energy Neutron Detector Data V1.0, ODY-M-GRS-4-DHD-V1.0, NASA Planetary Data System Geosciences Node, URL: <http://grspds.lpl.arizona.edu/>.
- Boynton, W.V., (2003), Mars 2001 Odyssey γ -ray Spectrometer Summed Gamma Spectra V1.0, ODY-M-GRS-5-SGS-V1.0, NASA Planetary Data System Geosciences Node, URL: <http://grspds.lpl.arizona.edu/>.
- Boynton, W.V., (2002), Mars 2001 Odyssey, γ -ray Spectrometer Corrected Gamma Spectra V1.0, ODY-M-GRS-4-CGS-V1.0, NASA Planetary Data System Geosciences Node, URL: <http://grspds.lpl.arizona.edu/>.
- Briggs, M., Ambrosi R. M., Nelms N. et al., (2005), 'Proposed Method to Improve the Accuracy of Thermal Conductivity Measurements of a Planetary Regolith', *Nuclear Instruments and Methods in Physics Research A*, 541, pp. 651-656.
- Brookshaw, M., (2006), Radiation Detection and Measurement,
URL: <http://www.upei.ca/~phys221/mbrookshaw/Glossary/glossary.html>.

- Brückner, J. and Masarik, J., (1997), 'Planetary Gamma-ray Spectroscopy of the Surface of Mercury', *Planetary and Space Science*, 45, pp. 39-48.
- Brückner, J., Körfer, M., Wänke, H., Schroeder, A. N. F., Filges, D., Dragovitsch, P., Englert, P. A. J., Starr, R., Trombka, J. I., Taylor, I., Drake, D. M., Shunk, E. R., (1991), 'Proton-induced Radiation Damage in Germanium Detectors', *IEEE Transactions on Nuclear Science*, 38, pp. 209-217.
- Buis, E. J., Beijers, H., Brandenburg, S., Bos, A.J.J., Dathy, C., Dorenbos, P., Drozdowski, W., Kraft, S., Maddox, E., Otendorf, R. W., Owens, A., Quarati, F., (2007), 'Measurement and Simulation of Proton-induced Activation of LaBr₃:Ce', *Nuclear Instruments and Methods in Physics Research A*, 578, pp. 239-245.
- Bucciati, A., Prati, F., (1993), 'Preliminary Data on the Content of Volatile Elements in the Rocks from Mount Erebus (Ross Island, Antarctica)', *Terra Antartica*, 1, pp. 88-91.
- BURLE Technologies Inc., (2005), Placacon™ Photomultiplier Tube Assembly Data Sheet, 85011-501, URL: http://www.burle.com/mcp_pmts.htm.
- Cappellani, F. and Restelli, G., (1968), 'X-ray and Gamma-ray Spectroscopy', Semiconductor Detectors, G. Bertolini and A. Coche (Eds.), North-Holland Publishing Company, Section 4.4, pp. 365- 408.
- Cane, H. V., Reames, D. V., and von Rosenvinge, T. T., (1988), 'The Role of Interplanetary Shocks in the Longitude Distribution of Solar Energetic Particles', *Journal of Geophysical Research*, 93, pp. 9555–9567
- Chadwick, M. B., Oblozinsky, P., Herman, M. et al., (2006), ENDF/B-VII.0: Next Generation Evaluated Nuclear Data Library for Nuclear Science and Technology", Nuclear Data Sheets, 107, pp. 2931-3060.
- Cleghorn, T. F., Saganti, P. B., Zeitlin, C. J., Cucinotta, F. A., (2004), 'Solar Particle Events Observed at Mars: Dosimetry Measurements and Model Calculations', *Advances in Space Research*, 33, pp. 2215-2218.
- Crombie, M. K., Harshman, K. P., McArthur, G. K., Shinohara, C., Boynton, W. V., (2003), '2001 Mars Odyssey Gamma-ray Spectrometer Science Data Products', *Lunar and Planetary Science*, XXXIV, 1671.
- Darken, L. S. and Cox, C. E., (1995), 'High-Purity Germanium Detectors', Volume 43: Semiconductors for Room Temperature Nuclear Detector Applications, T. E. Schlesinger, R. B. James (Eds.), Semiconductors and Semimetals, R. K. Willardson, A. C. Beer, E. R., Weber (Eds.), Academic Press Ltd., Chapter 2, pp. 23- 85.

- Derenzo, S. E. et al., (2003), 'The Quest for the Ideal Inorganic Scintillator', *Nuclear Instruments and Methods in Physics Research A*, 505, pp. 111-117.
- Dickin, A. P., (2005), 'K-Ar and Ar-Ar Dating', *Radioisotope Geology* (2nd Edition), Cambridge University Press, Chapter 10, pp. 245-274.
- Dorenbos, P., (2002), 'Light Output and Energy Resolution of Ce³⁺-doped Scintillators', *Nuclear Instruments and Methods in Physics Research A*, 486, pp. 208-213.
- Dyar, M.D., and 12 colleagues, (1995), 'Mineralogy', Planetary Surface Instruments Workshop, LPI Technical Report 95-05, C. Meyer, A. Treiman, T. Kostiuk, (Eds.), Lunar and Planetary Institute, Houston, Chapter 6, pp. 65- 84.
- Economou, T., (2001), 'Chemical Analyses of Martian Soil and Rocks Obtained by the Pathfinder Alpha Proton X-ray Spectrometer', *Radiation Physics and Chemistry*, 61, pp. 191-197.
- EG & G Ortec, (1995), Solid State Photon Detectors Operators Manual: GEM Series, HPGe, EG&G Publishing.
- EG&G Ortec, (1984), Experiments in Nuclear Science- Introduction to Theory and Basic Applications, AN34- Lab Manual (3rd Edition), EG&G Publishing.
- EURORAD, (2008), γ -ray Detection Probe: LaBr₃ Instruction Manual, May 2008.
- EURORAD, (2006), Hybrid Detector Prototype User Manual, December 2006.
- EURORAD, (1998a), Compact Pulse Processor for High Resolution Spectroscopy with CdTe Detectors, Charge Loss Compensator Model CPP II-NIM Operation Manual, September 1998, URL: http://www.eurorad.com/PDF/UG_CPP-NIM.pdf.
- EURORAD, (1998b), Solid State Scintillation Probe Models SC1010, SC1515, SC1530, SC2525 Instruction Manual, November 1998.
- Evans, L. G., Reedy, R. C., Starr, R. D., Kerry, K. E., Boynton, W. V., (2007), 'Analysis of Gamma-ray Spectra Measured by Mars Odyssey', *Journal of Geophysical Research*, 111, E03S04, doi:10.1029/2005JE002657 [printed 112(E3), 2007].
- Evans, L. G., Reedy, R. C., Boynton, W. V., (2003), 'Effects of Solar Particles on the Gamma-ray Spectrometer', *Lunar and Planetary Science*, XXXIV, 1591.
- Evans, L. G., Boynton, W. V., Reedy, R. C., Starr, R. D., Trombka, J. I., (2002), 'X-Ray and Gamma-Ray Detectors and Applications IV', R. B. James, L. A. Franks, A. Burger, E. M. Westbrook, R. D. Durst (Eds.), Proceedings of SPIE 4784, pp. 31- 44.
- Evans, L. G., Starr, R. D., Brückner, J., Reedy, R. C., Boynton, W. V., Trombka, J. I., Goldsten, J. O., Masarik, J., Nittler, L. R., McCoy, T. J., (2001), 'Elemental Composition from

- Gamma-ray Spectroscopy of the NEAR-Shoemaker Landing site on 433 Eros', *Meteoritics & Planetary Science*, 36, pp. 1639-1660.
- Feldman, W. C. et al., (2004), 'Gamma-Ray, Neutron, and Alpha-Particle Spectrometers for the Lunar Prospector Mission', *Journal of Geophysical Research*, 109, E07S06, doi:10.1029/2003JE002207.
- Firestone, R. B., (2003), LBNL Isotopes Project Nuclear Data Dissemination Home Page. Retrieved: June, 2009, URL: <http://ie.lbl.gov/toi.html>.
- Futaana, Y., Barabash, M., Yamauchi, S. et al, (2008), 'Mars Express and Venus Express Multi-point Observations of Geoeffective Solar Flare Events in December 2006', *Planetary and Space Science*, 56, pp. 873-880.
- Gao, Y., Phipps, A., Talyor, M., Clemmet, J., Parker, D., Crawford, I. A., Ball, A. J., Wilson, L., de Silva Curil, A., Davies, P., Sweeting, M., Baker, A., (2007), UK Lunar Science Missions: MoonLITE and Moonraker, *Presented at DGLR Int. Symp. "To Moon and Beyond", Bremen, Germany, 14-16 March 2007*.
- Gehrels, N., Crannell, C. J., Orwig, L. E., Forrest, D. J., Lin, R. P., Starr, R., (1988), 'Hard X-ray and Low-energy Gamma-ray Spectrometers', *Solar Physics*, 118, pp. 233-268.
- Gehrke, R. J., Aryaeinejad, R., Hartwell, J. K., Yoon, W. Y., Reber, E., Davidson, J. R., (2004), 'The γ -ray Spectrum of ^{252}Cf and the Information Contained within it', *Nuclear Instruments and Methods in Physics Research Section B*, 213, pp. 10-21.
- Gellert, R., Rieder, R., Anderson, R., Bruckner, J., Clark, B. C., Dreibus, G., Economou, T., Klingelhofer, G., Lugmair, G. W., Ming, D. W., Squyres, S. W., d'Uston, C., Wanke, H., Yen, A., Zipfel, J., (2004), 'Chemistry of Rocks and Soils in Gusev Crater from the Alpha Particle X-ray Spectrometer', *Science*, 305, pp. 829-832.
- Goldsten, J.O., Rhodes, E. A., Boynton, W. V., Feldman, W. C., Lawrence, D. J., Trombka, J. I., Smith, D. M., Evans, L. G., White, J., Madden, N. W., Berg, P. C., Murphy, G. A., Gurnee, R. S., Strohbahn, K., Williams, B. D., Schaefer, E. D., Monaco, C. A., Cork, C. P., Eckels, J. D., Miller, W. P., Burks, M. T., Hagler, L. B., Deteresa, S. J., and Witte, M. C., (2007), 'The MESSENGER Gamma-Ray and Neutron Spectrometer', *Space Science Reviews*, 131, pp. 339-391.
- Goldsten, J. O., (1998), 'The NEAR X-ray/ γ -ray Spectrometer', *John Hopkins APL Technical Digest*, 19, pp. 126-135.
- Govil, I. M., (2001), 'Proton Induced X-ray Emission- a Tool for Non-destructive Trace Element Analysis', *Current Science*, 80, pp. 1542- 1549.

- Grande, M. and 47 colleagues, (2003), 'The D-CIXS X-ray Mapping Spectrometer on SMART-1', *Planetary and Space Science*, 51, pp. 427-433.
- GRS team, (2005), Model spectrum Calculations (Version 0.5),
URL: <http://grspds.lpl.arizona.edu/>.
- Hahn, B. C., and McLennan, S. M., (2007), 'Mars Odyssey Gamma-ray Spectrometer Elemental Abundances and Apparent Relative Surface Age: Implications for Martian Crustal Evolution', *Journal of Geophysical Research*, 112, E03S11, doi: 10.1029/2006JE002821.
- Hage-Ali, M. and Siffert, P., (1995), 'CdTe Nuclear Detectors and Applications', Volume 43: Semiconductors for Room Temperature Nuclear Detector Applications, T. E. Schlesinger and R. B. James (Eds.), Semiconductors and Semimetals, R. K. Willardson, A. C. Beer and E. R. Weber (Eds.), Academic Press Ltd., Chapter 8, pp. 291- 335.
- Hagermann, A., (2005), 'Planetary Heat Flow Measurements', *Philosophical Transactions of the Royal Society A*, 363 (1837), pp. 2777-2791.
- Hardie, G., Segel, R. E., Elwyn, A. J., Monahan, J. E., (1988), 'Nonresonant Capture of Low-energy Protons by ^{27}Al ', *Physics Review C*, 38, pp. 2003 – 2012.
- Hartmann, W. K. and Neukum, G., (2001), 'Cratering Chronology and the Evolution of Mars', *Space Science Reviews*, 96, pp. 165-194.
- Healy, J., de Groot J., Kestin J., (1976), 'Proton Induced X-ray Emission- a Tool for Non-destructive Trace Element Analysis', *Physica C*, 82, pp. 392-408.
- Hearst, J. R. and Carlson, R. C., (1969), 'The RIDS: A Density Logger for Rough Holes', *Geophysics*, 34, pp. 222-234.
- Hitomi, K., Onodera, T., Shoji, T., He, Z., (2008), 'Investigation of Pixelated TlBr Gamma-ray Spectrometers with the Depth-sensing Technique', *Nuclear Instruments and Methods in Physics Research A*, 591, pp. 276- 278.
- Hubbell, J.H. and Seltzer, S.M., (2004), Tables of X-Ray Mass Attenuation Coefficients and Mass Energy-Absorption Coefficients (Version 1.4), National Institute of Standards and Technology, Gaithersburg, MD, URL: <http://physics.nist.gov/xaamdi> [2008, August 22].
- Hundhausen, A. J., (1995), 'The Solar Wind', Introduction to Space Physics, M. G. Kivelson and C. T. Russell (Eds.), Cambridge University Press, Chapter 4, pp. 91-128.
- Jenkins, R., (1999a), 'More Recent Trends in X-ray Fluorescence Instrumentation', X-ray Fluorescence Spectrometry (2nd Edition), Volume 152 in Chemical Analysis: A Series of Monographs on Analytical Chemistry and its Applications, J. D., Winefordner (Ed.), Wiley-Interscience, Chapter 8, pp. 123-140

- Jenkins, R., (1999b), 'Production and Properties of X-rays', X-ray Fluorescence Spectrometry (2nd Edition), Volume 152 in Chemical Analysis: A Series of Monographs on Analytical Chemistry and its Applications, J. D., Winefordner (Ed.), Wiley-Interscience, Chapter 1, pp. 1-16.
- Joint Jupiter Science Definition Team, (2009), NASA/ESA Study Team, EJSM NASA/ESA Joint Summary Report,
URL: <http://sci.esa.int/science-e/www/object/index.cfm?fobjectid=44035>, 20 Jan 2009.
- Joint Titan Saturn System Mission Science Definition Team, (2009), ESA Study Team, NASA Study Team, TSSM NASA/ESA Joint Summary Report,
URL: <http://sci.esa.int/science-e/www/object/index.cfm?fobjectid=44033#>, 19 Jan 2009.
- Jun, I. and Garrett, H. B., (2005), 'Comparison of High-energy Trapped Particle Environments at the Earth and Jupiter', *Radiation Protection and Dosimetry*, 116, pp. 50–54, doi:10.1093/rpd/nci074.
- Kaplan, I., (1963), 'Neutron Induced Reactions', *Nuclear Physics* (2nd Edition), Addison Wesley Publishing Company, Inc., USA, Chapter 16, Section 5, pp.465-477.
- Kelly, N. J., Boynton, W. V., Kerry, K., Hamara, D., Janes, D., Reedy, R. C., Kim, K. J., and Haberle, R. M., (2007), 'Seasonal Polar Carbon Dioxide Frost on Mars: CO₂ Mass and Columnar Thickness Distribution', *Journal of Geophysical Research*, 111, E03S07.
- Kerry, K. E., Marcialis, R. L., Hamara, D., Fellows, C., (2002), 2001 Mars Odyssey GRS Calibration Report- Version 3.0, University of Arizona, URL: <http://grspds.lpl.arizona.edu/>.
- Ketek GmbH, (2008), URL: <http://www.ketek.net/>.
- Kim, K. J., Drake, D. M., Reedy, R. C., Williams, R. M. S., and Boynton, W. V., (2007), 'Theoretical Fluxes of Gamma-rays from the Martian Surface', *Journal of Geophysical Research*, 111, E03S09, doi:10.1029/2005JE002655, [printed 112(E3), 2007].
- Knoll, G. F., (1999a), 'Linear and Logic Pulse Functions', *Radiation Detection and Measurement* (3rd Edition), Wiley, Chapter 17, pp. 605- 684.
- Knoll, G. F., (1999b), 'Radiation Interactions', *Radiation Detection and Measurement* (3rd Edition), Wiley, Chapter 2, pp. 29- 64.
- Knoll, G. F., (1999c), 'Scintillation Detector Principles', *Radiation Detection and Measurement* (3rd Edition), Wiley, Chapter 8, pp. 219- 264.
- Knoll, G. F., (1999d), 'Photomultiplier Tubes and Photodiodes', *Radiation Detection and Measurement* (3rd Edition), Wiley, Chapter 9, pp. 265- 306.

- Knoll, G. F., (1999e), 'Counting Statistics and Error Propagation', Radiation Detection and Measurement (3rd Edition), Wiley, Chapter 3, pp. 65- 102.
- Knoll, G. F., (1999f), 'General Properties of Radiation Detectors', Radiation Detection and Measurement (3rd Edition), Wiley, Chapter 4, pp. 103- 128.
- Knoll, G. F., (1999g), 'Germanium Gamma-ray Detectors', Radiation Detection and Measurement (3rd Edition), Wiley, Chapter 12, pp. 405- 456.
- Knoll, G. F., (1999h), 'Radiation Spectroscopy with Scintillators', Radiation Detection and Measurement (3rd Edition), Wiley, Chapter 10, pp. 307-352.
- Krane, K. S., (1988), 'Nuclear Reactions', Introductory Nuclear Physics, John Wiley and Sons, Chapter 11, pp. 378-443.
- Kring, D., Schweitzer, J., Meyer, C., Trombka, J., Freund, F., Economou, T., Yen, A., Kim, S. S., Treiman, A., Blake, D., Lisse, C., (1995), 'Precise Chemical Analyses of Planetary Surfaces', Planetary Surface Instruments Workshop, LPI Technical Report 95-05, C. Meyer, A. Treiman, T. Kostiuk (Eds.), Lunar and Planetary Institute, Houston, Chapter 2, pp. 5- 20.
- Kyle, P. R., Moore, J. A., Thirlwall, M. F., (1992), 'Petrologic Evolution of Anorthoclase Phonolite Lavas at Mount Erebus, Ross Island, Antarctica', *Journal of Petrology*, 33, pp. 849- 875.
- Lammer, H., Lichtenegger, H. I. M., Kolb, C., Ribas, I., Guinan, E. F., Abart, R. and Bauer, S. J., (2003), 'Loss of Water from Mars:: Implications for the Oxidation of the Soil', *Icarus*, 165, pp. 9-25.
- Lawrence, D. J., Maurice, S., Feldman, W. C., (2004), 'Gamma-ray Measurements from Lunar Prospector: Time Series Data Reduction for the Gamma-ray Spectrometer', *Journal of Geophysical Research*, 109, E07S05, doi:10.1029/2003JE002206.
- Lawrence, D. J., Feldman, W. C., Barraclough, B. L., Binder, A. B., Elphic, R. C., Maurice, S., Thomsen, D. R., (1998), 'Global Elemental Maps of the Moon: The Lunar Prospector Gamma-ray Spectrometer', *Science*, 281, pp. 1484- 1489.
- Lecoq, P., Annenkov, A., Gektin, A., Korzhik, M., Pedrini, C., (2006), 'Scintillation and Inorganic Scintillators', Inorganic Scintillators for Detector Systems- Physical Principles and Crystal Engineering, Springer Verlag, Chapter 1, pp. 1- 34.
- Lentz, R. C., Taylor, G. J., Treiman, A. H., (1999), 'Formation of Martian Pyroxenite: A Comparative Study of the Nakhilite Meteorites and Theo's Flow', *Meteoritics and Planetary Science*, 34 pp. 919-932.

- Lindstrom, R. M. and Yonezawa, C., (2004), 'Samples and Standards', Handbook of Prompt Gamma Activation Analysis with Neutron Beams, G. L. Molnár (Ed.), Kluwer Academic Publishers, Chapter 3, pp. 59-69.
- Lorenz, K, Calzada, E, Muhlbauer, M, Schillinger, B, Schulz, M, Zeitelhack, K, (2008), 'The New Multi-filter at ANTARES, TOF Measurements and First Applications', *Presented at: The 8th World Conference on Neutron Radiography, NIST, Gaithersburg, MD, USA, 16 - 19th October 2006*, M. Arif and R. D. Downing (Eds.), Neutron Radiography, DEStech Publications Inc., Lancaster, USA.
- Malm, H. L., Canali, C., Mayer, J. W., Nicolet, M.-A., Zanio, K. R., Akutagawa, W., (1975), 'Gamma-ray Spectroscopy with Single-carrier Collection in High-resistivity Semiconductors', *Applied Physics Letters*, 26, pp. 344-346.
- Molnár, G. L., Révay, Zs., Belgya, T., (2002), 'Wide Energy Range Efficiency Calibration Method for Ge Detectors', *Nuclear Instruments and Methods in Physics Research A*, 489, pp. 140-159.
- Martin, R. C., Knauer, J. B., Balo, P. A., (1999), 'Production, Distribution and Applications of Californium-252 Neutron Sources', *Presented at IRRMA '99, 4th Topical meeting on industrial radiation and radioisotope measurement applications, Raleigh, N. Carolina, October 3-7, 1999*.
- Masarik, J. and Reedy, R. C., (1995), 'Terrestrial Cosmogenic Nuclide Production Systematics Calculated from Numerical Simulations', *Earth and Planetary Science Letters*, 136, pp. 381-395.
- Masarik, J. and Reedy, R. C., (1996), 'Gamma-ray Production and Transport in Mars', *Journal of Geophysical Research*, 101, pp. 18,891-18,912.
- McKinney, G. W., Lawrence, D. J., Prettyman, T. H., Elphic, R. C., Feldman, W. C., and Hagerty, J. J., (2006), 'MCNPX Benchmark for Cosmic-ray Interactions with the Moon', *Journal of Geophysical Research*, 111, E06004, doi:10.1029/2005JE002551.
- Mowlavi, A. A. and Koochi-Fayegh, R., (2004), 'Determination of 4.438 MeV γ -ray to Neutron Emission Ratio from a ^{241}Am - ^9Be Neutron Source', *Applied Radiation and Isotopes*, 60, pp. 959-962.
- Morthekai, P., Jain, M., Dartnell, L., Murray, A. S., Bøtter-Jensen, L., Desorgher, L., (2007), 'Modelling of the Dose-rate Variations with Depth in the Martian Regolith using GEANT4', *Nuclear Instruments and Methods in Physics Research A*, 580, pp. 667-670.
- Moszynski, M., Nassalski, A., Syntfeld-Kazuch, A., Szczesniak, T., Czarnacki, W., Wolski, D., Pausch, G., Stein, J., (2006), 'Temperature Dependences of $\text{LaBr}_3(\text{Ce})$, $\text{LaCl}_3(\text{Ce})$ and

- Nal(Tl) Scintillators', *Nuclear Instruments and Methods in Physics Research A*, 568, pp. 739-751.
- Neaman, D. A., (2003a), 'Introduction to the Quantum Theory of Solids', *Semiconductor Physics and Devices: Basic Principles (3rd Edition)*, McGraw Hill, Chapter 3, pp. 56-102.
- Neaman, D. A., (2003b), 'The Semiconductor in Equilibrium', *Semiconductor Physics and Devices: Basic Principles (3rd Edition)*, McGraw Hill, Chapter 4, pp. 103-183.
- Neaman, D. A., (2003c), 'The pn-Junction', *Semiconductor Physics and Devices: Basic Principles (3rd Edition)*, McGraw Hill, Chapter 7, pp. 238-267.
- Neaman, D. A., (2003d), 'Non-equilibrium Excess Carriers in Semiconductors', *Semiconductor Physics and Devices: Basic Principles (3rd Edition)*, McGraw Hill, Chapter 6, pp.189- 238.
- NGDC, (2008), NOAA, Space Physics Interactive Data Resource (SPIDR),
URL: <http://spidr.ngdc.noaa.gov/spidr/>.
- O'Brien, R. C., Ambrosi, R. M., Bannister, N. P. et al., (2009), 'Neutron Sources for Radioisotope Power Systems and In-situ Planetary Science Applications', *In preparation for submission to Journal of Nuclear Materials*.
- O'Brien, R. C., Ambrosi, R. M., Bannister, N. P., Howe, S. D., Atkinson, H. V., (2008), 'Safe Radioisotope Thermoelectric Generators and Heat Sources for Space Applications', *Journal Nuclear Materials*, 377, pp. 506- 521.
- Oda, O., (2007), 'CdTe', *Compound Semiconductor Bulk Materials and Characterisation*, World Scientific, Chapter 15, pp. 377-425.
- Okada, T., Shirai, K., Yamamoto, Y., Arai, T., Ogawa, K., Hosono, K., Kato, M., (2006), 'X-ray Fluorescence Spectrometry of Asteroid Itokawa by Hayabusa', *Science*, 312, pp. 1338-1343.
- Okada, E., Miura, I., Wakatsuki T., Hirao, Y., (1958), 'Gamma Rays from the Proton Bombardment of Silicon', *Journal of the Physical Society of Japan*, 13, pp. 541- 544.
- ORTEC[®], (2007), Pulse Formation Process, Review of the Physics of Semiconductor Detectors,
URL: http://www.ortec-online.com/detectors/review_physics/pulse.htm.
- Owens, A., Brandenburg, S., Buis, E. J., Kiewiet, H., Kraft, S., Ostendorf, R. W., Peacock, A., Quarati, F., Quirin, P., (2007a), 'An Assessment of Radiation Damage in Space-based Germanium Detectors due to Solar Proton Events', *Nuclear Instruments and Methods in Physics Research A*, 583, pp. 285- 301.
- Owens, A., Bos, A. J. J., Brandenburg, S., Buis, E. J., Dathy, C., Dorenbos, P., van Eijk, C. W. E., Kraft, S., Ostendorf, R. W., Ouspenski, V., Quarati, F., (2007b), 'Assessment of the

- Radiation Tolerance of LaBr₃:Ce Scintillators to Solar Proton Events', *Nuclear Instruments and Methods in Physics Research A*, 572, pp. 785- 793.
- Pelowitz, D. B. (Ed.), (2005), MCNPX User's Manual Version 2.6.0, Report LA-CP-07-1473, Los Alamos National Laboratory, Los Alamos, N. M.
- Photonis, (2007), Photomultiplier XP2060 Data Sheet,
URL:http://www.photonis.com/medical/products/photomultipliers_assemblies/product_specifications.
- Potts, P. J., (1987), 'X-ray Fluorescence Analysis: Principles and Practices of Wavelength Dispersive Spectrometry', *A Handbook of Silicate Rock Analysis*, Blackie & Son Ltd., Chapter 8, pp. 226- 285.
- Prettyman, T. H., Hagerty, J. J., Elphic, R. C., Feldman, W. C., Lawrence, D. J., McKinney, G. W., Vaniman, D. T., (2006), 'Elemental Composition of the Lunar Surface: Analysis of Gamma-ray Spectroscopy Data from Lunar Prospector', *Journal of Geophysical Research*, 111, E12007.
- Quaranta, A. A., et al., (1968), 'Transport Phenomena', *Semiconductor Detectors*, G. Bertolini and A. Coche (Eds.), North-Holland Publishing Company, Section 1.3, pp. 53- 102.
- Quarati, F., Bos, A. J. J., Brandenburg, S., Dathy, C., Dorenbos, P., Kraft, S., Ostendorf, R. W., Ouspenski, V., Owens, A., (2007), 'X-ray and Gamma-ray Response of a 2"×2" LaBr₃:Ce Scintillation Detector', *Nuclear Instruments and Methods in Physics Research A*, 574, pp. 115-120.
- Reames, D. V., (1999a), 'Particle Acceleration at the Sun and in the Heliosphere', *Space Science Reviews*, 90, pp. 413-491.
- Reames, D., (1999b), 'Solar Energetic Particles: Is there time to hide?', *Radiation Measurement*, 30, pp. 297-308.
- Redus, B., (2003), Application Note ANCZT-2 Rev. 2 Charge Trapping in XR-100T-CdTe and -CZT Detectors, URL: <http://www.amptek.com/anczt2.html>.
- Reedy R. C. and Arnold, J. R., (1972), 'Interaction of Solar and Galactic Cosmic-Ray Particles with the Moon', *Journal of Geophysical Research*, 77, pp. 537-555.
- Restelli, G., (1968), 'Semiconductor Properties of Silicon and Germanium', *Semiconductor Detectors*, G. Bertolini and A. Coche (Eds.), North-Holland Publishing Company, Section 1.1, pp. 11- 26.
- Révay, Zs. and Belga, T., (2004), 'Principles of the PGAA method', *Handbook of Prompt Gamma Activation Analysis*, G. L. Molnár (Ed.), Kluwer Academic Publishers, Chapter 1, pp. 1-30.

- Révay, Zs., Firestone, R. B., Belgya, T., Molnár, G. L., (2004), 'Prompt Gamma-Ray Spectrum Catalog', Handbook of Prompt Gamma Activation Analysis, G. L. Molnár (Ed.), Kluwer Academic Publishers, Chapter 7, pp. 173-364.
- Richter, M. and Siffert, P., (1992), 'High Resolution Gamma-ray Spectroscopy with CdTe Detector Systems', *Nuclear Instruments and Methods in Physics Research A*, 322, pp. 529-537.
- Rieder, R., Wänke, H., Economou, T., Turkevich, A., (1997), 'Determination of the Chemical Composition of Martian Soil and Rocks: The Alpha Proton X ray Spectrometer', *Journal of Geophysical Research*, 102, pp. 4027-4044.
- Saint-Gobain Crystals, (2007), Efficiency Calculations for Selected Scintillators,
URL: <http://www.detectors.saint-gobain.com>.
- Sano, T., Hasenaka, T., Sawahata, H., Fukuoka, T., (2005), 'Determination of Ti, K, Sm and Gd Values in Geological Survey of Japan Reference Materials by Prompt Gamma Neutron Activation Analysis', *Geostandards and Geoanalytical Research*, 30, pp. 31-37.
- Sellin, P. J., Davies, A. W., Lohnstroh, A., Ozsán, M. E., Parkin, J., Siffert, P., Sowinska, M., Simon, A., (2004), Charge Transport and Mobility Mapping in CdTe,
URL: http://personal.ph.surrey.ac.uk/~phs2ps/rome_cdte_oct04.pdf.
- Shah, K. S. et al., (2002a), 'LaBr₃:Ce Scintillators for Gamma-ray Spectroscopy', *IEEE Transactions on Nuclear Science*, 50, pp. 2410- 2413.
- Shah, K. S. et al., (2002b), 'LuI₃:Ce—A New Scintillator for Gamma-ray Spectroscopy', *IEEE Transactions on Nuclear Science*, 51, pp. 2302- 2305.
- Siffert, P. and Coche, A., (1968a), 'Behaviour of Lithium in Silicon and Germanium', Semiconductor Detectors, G. Bertolini and A. Coche (Eds.), North-Holland Publishing Company, Section 1.2, pp. 27- 52.
- Simon, H., (2009), Personal Communication.
- Simonsen, L. C., and Nealy, J. E., (1991), 'Radiation Protection for Human Missions to the Moon and Mars', NASA Technical Paper 3079.
- Space Systems Loral, (1996), GOES I-M Databook, Goddard Space Flight Centre, DRL 101-08 (Revision 1), 31/08/1996.
- Spohn, T., Seiferlin, K., Hagermann, A., Knollenberg, J., Ball, A. J., Banaszkiwicz, M., Benkhoff, J., Gadomski, S., Gregorczyk, W., Grygorczuk, J., Hlond, M., Kargl, G., Kührt, E., Kömle, N., Krasowski, J., Marczewski, W., Zarnecki, J. C. (2007), 'Mupus: A Thermal and Mechanical Properties Probe for the Rosetta Lander Philae', *Space Science Reviews*, 128, pp. 339-362.

- Spohn, T., Ball A. J., Seiferlin K., Conzelmann V., Hagermann A., Kömle N. I. and Kargl G., (2001), 'A Heat Flow and Physical Properties Package for the Surface of Mercury', *Planetary and Space Science*, 49, pp. 1571-1577.
- Starr, R. D., Ho, G. C., Schlemm, C., Gold, R. E., Goldsten, J. O., Boynton, W. V., Trombka, J. I., (2001), 'The X-ray Spectrometer for Mercury: MESSENGER (8055), Workshop on Mercury: Space Environment, Surface, and Interior', *Proceedings of a workshop held at The Field Museum, 4-5 October, 2001, Chicago, IL. Convened by M. Robinson and G. J. Taylor. LPI Contribution No. 1097. Houston, TX: Lunar and Planetary Science Institute*, p.102.
- Stynfeld, A., Arlt, R., Gostilo, V., Loupilov, A., Moszynski, M., Nassalski, A., Swoboda, M., Wolski, D., (2006), 'Comparison of a LaBr₃(Ce) Scintillation Detector with a Large Volume CdZnTe Detector' *IEEE Transactions on Nuclear Science*, 53, pp. 3938-3943.
- Sueki, K., Kobayashi, K., Sato, W., Nakahara, H., Tomizawa, T., (1996), 'Nondestructive Determination of Major Elements in a Large Sample by Prompt γ Ray Neutron Activation Analysis', *Analytical Chemistry*, 68, pp. 2203- 2209.
- Surkov, Y., (1997a), 'Gamma-ray Spectrometric Studies', *Exploration of Terrestrial Planets from Spacecraft- Instrumentation, Investigation and Interpretation (2nd Edition)*, John Wiley and Sons, Section 2.1, pp. 140-244.
- Surkov, Y., (1997b), 'X-ray Spectrometric Studies', *Exploration of Terrestrial Planets from Spacecraft- Instrumentation, Investigation and Interpretation (2nd Edition)*, John Wiley and Sons, Section 2.2, pp. 245-311.
- Swindle, T. D., Masarik, J., Kollár, D., Kim, K. J., Reedy, R. C., (2005), 'Production of Noble Gases Near the Surface of Europa and the Prospects for In-situ Chronology', *Icarus*, 174, pp. 205-214.
- Swindle, T. D., (2001), 'Could In-situ Dating Work on Mars?', *Lunar and Planetary Science*, XXXII, 1492.
- Talboys, D. L., Barber, S., Bridges, J. C., Kelley, S. P., Pullan, D., Verchovsky, A. B., Butcher, G., Fazel, A., Fraser, G. W., Pillinger, C. T., Sims, M. R., Wright, I. P., (2009), 'In-situ Radiometric Dating on Mars: Investigation of the Feasibility of K-Ar Dating using Flight-type Mass and X-ray Spectrometers', *Planetary and Space Science*, 57, pp.1237-1245.
- Talboys, D. L., (2006), 'The Beagle 2 X-ray Spectrometer for Mars', Thesis (Ph.D.), University of Leicester.

- Technische Universität München (TUM), (2001), Experimental Facilities at FRM-II, Research with Neutrons, Public Relations, Garching, Germany, URL: <http://www.FRM-2.tu-muenchen.de>.
- Topinka, L., Columbia Plateau, Columbia River Basalt Group, USGS/Cascades Volcano Observatory, Vancouver, Washington, 23/01/2007,
URL: <http://vulcan.wr.usgs.gov/Volcanoes/ColumbiaPlateau/framework.html>.
- Vega-Carrillo, H. R., Manzanares-Acuña, E., Becerra-Ferreiro, A. M., Carrillo-Nuñez, A., (2002), 'Neutron and Gamma-ray Spectra of $^{239}\text{PuBe}$ and $^{241}\text{AmBe}$ ', *Applied Radiation and Isotopes*, 57, pp. 167-170.
- Warren, P. H. and Rasmussen, K. L., (1987), 'Megaregolith Insulation, Internal Temperatures, and Bulk Uranium Content of the Moon', *Journal of Geophysical Research*, 92, pp. 3453-3465.
- Watanabe, S. et al., (2002), 'CdTe Stacked Detectors for Gamma-ray Detection', *IEEE Transactions on Nuclear Science*, 49, pp. 1292- 1296.
- Wolf, R. A., (1995), 'Magnetospheric Configuration', Introduction to Space Physics, M. G. Kivelson, and C. T. Russell (Eds.), Cambridge University Press, Chapter 10, pp. 227-287.
- Yin, L., I., Trombka, J., I., Adler, I., Bielefeld, M., (1993), 'X-ray Remote Sensing Techniques for Geochemical Analysis of Planetary Surfaces', Remote Geochemical Analysis: Elemental and Mineralogical Composition, C. M. Pieters and P. A. J. Englert (Eds.), Cambridge University Press, Chapter 9, pp. 199-212.
- Zolotov, M. Y. and Shock, E. L., (2000), 'Composition and Stability of Salts on the Surface of Europa and their Oceanic Origin', *Journal of Geophysical Research*, 106, pp. 32815-32827.